Bakk.rer.nat. Mag.rer.nat. Johanna Kraxner

Analytical TEM of organic electronics with a special focus on EDXS and geometry aspects

DOCTORAL THESIS

to achieve the university degree of

Doktorin der Naturwissenschaften

Submitted to

Graz University of Technology

Supervisor

Ao. Univ.-Prof. Dipl.-Ing. Dr.techn. Werner Grogger

Institute for Electron Microscopy and Nanoanalysis (FELMI)

Graz Centre for Electron Microscopy (ZFE)

Graz, February 2018

Abstract

This thesis is devoted to the improvement of light element analysis in the transmission electron microscope. Light elements are the main components of organic electronic devices. The analysis of light elements mainly focuses on the analysis using energy-dispersive X-ray spectrometry (EDXS). Quantitative EDXS is done using the ζ-factor technique on a four quadrant detector system (a Super-X system by FEI). The complex geometry of such an EDXS system makes reliable quantitative EDXS challenging.

This thesis is organized in three main chapters: The analysis of organic electronic devices; quantitative EDXS and the influence of geometry on EDXS results.

The first chapter is on the characterization of organic electronic devices. The characterization is done with electron microscopy, including methods like electron energy loss spectroscopy (EELS) and EDXS. This work was done in an FFG project (NILEcho II, 830269). The goal of the project was to develop an organic thin film transistor (oTFT) made out of printable materials. The ongoing transition to an all-organic transistor makes the analysis using transmission electron microscopy more challenging because the materials get more and more similar in their composition. This makes imaging of structures of different materials difficult because of the similarity in contrast. The materials used in oTFTs and in the manufacturing process are mainly consisting of elements like hydrogen, carbon, oxygen and sometimes nitrogen and sulphur. Depending on the materials we either used EDXS or EELS to differentiate between the structures. Electron energy loss spectroscopy was done by focusing on the plasmon region as well as on the fine structure of the carbon K edge. We further focused on light element analysis in the TEM.

Therefore, the second chapter is on the ζ-factor technique which is a quantitative EDXS method. An iterative process gains the concentration values and the mass thickness. The mass-thickness can be used to do an iterative absorption correction, which is mandatory for quantitative EDXS of light elements. We briefly explain the background of the method and compare it to the Cliff-Lorimer ratio technique. Important aspects for the ζ-factor determination are discussed: Starting with finding the right standard materials; measuring the absolute thickness of the samples (which is needed to measure a ζ-factor). We further discuss the influence of the mean free path length of the material and the influence of the chosen method to evaluate an EDX spectrum as far as the background correction and intensity determination is considered.

The last chapter is on the precise characterization of the geometry of the used EDXS system. This work was done on a Super-X system which has four EDX detector quadrants

spaced symmetrically around the electron beam. The understanding of the complex geometry is of huge importance for a precise understanding of the measured EDX signal. Therefore, a detailed model of the used specimen holder was made using computed X-ray tomography. With a combination of tilt experiments and simulations a precise analysis of the Super-X system could be performed. This gave a deeper understanding of the importance of geometry on the measured EDX signal. Not only the position of the EDX detectors has a severe influence, but also the used TEM specimen holder is an important parameter. We could identify the exact location of all four detector quadrants their distance and elevation angle. Finally estimations have been made about the influence of the energy dependent absorption of X-ray photons in the beryllium portion of the specimen holder.

Kurzfassung

Die vorliegende Arbeit ist thematisch in drei große Kapitel gegliedert: die Untersuchung von organisch-elektronischen Bauteilen mittels Elektronenmikroskope, quantitative, energiedispersive Röntgenspektroskopie (EDXS) unter Verwendung der ζ-Faktor Methode und der genaueren Betrachtung von geometrischen Einflüssen des Systems Detektor-Probenhalter auf die detektierte Röntgenstrahlung. Der rote Faden der sich durch alle drei Kapitel zieht, ist die Analyse von leichten Elemente.

Organische Elektronik basiert hauptsächlich auf Polymeren. Polymere wiederum bestehen zu einem großen Teil aus Kohlenstoff und Wasserstoff und zu geringeren Teilen aus Stickstoff, Schwefel, Phosphor, Silizium und Spuren anderer Elemente. Sie sind oft in der Zusammensetzung und der chemischen Struktur sehr ähnlich, was die Analyse mittels Elektronenmikrokopie sehr herausfordernd gestaltet. Die Arbeit zum Thema organische Elektronik wurde mit Unterstützung des FFG Projekt NILEcho II (830269) durchgeführt. Das Ziel dieses Projektes war einen organischen Transistor aus druckbaren Materialien herzustellen. In dieser Arbeit werden Ergebnisse präsentiert, wie Elektronenmikroskopie unterstützen kann, bei der Weiterentwicklung und Charakterisierung von Produktionsprozessen sowie der Charakterisierung fertiger Bauteile.

Das zweite Kapitel beschäftigt sich mit der sogenannten ζ-Faktor Methode. Dies ist eine Methode zur quantitativen EDXS, die die Möglichkeit bietet iterative die Absorption von Röntgenstrahlung in der Probe zu berücksichtigen. Diese Absorptionskorrektur ist Voraussetzung für die Verwendung von quantitativer EDXS an Proben welche auch leichte Elemente enthalten. Es werden ζ-Faktoren für Al, Si und O präsentiert. Das eigentliche Ergebnis dieses Kapitels liegt jedoch in der genauen Betrachtung aller Faktoren, welche die Bestimmung von ζ-Faktoren beeinflussen, beginnend bei der Wahl des Standards bis hin zur Wahl des Programmes mit welchem die Daten ausgewertet werden.

Das letzte Kapitel beschäftigt sich mit einer eingehenden Betrachtung des Super-X Systems. Das Super-X System ist ein Detektor System, welches aus vier symmetrisch angebrachte Detektor Quadranten besteht. Die Geometrie dieses Detektorsystems wird mittels einer Kombination aus Simulation und Experiment nachgebildet. Das so erhaltene Modell ermöglicht uns die geometrischen Einflüsse, wie Schattenbildung des Probenhalters auf den einzelnen Detektoren, zu berücksichtigen. Diese Einflüsse sind gravierend und können daher nicht vernachlässigt werden, wenn eine korrekte Quantifizierung mittel EDXS durchgeführt werden soll.

Acknowledgement

Many people have to be acknowledged. I would like to start with my family and my friends who supported me through all my studies.

I want to thank Werner Grogger for his supervision and also all other FELMI ZFE members as well as Ferdinand Hofer the head of the institute. We were a large community of Phd students which helped a lot for motivation and also scientific input. I also want to thank especially Stefan Mitsche with whom I shared an office. He made my time at the FELMI much more fun. I also would like to thank Stefanie Fladischer who did her best at the beginning of my thesis that I had a good start. I also want to thank Judith Lammer, who I was allowed to co-supervise during her master thesis and who will continue the work I did, for the discussions we had.

From my friends I would like to thank especially Andrea, Claudia and Jakob who shared the time of the Phd thesis with me.

And last but not least I would like to thank Daniel Knez for all the endless discussions and motivation he provided, without whom I am not sure the thesis would have come to an end.

Preamble

Many people have contributed to this work.

Content

1   Introduction

The thesis is built up of three main chapters dealing with organic electronics, quantitative energy-dispersive X-ray spectrometry (EDXS) and the influence of the geometry on a four detector quadrant EDXS system on the gained X-ray intensity. All chapters have in common the analysis of light elements using analytical TEM. The structure and the content of the thesis developed over the years of research. At the beginning, the analysis of organic electronic devices was the main goal. This was to assist the development of an organic thin film transistor made out of all printable materials. This work was done in the NILEcho II project (FFG 830269). Electron microscopy is a very valuable tool for the process development and for device characterisation. The field of organic electronics is still a very young field of research compared to conventional electronics but with rapid growing interest of the industry (*1*). The search for new manufacturing procedures (*2, 3*) and materials is still ongoing. Therefore, a precise monitoring of each process step is of huge importance. Electron microscopy can assist in several stages of the manufacturing process and final characterization of the devices. Surface analysis as well as cross-section investigations can be done using SEM (scanning electron microscopy) and TEM. These analysis can help to introduce new materials in ongoing processes and can also help to understand device performance (*4, 5*). The analysis using electron microscopy gets more challenging as the amount of organic material in the device increases. To investigate an all polymer layer stack analytical electron microscopy is needed. Therefore, EDXS and EELS are essential. Especially, the electron energy loss in the plasmon region and the C-edge fine structure can provide significant differences between materials (*6*) rather similar in composition. Although, EELS is the method of choice for characterizing light elements, EDXS is also a very powerful method for this purpose. Especially, if a windowless, large area detector is available, like a Super-X detector. As far as quantitative EDXS of light elements is concerned, the ζ-factors method has to be considered with its possibility to perform an iterative absorption correction. Therefore, we also focused on quantitative EDXS. The work presented here builds up on the work by Stefanie Fladischer (*7*), who started to establish the ζ-factor method at our institute. The ζ-factor technique is a method for EDXS quantification. When we started to work on the ζ-factor method the goal was to measure the ζ-factors for the "light elements". This was for two reasons: firstly the ζ-factors at our institute are so far determined using a NIST standard (SRM2063a (*8*)), following a method of (*9*). This standard material contains O, Si, Mg, Fe and Ca and can be used to inter/extrapolate all ζ-factors of K lines by a fitting process. This fitting process contains a parameter optimization, considering for e.g. the thickness of the detector-window material, the contact layer and, the ionization

cross-section. The dependency of the gained ζ-factors on the chosen ionization cross-section model is rather high. The choice of the ionization cross-section model has the highest influence for light elements (atomic number Z<~10) and heavy elements (Z>30).

The second reason was to use the ζ-factors on the analysis of organic electronic devices, which mainly contain light elements. During the process of the ζ-factor measurements several questions arose, considering the reproducibility of the gained result. Influences on the gained results are studied on aspects like: the choice of the standard sample, the measurement procedure, the person measuring the sample and the intensity evaluation. We present the ζ-factors of Si, Al and O, but the main result of the chapter on ζ-factors is a very close consideration on all aspects, which can influence the gained ζ-factors. These close considerations lead us to the topic of the last chapter: a geometrical study of the Super-X system is presented. The geometry plays an important role considering quantification using the ζ-factor technique. Exact knowledge of the geometry is needed to perform an absorption correction, which is mandatory to gain reliable results on light element analysis. Therefore, we identify in the third chapter the exact detector positions. We used a combination of an experimentally measured tilt series with simulations using a very precise model of the Super-X system. We not only determined the exact positions of the detectors, we also found that the shadow cast by the holder on the detectors plays a significant role in a four quadrant detector system. Finally, we were able to simulate the exact influence this shadow has on the gained X-ray signal.

2   Light elements - OE

2.1   Organic electronics

Organic electronics is a field of research gaining more and more interest from industry. Organic electronics is mainly carbon based electronics in comparison to inorganic electronics which is mainly silicon based. The main advantage usually associated with organic electronics is the reduced production costs. This is due to the usage of different materials, which allow the introduction of more cost-efficient methods in manufacturing. These new materials also open up new fields of application and thereby new markets. The materials can be applied easily on large areas, are flexible, lightweight, can be modified to show different functionalities (e.g. interesting for sensing) and can even be biocompatible. In principle, organic materials can be tuned to have all kinds of properties. Nonetheless, organic electronics will probably never meet the performance of an inorganic device due to the lower charge carrier mobilites in organic semiconductors. Still, organic electronics has already entered the marked of displays, where the switching speed and integration density are not the crucial factors but large area production and low cost manufacturing.

One big advantage seen in organic electronics is that most materials can be processed out of solution. The possibility to produce functional structures out of solution makes it possible to combine the manufacturing of electronics with printing techniques. Printing techniques can be used to structure large areas and are therefore inexpensive. Moreover, the usage of a flexible substrate would even make a role-to-role production possible (*10–12*).

So, the combination of printing techniques and organic materials allow a cost-efficient production of electrical devices with novel properties like e.g. flexibility and transparency.

2.1.1   The organic thin film transistor

The transistor is a key element of every electronic logic circuit. Metal-insulator-semiconductor (MIS) field-effect transistors (FET) are one of the most important groups of transistors in mainstream semiconductor technology in microprocessors, solid-state memories, mobile communication chips and so on. The MISFET is defined by a semiconductive and a conductive gate electrode separated by a thin insulating layer. If a voltage is applied at the gate electrode a thin sheet of mobile electronic charges is created at the semiconductor-insulator interface.

The charge carrier density can be controlled with the applied gate voltage and thereby the current flow between the two additional contacts (source and drain) can be adjusted.

The thin film transistor is a very prominent device in organic electronics because of its low requirements on the purity of materials (*13*). Due to the low requirements it can be considered as the most relevant device in organic electronics development (*14*). A thin film transistor becomes an organic thin film transistor (oTFT) if at least the semiconductive layer is made of organic material. Several different setups of oTFTs exist. In Figure 1 b) the bottom contact configuration is shown. Each oTFT has, similar to inorganic MISFETs, three electrodes: a gate, a source and a drain electrode. Whereas, the different oTFTs designs have different advantages and disadvantages the gate electrode is always separated by the dielectric layer from the source and drain electrodes (*15*). The source and drain electrodes are at the same level and always connected to the semiconductive layer. In this oTFT design, a voltage is applied to the gate electrode controlling the current flow between source and drain.
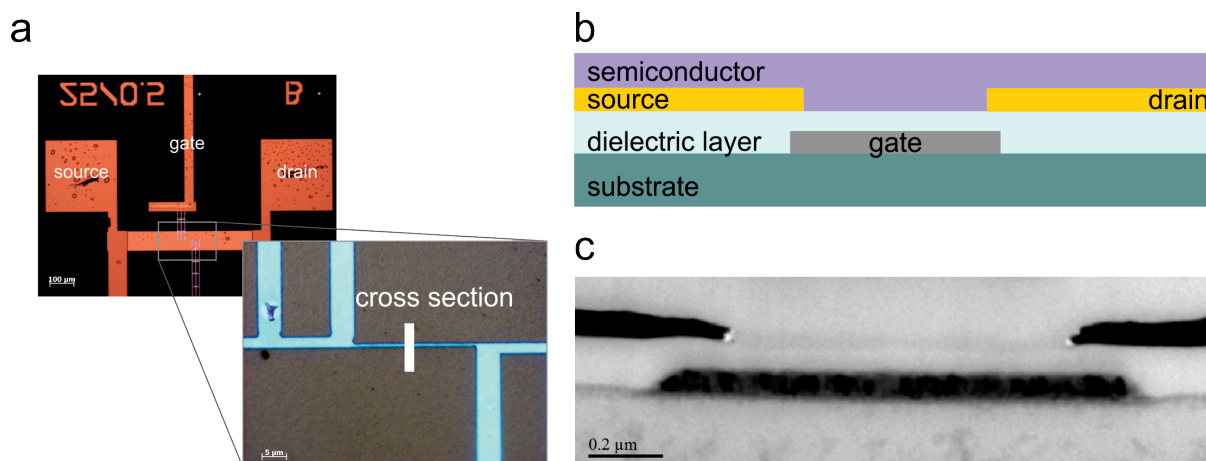
Figure 1: a) Light microscope of an oTFT. The white bar in the magnified image indicates the position of which a TEM lamella was prepared. b) Schematic of an oTFT. c) TEM image of a cross-section of an oTFT.

Figure 1a shows a light micrograph of an oTFT. One can see the source, drain and gate electrodes. In the magnified image, the channel region can be seen and the position of which a TEM lamella was prepared is marked with a white bar. In Figure 1b a schematic of an oTFT can be seen and in Figure 1c a TEM image of an oTFT.

In this work, only the configuration shown in Figure 1b was studied. As substrate materials PET (Polyethylene terephthalate), PC (Polycarbonate) and Kapton (Polyimid) were used. The substrate material needs to be bendable with regard to a roll-to-roll processing. It needs to

withstand all further fabrication steps (e.g. temperature and solvents) without being damaged and it needs to be suitable for the fabrication process used with regard to UV transparency and thermal expansion. As gate dielectric material aluminum, copper and silver were used (applied by thermal evaporation). Dielectric materials used here were: PVCi (poly(vinyl cinnamate) derivative), BCB (divinyl-tetramethylsiloxane-bis(benzocyclobutene) derivative)) and PMMA (Poly(methyl methacrylate)). The source and drain material was either gold or PEDOT:PSS (Poly(3,4-ethylenedioxythiophene) Polystyrene sulfonate). As semiconductive material the p-type semiconductor pentacene was used.

The manufacturing process of the oTFTs shown here either followed (*16*) or (*2*) and is described in more detail in (*17*).

Cross-section analyses of oTFTs provide valuable insights for the improvements of manufacturing processes as well as for the understanding of the electrical characteristics. TEM cross-section analysis can be performed during manufacturing steps to assure e.g. the suitability of a new material for a process step. This can answer questions about remaining residuals (e.g. in (*2*)), structuring of electrodes, layer thicknesses and so on. Moreover, parameters for understanding the electrical characteristics like the dielectric layer thickness or the gate and source/drain overlap (*18*) can be gained. The miniaturization of the structures is a substantial requirement, achieving faster devices with a lower driving voltage and higher integration density. A transition to an all-organic device is favoured with regard to the printability of the devices (*19*). This on-going transition continuously challenges the TEM characterization due to the lack of distinguishable features between the materials.

The following chapters give an overview of how microscopy is used to improve the manufacturing of organic electronic devices and to answer questions arising during the characterization with a special focus on the questions arising in the FFG project (NILEcho II (830269)). Information can be gained either by using an SEM if for instance the surface of an imprint should be evaluated. If the structures are large enough a cross section analysis can also be performed using a FIB (focused ion beam) instrument; in the presented case the gate source/drain overlap were determined. If the structures get smaller a TEM analysis had to be performed. Often imaging techniques could answer questions concerning the structure of oTFT components, thicknesses of layers as well as overlaps of electrodes. For a more advanced analysis or materials which cannot be distinguished by only using imaging techniques analytical TEM was used; either EDXS or EELS. Analytical TEM was also mainly used to make the different features in an oTFT visible to be able to evaluate their structure. The structure is influenced by the initial patterning but also each manufacturing step can have a severe

influence (e.g. used solvents or temperature inputs). Questions answered using TEM presented here, were about the structure and thicknesses of oTFT features. Moreover, the aim was to make each organic material used during the manufacturing visible or distinguishable in the TEM.

2.2   SEM

In the following section an overview of examples is given were the resolution of a scanning electron microscope is sufficient to answer appearing questions during the manufacturing of organic electronic devices.

The basis of each NIL process is the stamp itself. The quality of the stamp is directly transferred to the imprinted resist. This is true for hot embossing as well as UV or thermally triggered structure transfer. The stamps used in all the processes considered here are made of silicon. The stamps are structured by e-beam lithography and the structure transfer is done by a wet etching step. Due to the inorganic nature of the stamps, their stability is usually not the limiting factor as long as their surface energy corresponds to the imprint resist.

The next component to be considered for a satisfying structure transfer is the imprint resist. This is always some kind of organic material; either a thermoplastic if hot embossing is used to structure the gate electrodes or a cross-linkable polymer if e.g. an UV-NIL process is performed. During the manufacturing flow of some self-aligned oTFTs the problem occurred that the metal gate electrode (in this case Cu) was ripped off during the stripping process. Taking a closer look on the imprinted structure answered the question why that behaviour appeared. In Figure 2 on the left side (a, c) the original imprint is shown (As imprint resist mr I7030E by microresist technologies is used). On the right side (Figure 2b, d) the resist after the reactive ion etching step is shown. It can clearly be seen that an unfavourable etching behaviour occurred. The resist was not removed homogenously. The solution for this problem was to use a new imprinting resist. Sometimes organic materials used in organic electronics tend to change properties after a certain time. This might be either due to introduced impurities, unstable components or changes in concentration due to depletion of more volatile components.
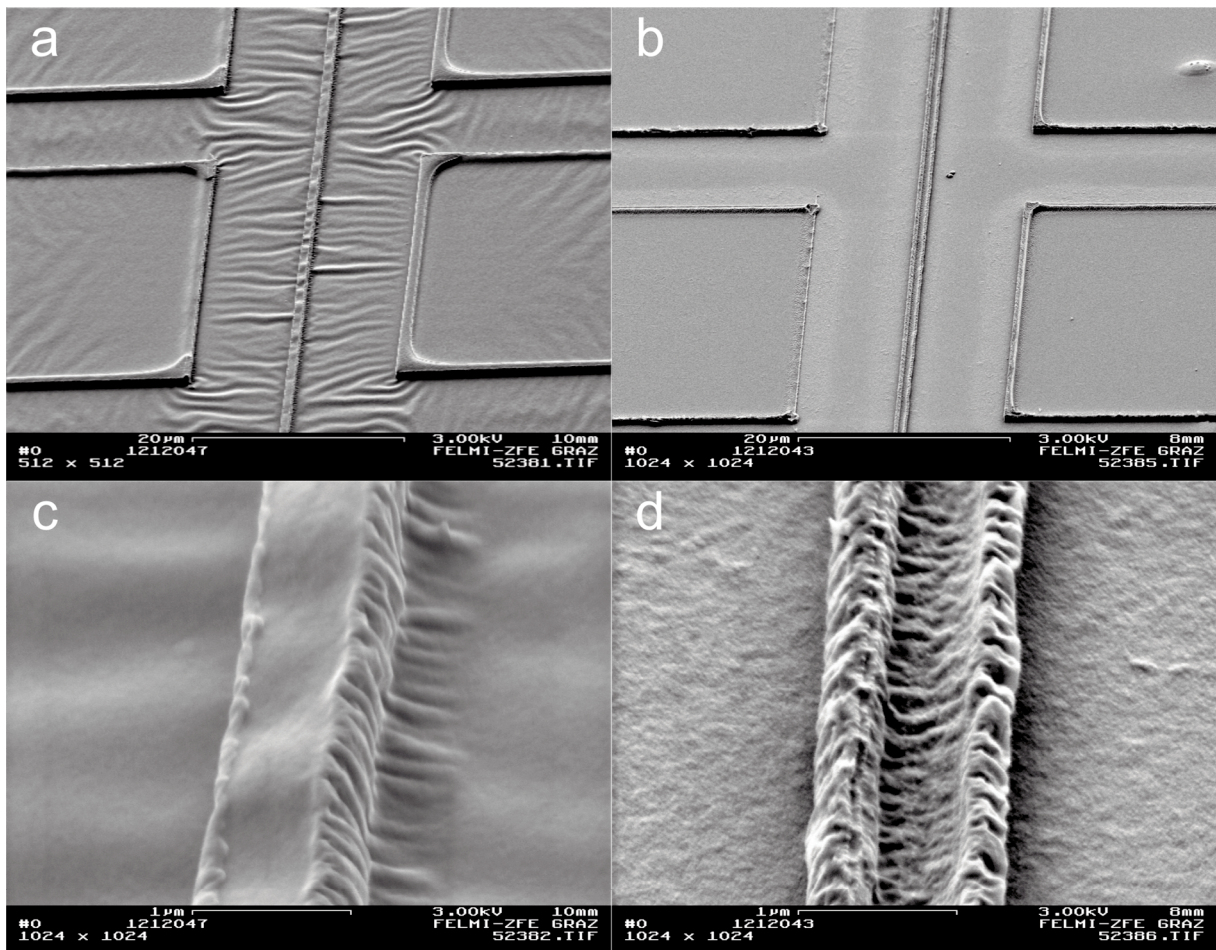
Figure 2: a) c) SE images of a hot embossing imprint. b) d) Imprint after reactive ion etch.

We also studied the influence of the source-gate and drain-gate overlap on the transistor performance (*17*). Therefore, an existing self-aligned process was modified to realize a varying overlap. The modification was done by changing the illumination angle of the photoresist (a wedge with different angles was used: 0°,55°, 65° 75° and 85°) and thereby realizing devices with an overlap between +1.5 µm to -0.2 µm. One transistor of each incident angle was investigated using a FEI NOVA 200 dual beam system. The channel length and overlaps of source-gate and drain-gate were determined. To avoid sample damage and prevent charging a Pt/Pd layer of around 80 nm was deposited (Leica EM ACE600) followed by an ion beam induced Pt/C layer (~1 µm). Trench milling were performed with a constant acceleration voltage of 30 kV and a beam current of 500 pA. While for final polishing currents of 100 pA and 50 pA with a dwell time of 500 µs were used. To avoid damage to the organic layers a recently introduced patterning strategy was used (*20–22*). Cross section analysis was in-situ performed using a through-the-lens-detector in secondary electron mode. The possibility do

answer these questions using the FIB enabled the fast analysis of several regions of a transistor and so lead to an improved statistic. In Figure 3 an example of a cross-section of a transistor illuminated with an angle of 75° is shown. The angle results in a channel length of 3.67 ±0.04 µm, a left overlap of 1.70 ±0.20 µm and a right overall of -0.17 ±0.03 µm. The effect of the variation in the channel region on the electrical behaviour of the device could be summed up as follows: if a gap appears between the source and gate electrode the on-current drops significantly; an overlap >180 nm is needed for an overlap-independent on-current; the influence of the drain to gate overlap on the on-current seems to be negligible. For more detail on the experiment as well as on the results see (*5, 17*).
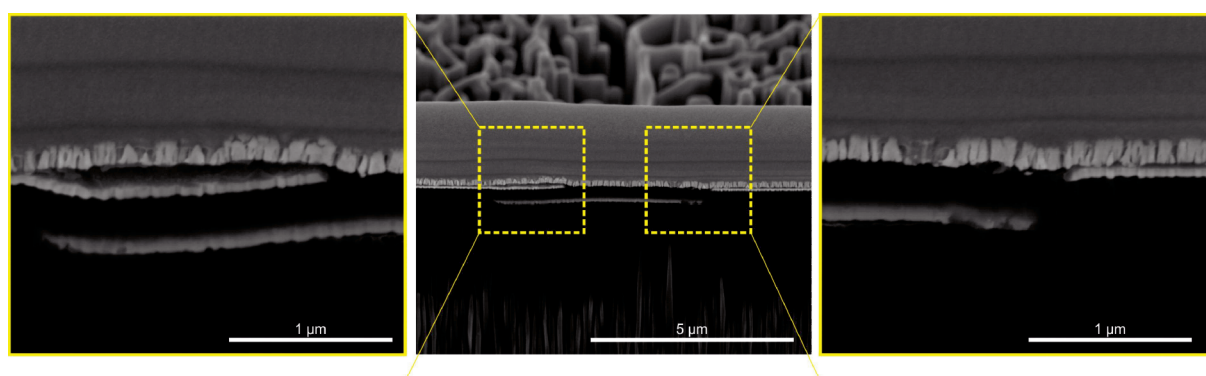
Figure 3: Secondary electron images acquired at 5 kV using a through-the-lens detector (TLD). Channel region of an oTFT (middle) tilted by 75° during illumination and in more detail (left and right) the overlap regions of each side.

The big advantage of doing an analysis in the SEM is that the sample preparation is less labour-intensive and time consuming compared to TEM. It is suitable especially for the cross section analysis as presented here because different sample regions can be analysed without a lot of additional sample preparation steps.

2.3 Organic material analysis in the TEM

Generally, for the analysis of organic materials, in our case oligo- and polymers, the same methods are used which are used for inorganic materials. This includes TEM imaging methods such as bright- and dark field, diffraction and high resolution but also the imaging generation using different signals in STEM (scanning transmission electron microscopy) mode such as HAADF (high angular annual dark field) and BF (bright field). Moreover, the analytic capabilities of an analytical electron microscope (as EDXS and EELS or EFTEM (energy filtered TEM) can also provide important information. The main difference to the analysis of

organic materials compared to inorganic materials is that these materials mainly consist of light elements such as: C, O, N, S and H. On the one hand the elastic interaction of light elements with energetic electrons is rather weak leading to low contrasts in TEM. On the other hand, the inelastic interactions are relatively strong providing the ability to do spectroscopy but also may lead to radiation damage.

If the polymer system is suitable it can be analysed solely using by imaging techniques. Differences in the morphology generate differences in contrast; contrast is generated by spatial variations of crystallinity, thickness, crystal orientation or density due to the presence of heavier elements. These mechanisms, Bragg diffraction and Rutherford scattering, lead to electrons scattered to relatively high angles where they either can be blocked by the objective aperture or detected using a HAADF in STEM.

Bragg diffraction only appears if crystalline or semi crystalline organic systems are studied. Such systems also allow high resolution imaging in TEM (*23–27*) and STEM (*25*) provided that the material withstands the electron beam without damage. Moreover, diffraction analysis can be performed and dark field imaging is also used (*28–30*).

Often heavy element staining is used to increase Rutherford scattering. Stains are materials which bind or should bind preferentially to certain material properties such as e.g. double bonds or amorphous parts of polymer blends. Common stains are for example uranyl acetate, osmium or ruthenium tetroxide. The high Z-elements enhance high-angle Rutherford scattering (scales with $\sim Z^2$ for a screened atomic potential (*31*)). If a suitable stain is available and a selective staining can be assured staining is still used (*32–35*), especially if biology samples are studied (*31*) and tomography of polymers is performed (*34*). The problem of using stained samples is that on the one hand the availability of selective stains is rather limited and on the other hand staining often introduces structural artefacts (*36, 37*) and moreover a quantitative analysis of composition is hardly possible (*38*).

The so far discussed contrast mechanism is amplitude contrast. But soft materials often do not exhibit significant amplitude contrast. Due to the rich valence electron structure spatial modulation of the phase of an incident electron wave are an alternative source of contrast. Phase contrast is generated by the interaction of the incident electron wave with the positive Coulomb potential of an atomic nucleus. Phase contrast imaging is not used in this work and therefore not further discussed. A summary on the application of this techniques for studying polymers in TEM can be found in (*39*).

More often than phase contrast imaging, analytical techniques are used to study polymer systems. The inelastic interactions between the incident electrons and the material generate contrast for mapping compositions, chemistry and distribution of phases. This includes information of the core loss excitations, the low loss regime and also by X-ray generation.

2.3.1 Electron energy-loss spectroscopy

Electron energy-loss spectroscopy (EELS) gains its information from electrons passing through a specimen. Some of these transmitted electrons lose energy due to inelastic collisions; mainly electron-electron interactions with the sample. These losses contain information about the chemistry of the specimen and also the electronic structure of the atoms (such as bonding and valence states, nearest-neighbour atomic structure, dielectric response, free electron density, information on band gaps and also specimen thickness). Typically, the energy loss is separated in a low-loss and a high loss region.

Another way of using the effect of the characteristic loss of energy of electrons due to interactions with the sample is energy-filtered TEM (EFTEM). The main difference to EELS is that the energy filter is used to only allow electrons within a certain range of energy to pass through. These electrons are further used to form an image. So by doing EELS one achieves the whole energy spectrum of a certain sample position (mainly done in diffraction mode), doing EFTEM one obtains an image with electrons which lost an amount of energy defined by an energy selective slit (commonly done in imaging mode). Both techniques EELS and EFTEM rely on the same physical signal.

Low-Loss region

The low-loss region of an EEL spectrum contains the zero-loss peak and electrons with an energy loss <50 eV, per definition. The zero-loss peak contains primarily elastic, forward-scattered electrons and is the most intense feature of an EEL spectrum. It reflects the energy resolution of the spectrometer (its point-spread function), the stability of the high tension and the monochromaticity of the beam. It also contains electrons, which lost only a small amount of energy due to the excitation of e.g. phonons. The second most obvious features in the low-loss region are the plasmon peaks, which arise from collective oscillations of electrons. All features in the low-loss region are due to scattered electrons, which interacted with weakly bound electrons. These are conduction and/or valence band electrons of the sample and therefore information on the local dielectric constant or permittivity of a sample, the free electron density, the thickness, the band gap and inter- as well as intra-band transitions can be gained from these electrons.

High-Loss region

The high-loss and also called core-loss region contains electrons which lose energy by ionizing a sample atom. This is a direct interaction of the beam electrons with inner or core shells of the atoms in the sample and therefore the information can also be used for quantitative analysis. Generally the ionization cross section (correspond to the probability an ionization takes place) is relatively small compared to the plasmon excitation. Hence, we have relatively weak features (core-loss signals) on a rapidly decreasing background arising from electrons which have undergone plural-scattering events. An ionization edge also shows fine structure. We distinguish between the so called energy-loss near-edge structure (ELNES) arising from bonding effects and the extended energy-loss fine structure (EXELFS) arising from interaction with the surrounding of the ionized atom.

In Figure 4 a typical electron energy loss spectrum can be seen. In green the zero loss peak is shown the next intense feature is the Plasmon peak (blue) and at 284 eV the core loss signal of carbon (note the vertical scale is increased by 10^3).
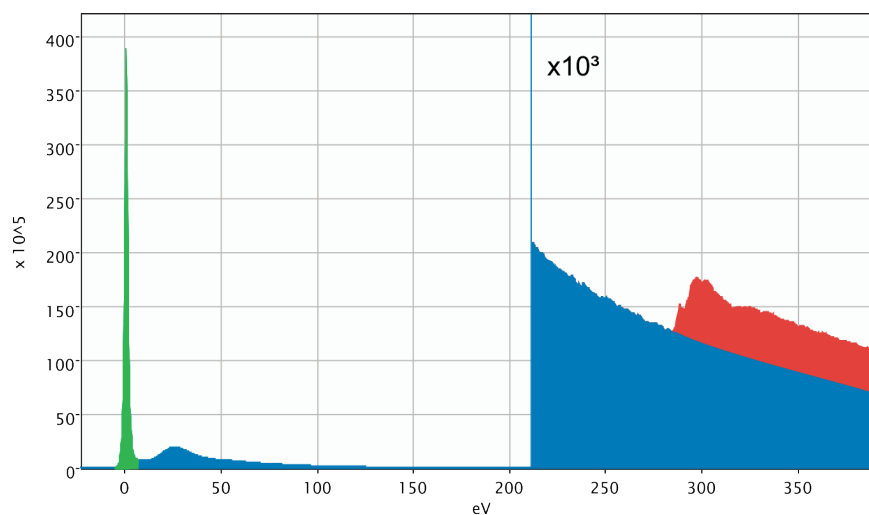
Figure 4: Electron energy loss spectrum. The high loss region is scaled-up by 10^3 for a better visibility.

EELS in light element analysis - Fingerprinting

Most elements found in polymers exhibit core loss excitations <1 keV which makes EELS especially suitable for light element analysis. But information can not only be gained by different chemical compositions but also from slight changes in the plasmon region as well as

in the ELNES region (this is called fingerprinting). Fingerprinting in the low-loss region focuses on differences in variations of band gap energies, the presence of structural elements like aromatic compounds or unsaturated bonds effective which affect the shape and position of plasmon peaks. Often the low-loss EELS range is the first choice because the inelastic electron scattering cross-section scales with $1/\Delta E$ (ΔE is the energy loss) which leads to a lower dose to achieve the same detected signal as using the core-loss signal (see e.g. a (*38*), (*40*)). Fingerprinting can also be done using the ELNES region which contains information on the electronic structure of the material and is mostly sensitive to the nearest-neighbour coordination. Theoretical simulations are possible but is highly demanding for complex molecules like polymers (*33, 41*).

In the following chapters different electron microscopy techniques are presented to systematically study organic electronic devices. This is done either with regard to the optimization of the manufacturing process or to gain a deeper understanding of the devices to contribute to the interpretation of the electrical characterization output.

2.4   TEM imaging

If a more precise analysis of a structure and/ or the composition is needed a TEM analysis is more suitable. Due to the fact that TEM is a method which works in transmission a thin sample is needed to perform a TEM analysis. If a site specific preparation is wanted the Focused Ion Beam (FIB) is the device of choice. The TEM sample preparation of organic materials is often closely linked to ultramicrotomy. In ultramicrotomy the sample is cut by a diamond knife and the slices float on a water surface. The next step is to somehow catch the slices with a TEM grid. The success of the technique not only depends on the skills of the operator but also on the suitability of the materials contained in the sample. The technique has its drawbacks especially if heterogonous material systems are prepared e.g. polymer layer separated by a metal layers. The preparation gets more and more challenging as the difference in the materials in the sample gets greater and artefacts like e.g. the delamination of layers are getting more frequent. Besides the introduction of artefacts due to the cutting process another aspect to be considered, using ultramicrotomy, is that the spatial resolution during preparation is limited. So usually many sample slices are cut and investigated with the hope to get a slice of the right sample site. This is the biggest advantage of the sample preparation using a FIB instrument. This site specific preparation is especially important if a part of a circuit should be investigated. This is the main reason why only TEM samples prepared using a FIB instrument appear in this work.

All FIB preparations were done with a FEI NOVA 200 dual beam system. If the charging of the sample was too severe an additional layer was applied prior to the FIB preparation (e.g. Pt/Pd ~80 nm with a Leica EM ACE600). In a next step a protective Pt layer was grown by an electron induced deposition to prevent the site of interest from ion beam damage. An even thicker layer of Pt was further deposited using the ion beam Figure 5b. In a next step two trenches were milled out (see Figure 5c). A microprobe manipulator was fixed to the lamella and the lamella was cut lose. It was in situ transferred to an Omniprobe grid and milled down to electron transparency (Figure 5e,f).

The gallium ion beam used for sample preparation also damages the sample (see also 3.6.1). Especially organic materials can be sensitive to beam damage. This damage can result in a loss of internal structures, such as crystallinity, up to the melting of materials during the preparation. The common ways to minimize this damage is to reduce the ion beam current and voltage as the lamella gets thinner during preparation to decrease the damaged surface layer. If very beam sensitive materials were prepared we used a special patterning technique, developed for beam sensitive material. This preparation technique uses a different patterning strategy of the ion beam to reduce the heat accumulation. For more information on the so-called smart interlacing technique please refer to the following references (*20–22*).
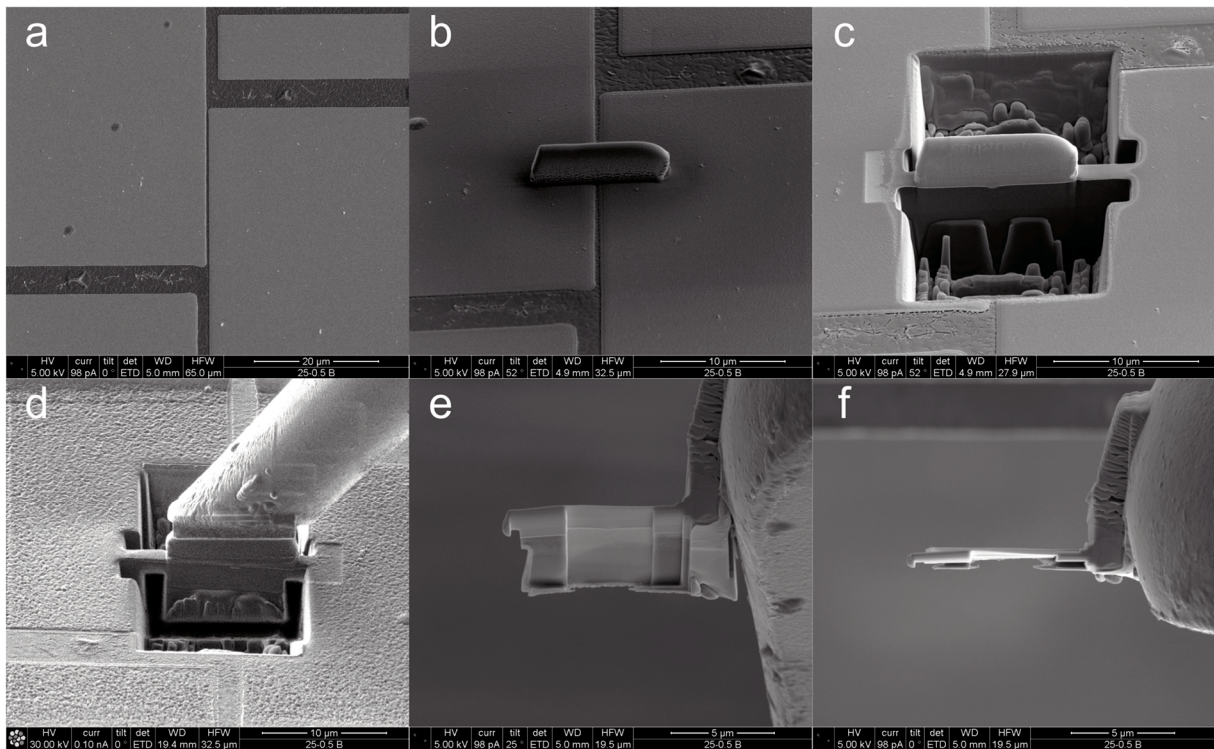
Figure 5: TEM lamella preparation using a FIB instrument. The images were acquired using an Everhart-Thornley detector. a) Site of interest. b) Pt protective layer. c) Two trenches are milled out on each side. d) The lamella is fixed onto a micromanipulator with which it is in situ transferred to the Omniprobe grid. e) f) Lamella fixed on the Omniprobe grid and thinned to electron transparency.

If the TEM lamella preparation was successful, an electron transparent lamella could be investigated in the TEM. In case of Figure 6 two self-aligned oTFTs can be seen (upper row: STEM HAADF, lower row: STEM BF). Both were manufactured by the same routine (PET, Cu, PVCi, Au) with the difference that the right oTFT Figure 6 a, c) was put in NMP (N-Methyl-2-pyrrolidon) to remove a remaining layer of a lift-off resist. The question was if other materials were also damaged by this solvent. The TEM investigation clearly revealed that the dielectric material shrunk by ~100 nm.
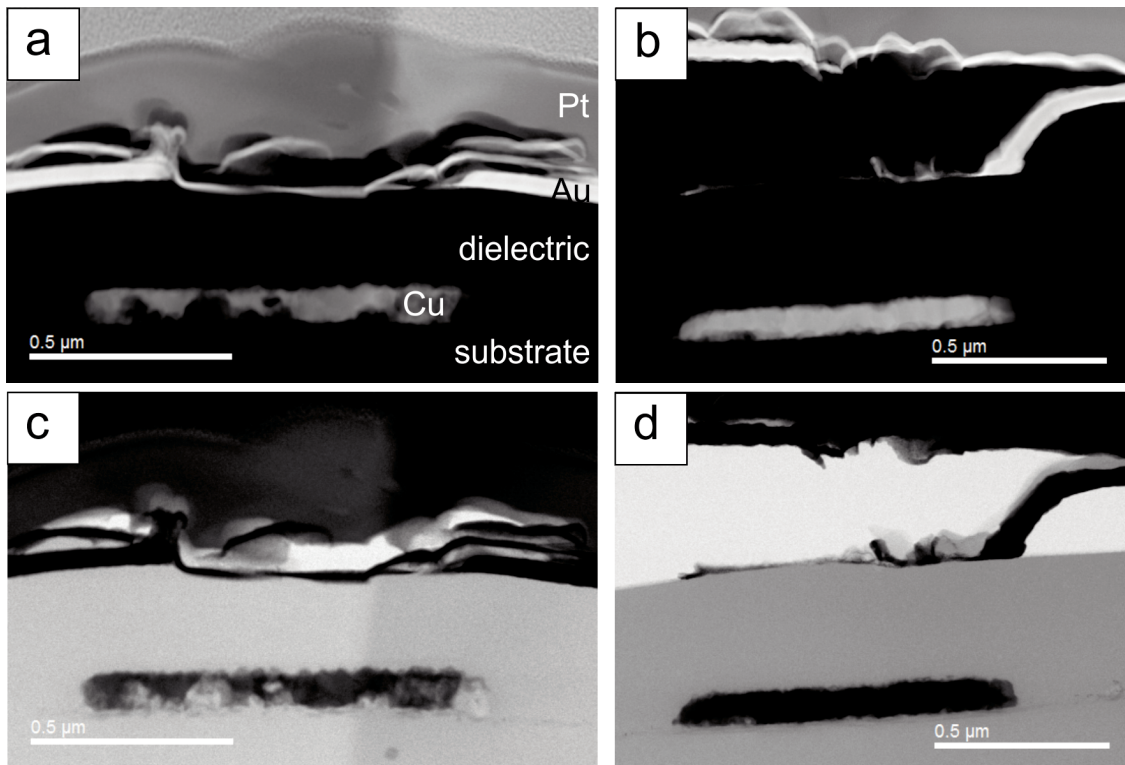
Figure 6: Self-aligned oTFT after treatment with NMP (right: a, c) and original oTFT (left: a, c). First row are STEM HAADF images and second row are acquired with a BF detector.

In another experiment the gate electrode material was changed from Al to Cu. If a new material is used its suitability to the manufacturing process has to be given. Moreover, its compatibility to the other materials also has to be given. So the question for the TEM investigation was how the shape of the Cu electrode looks like. Figure 7 shows that the Cu electrode had a trapezoid shape in cross section and that its edges are very well defined. The transition of the gate electrode material to Cu was made with regard to the production of an all-printable self-aligned transistor. The gate electrode material has to be opaque in the UV range because it acts as a photo mask in the self-aligned manufacturing approach. Al inks are still in development and therefore Ag and Cu represented two suitable candidates.
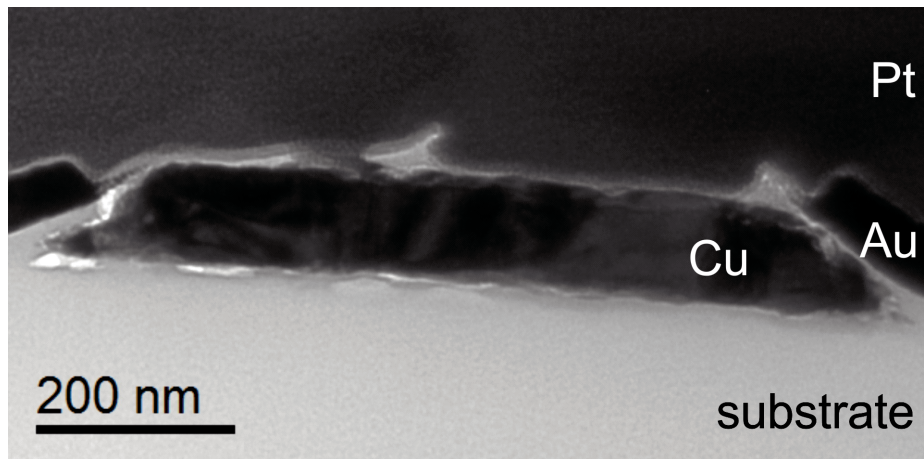
Figure 7: TEM image of a self-aligned oTFT with a copper gate electrode.

Using the TEM as an imaging technique a more detailed study of devices can be performed. The increase in resolution allows us the precise study of thicknesses and shapes of structures. Nevertheless, it always has to be borne in mind that only a very limited area is investigated. If the investigation is becoming more advanced, the analytic capabilities of an electron transmission microscope come into play.

2.5   TEM EDX

In Figure 8 already the HAADF contrast gives some information on the nature of the materials. Gold with the highest atomic number appears brightest and the polymer, mainly consisting out of carbon, the darkest. This was an oTFT, which was already electrically characterized, and probably due to the measurements the gold diffused into the channel region. In the image three points are marked; the red dot is on a very bright region in the channel the green dot on a darker one and the blue on a black region. This trend is reflected in the corresponding gold X-ray signal. The gold L signal goes down from red to green to blue.
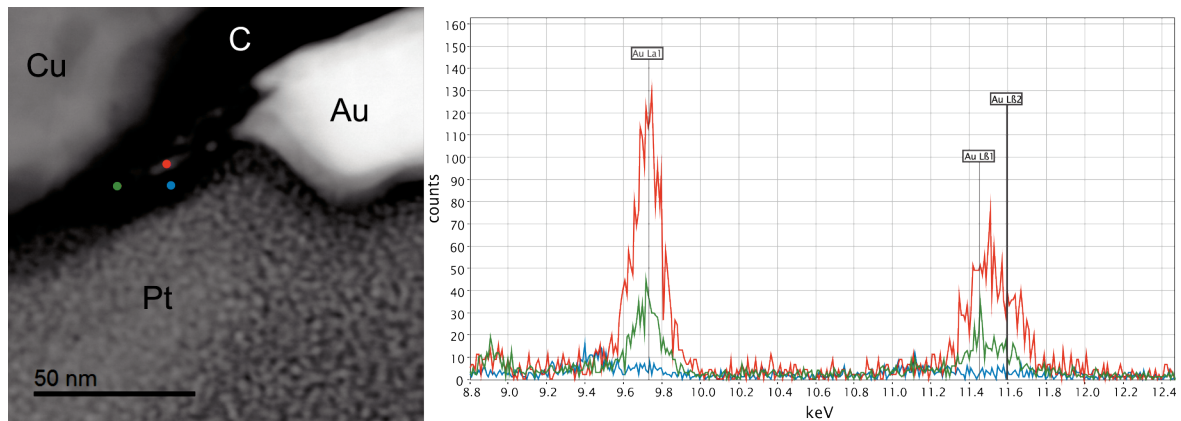
Figure 8: Left: HAADF image of an oTFT. The points show the positions were the EDX spectra were recorded. Right: EDX spectra at different positions.

If the materials get more similar in composition the analysis using the TEM as just an imaging tool is not sufficient. In Figure 9 an oTFT manufactured of all printable materials is shown. As a substrate a PET foil was used. The gate electrode material was silver. The dielectric material was PVCi and as source and drain electrode PEDOT:PSS was used. The semiconductive layer was pentacene. In Figure 9b a STEM BF image can be seen. The only layer which clearly can be distinguished is the silver gate electrode but all other materials appear to be similar. Figure 9a,b are two HAADF images of the left and right overlap region. To determine how big the overlap of the source and drain electrode in respect to the gate electrode is EDX was used. In Figure 9a,b as coloured insets the extracted Pt, S and Ag signal can be seen. The transistor had on both sides a negative electrode overlap. In the lower row of Figure 9 the extracted signals can be seen; Pt L @ 9.44 keV, S K @ 2.31 keV and Ag L @ 2.98 keV as well as the RGB overlay.
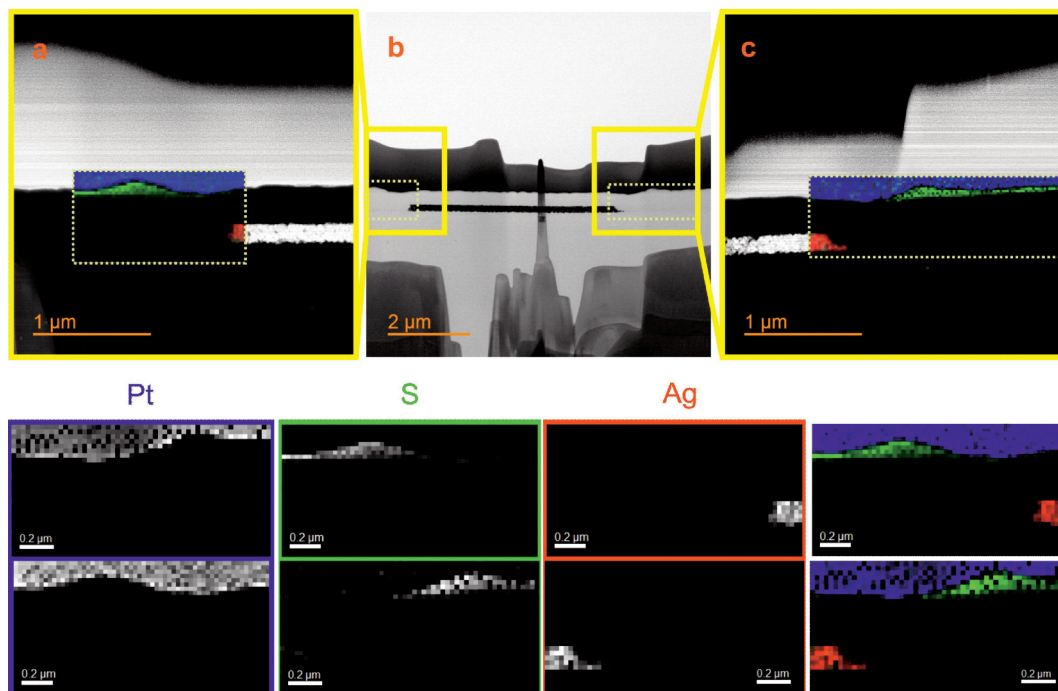
Figure 9: The top row shows two HAADF STEM images of the overlap region (a, c) and a BF STEM image of the whole channel region (b). The coloured insets correspond to data gained by EDXS SIs. The original extracted signal can be seen in the second (left side of the channel) and third row (right side of the channel). From left to right the extracted EDXS Pt, S and Ag Signal can be seen as well as an RGB image (Pt- blue, S – green, Ag- red).

2.6   TEM EELS

Similar to EDXS shown before, EELS can also be used to differentiate layers by their composition. An all polymer layer stack was produced. It consisted of four different polymers on a Kapton substrate. Two of the polymers are used as dielectric material PVCi and BCB whereas PEDOT:PSS is used as a conductive polymer as already shown in the example before. In this sample no metal layers were applied to assure the separation of the organic layers. Due to the advanced FIB preparation no intermixing of the polymer layers occurred (e.g. no sulphur of PEDOT:PSS was found in the adjacent layers). All five polymers are nicely separated as can be seen in Figure 10.
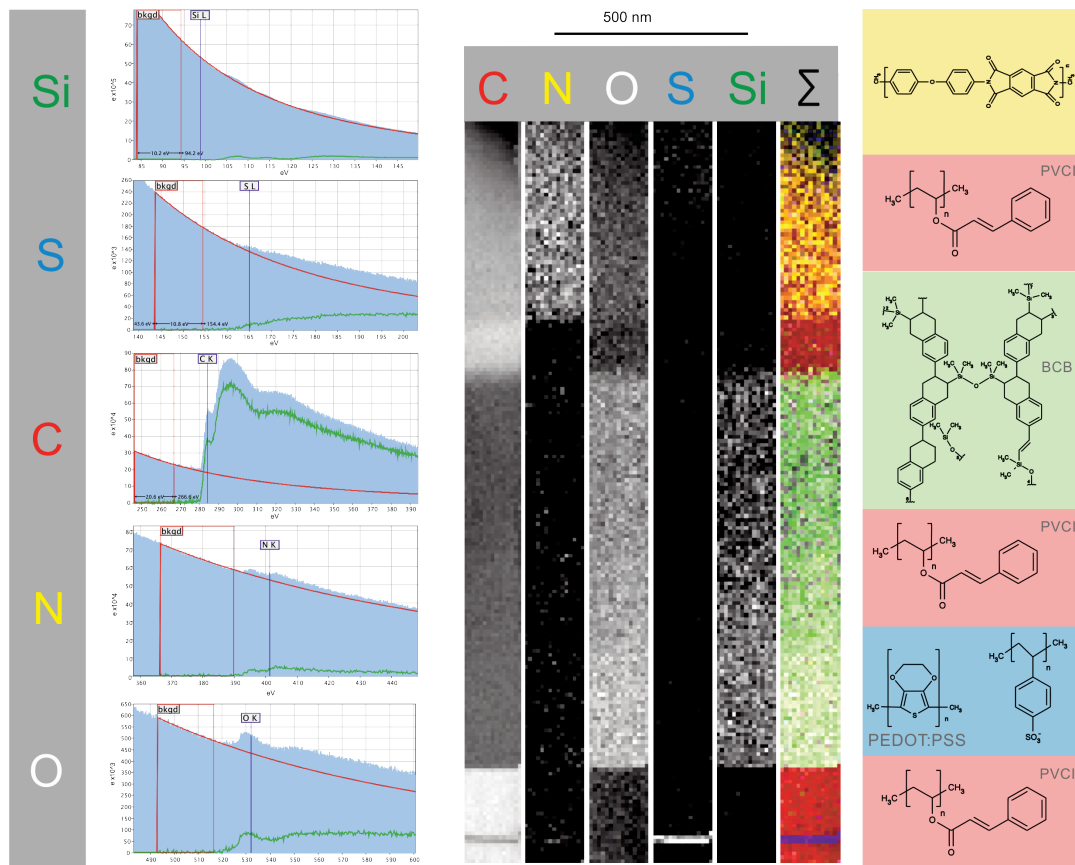
Figure 10: Left: Extracted core-loss edges of Si, S C, N and O of an EEL spectrum image of an all polymer layer stack. In blue the original spectrum is shown, the background fit in red and the background corrected core-loss signal in green. The layer stack consists of (bottom to top) PVCi, PEDOT:PSS, PVCi, BCB, PVCi, Kapton (PI). Middle: The extracted core-loss signals over the spectrum image are shown as well as the super-imposed elemental information (C…red, N…yellow, O…white, S...blue and Si…green). Right: The chemical structures of the used materials are shown.

To distinguish different polymer layers electron energy loss spectroscopy provides more possibilities besides the difference in elements. In Figure 11 a layer stack can be seen. It consisted of a PET substrate, a photo resist layer and a PEDOT:PSS layer. All polymer layers were separated by Au/Cr layers. This sample was produced to study if it would be possible to distinguish between the polymer layers. To prevent any preparation artefacts (such as an intermixing of the layers) metal layers were applied as intermediate layers. In Figure 11a a HAADF overview image of the sample can be seen. The metal layers can clearly be distinguished from the polymer layers by contrast. In Figure 11b an EDXS SI of the layer stack was made. Elements like Cr, Au, S and O can easily be identified. The chromium layer was

oxidized as could be expected. In the RGB image the Cr (green), Au (blue) and S (red) signals are superimposed. Using only EDXS a distinction between all polymer layers would not have been possible. But if EELS was used as an additional method a distinction could be made. Therefore, a closer look on the C-K edge was taken (Figure 11c). ELNES fingerprinting is a common (*31*) practice in material identification. Even though the near edge structure is directly influenced by the electronic structure of the material an interpretation of a real spectrum is still challenging. To be able to interpret the ELNES atomic simulations would be needed. In case of polymers the structures are far too complex to perform simulations. Therefore, often a simple comparison of the shape of e.g. the C-K edge is used. In Figure 11c the carbon edge of all three polymers (PET, photo resist, PEDOT:PSS) was extracted. Slight differences of the π* and σ* peak position and intensity can be seen. Three different energy regions are marked in Figure 11c. These regions were extracted from the whole SI and in Figure 11d ratios of the π* peak and the gap region as well as the σ* and π* peak region can be seen. Moreover, a Gaussian peak was fitted to the π* peak, which marks the onset energy of the carbon edge *E* (π*), and the center of the Gaussian is plotted in Figure 11d *E* (π*). If the ratios and the onset energy are considered we can distinguish between all three different polymer materials without any further analysis.
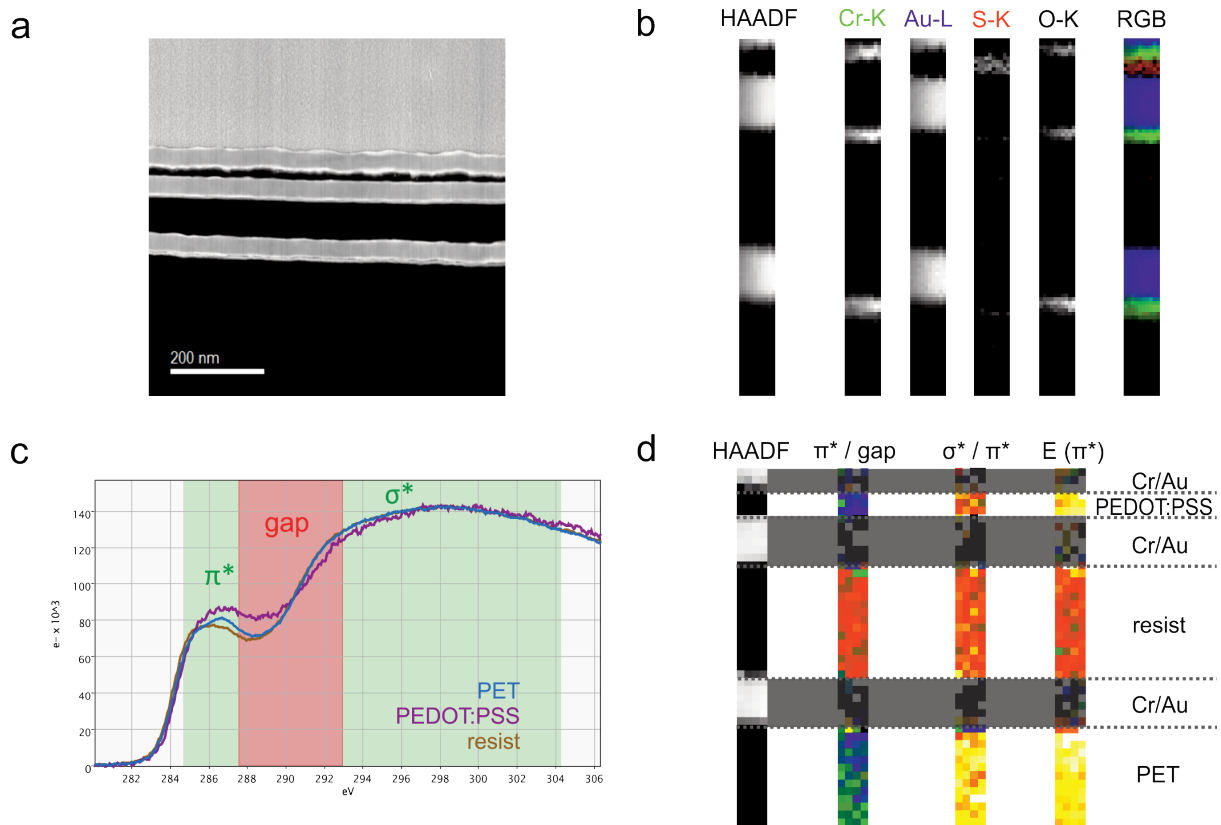
Figure 11: a) HAADF image of a polymer layer stack. b) HAADF image of SI position as well as extracted EDX signals of Cr-K, Au-L, S-K and O-K. In the RGB image the Cr (green), Au (blue) and S (red) signal are superimposed. c) Extracted C-K edge signal for different polymer layers (PET in blue, PEDOT:PSS in purple, resist in brown) with the definition of integral regions for ratios in d). d) HAADF image of SI position. Ratios of different region of the C-K-edge: π^*/ gap and σ^* /π^* ratio maps as well as the onset energy map of the π^* peak ($E(\pi^*)$).

The distinction of polymers by considering the shape of the C-K edge is not always possible. It depends on the chemical differences of the polymers, hence the bonding conditions of the carbon. Not only the core loss region is of interest if polymers should be differentiated but also the low energy region can provide information. The low loss region mainly provides electronic properties of the materials. In Figure 12 the thickness of a dielectric material (PMMA) could be determined by analysing the position of the bulk plasmon. A Gaussian function was fitted to the bulk plasmon. In Figure 12a the center of the fit can be seen. In Figure 12b the extracted low loss region of the dielectric (PMMA) and the semiconductor (pentacene) is shown. In Figure 12c an intensity profile is extracted from Figure 12a, marked by the orange rectangle and a dielectric layer thickness of about 64±5 nm could be measured.
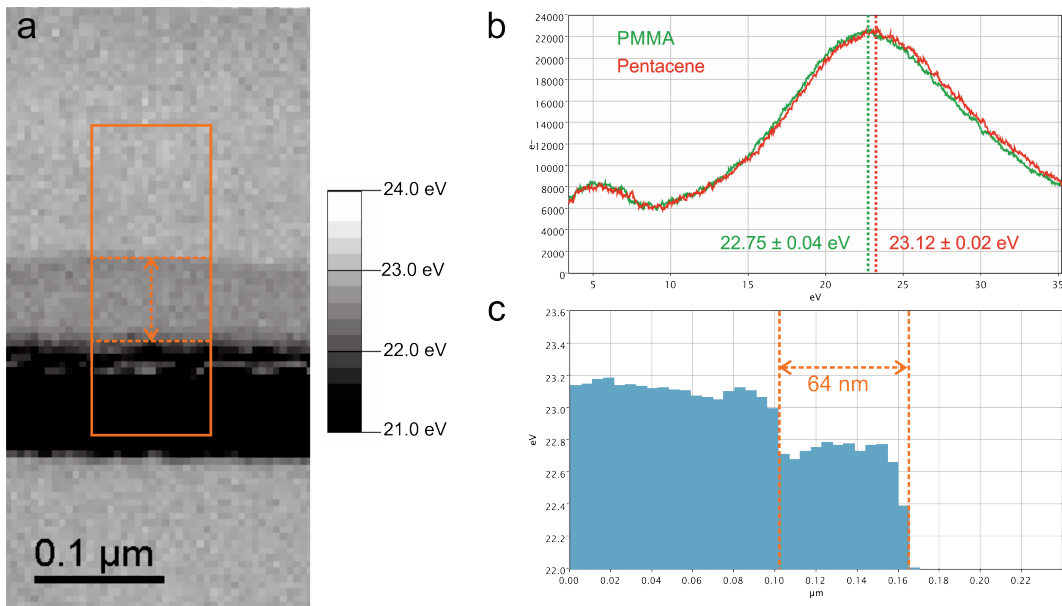
Figure 12: a) Center of fitted Gaussian function over the whole SI. The profile region shown in c) is marked in orange; b) extracted low loss EEL signal of PMMA (green) and Pentacene (red). The center of the Gaussian fit is also marked (given by the mean and the standard deviation over the corresponding regions in a)). c) Profile over the in orange marked region in a. A layer thickness of 64 ±5 nm can be determined.

Especially if the low loss region is used to determine thicknesses of layers one has to keep in mind that the spatial resolution decreases at lower energy losses. This is due to the effect that a beam electron passing by a sample atom in some distance already can transfer some energy. This can be described by the following equation giving the diameter, which contains 50% of the inelastic intensity.

$$(d_{50})^2 = \left(\frac{0.5\lambda}{\theta_E^{3/4}}\right)^2 + \left(\frac{0.6\lambda}{\beta}\right)^2 \qquad \textbf{(2.1)}$$

λ…   Mean free path

θ…   Characteristic scattering angle

β…   Collection angle

Using this equation an energy loss of 20 eV would lead to a value for d_{50} of 2 nm (at 200 keV acceleration voltage).

2.7   EFTEM

As already described EFTEM is also used for the analysis of polymer samples. One can either use compositional differences as e.g. (*42–45*) or differences in the low-loss region (*46–49*) to distinguish between phases. In Figure 13 an oTFT is shown with a very thin dielectric layer on top of the gate electrode. The three window method was applied to produce the elemental maps. Therefore two images are acquired at energy windows before the elemental edge and one after. The two pre-edge windows are used for a background fit which is further subtracted from the post-edge image (see e.g. (*31, 50*)). In Figure 13 one can nicely see that the aluminum gate electrode is oxidized and that the substrate coating as well as the enhancement contains oxygen rich areas. Looking at the carbon image it can be seen that a thin dielectric layer (>10 nm) is covering the whole gate electrode.
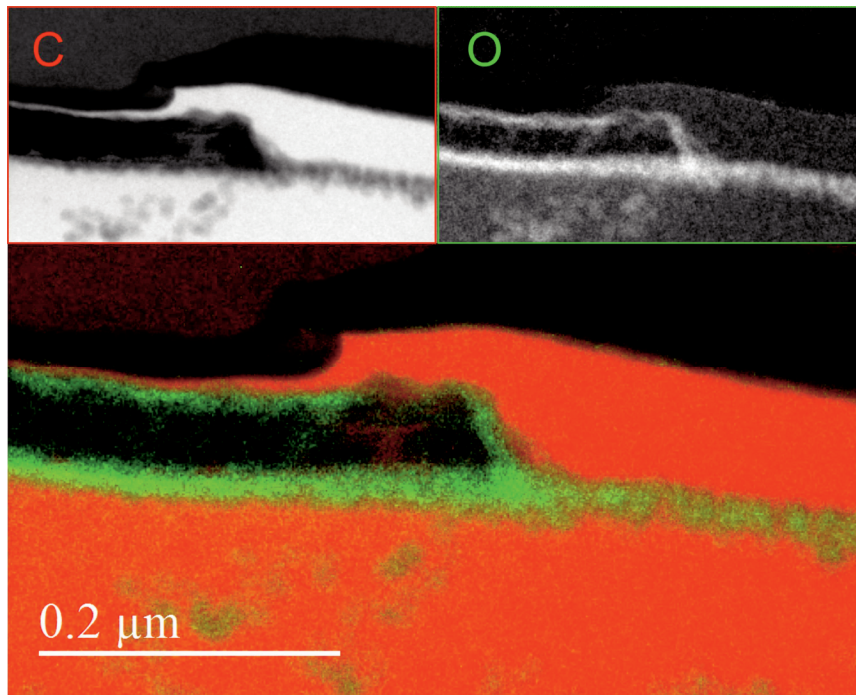
Figure 13: Elemental map of carbon (top left) and oxygen (top right). Superimposed elemental maps (carbon in red, oxygen in green).

To reduce the recording time and thereby the electron dose one can also use the low-loss region to gain information on the sample. The sample presented here was studied using a 2 eV broad energy selective slit. The slit energy was varied between 3 eV to 29 eV. The sample was an oTFT on an enhanced polycarbonate substrate, an aluminum gate, the dielectric material was PMMA, the source/drain electrodes were made out of gold, as semiconductive

material pentacene was used. The aim of this analysis was to make the dielectric material visible to estimate its thickness.
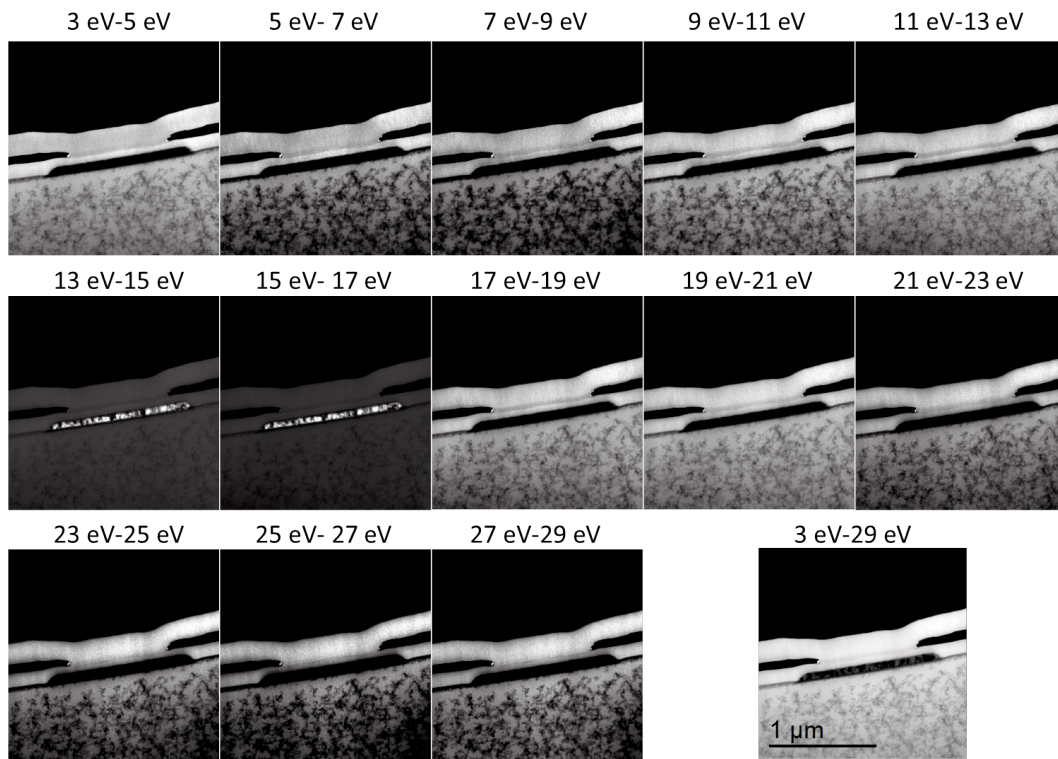
Figure 14: EFTEM SI each image was recorded with a 2 eV slit from 3-29 eV. The last image is the sum from 3 eV to 29 eV.

The difference between pentacene and PMMA can best be seen in an energy window from 3 eV – 7 eV, this energy-loss range corresponds to π electron excitations. At an energy-loss around 15 eV aluminum exhibits a plasmon excitation. If an intensity profile is drawn over the area indicated in the inset in Figure 15 the dielectric layer thickness can be determined to be around 64 ±5 nm. The profile is drawn over each energy slit positions and in most energy ranges the layer is visible.
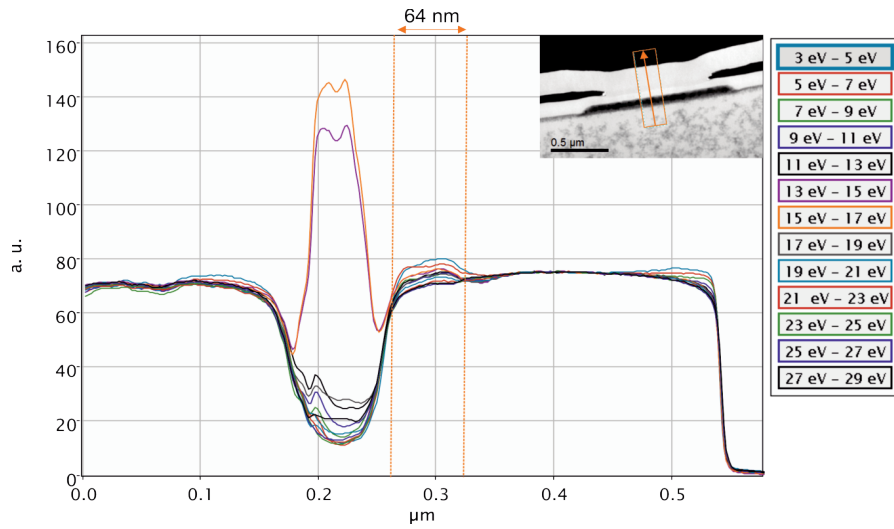
Figure 15: Profile at the area marked in the inset at each energy loss image. The intensity profiles of each EFTEM image are plotted at the marked position (3 eV to 29 eV). The dielectric layer thickness of around 64 ±5 nm is marked in the profile.

3 The ζ-factor method

Energy Dispersive X-ray Spectrometry (EDXS) is a well-established technique in analytical TEM, which is mainly used for heavier element analysis. This is due to two effects: Firstly, the probability that an X-ray count is generated is much higher for higher Z-elements (see 3.1.1) due to the fluorescence yield. Secondly, the amount of absorption in the specimen largely increases for low Z elements. If quantitative EDXS analysis needs to be performed mainly the ratio approach following the well-known Cliff-Lorimer (*51*) method is used. In most application cases absorption inside the specimen is neglected, because the mass-thickness of the specimen is generally unknown. Neglecting the absorption of characteristic X-rays in the sample limits the application of this method to systems containing a mixture of heavy and light elements (*52*). In principle, the Cliff-Lorimer method could correct for the absorption in the sample if the composition of the sample, hence the mass thickness, would be known. Quantitative EDXS, accounting for the absorption of characteristic X-rays by iteratively gaining the mass thickness was implemented in EDXS quantification (*53–55*) and in 2006 Watanabe and Williams (*9*) published the final version of the so called ζ-factor method. The ζ-factor method yields not only the elemental concentrations but also the mass-thickness of the specimen. This makes this technique suitable for quantitative light element analysis as a proper absorption correction can be performed.

The following chapters first give a short overview on EDXS and EDXS quantification in general. In a next step, the ζ-factor method is explained in more detail and finally practical aspects of EDXS quantification as well as results are discussed.

3.1 Energy dispersive X-ray spectrometry

In the next chapters a short overview is given of the factors which determine the appearance of a typical EDX spectrum, bremsstrahlung and characteristic X-rays. Moreover, a focus is especially placed on aspects important considering X-rays of light elements.

3.1.1 The X-ray spectrum

Generally, an X-ray can be emitted if an ionized atom returns to its ground state. The high energy electron beam in a TEM can lead to the ejection of an inner shell electron of an atom if the transferred energy is high enough. The atom can return to its ground state by filling the generated vacancy with an outer shell electron. This transition can either lead to the generation

of an Auger electron or an X-ray. The ratio of X-ray emission to Auger electron generation is described by the fluorescence yield (ω) and can be linked to the atomic number with the following approximation:

$$\omega = \frac{Z^4}{a + Z^4}$$

(3.1)

whereas, α is ~10^6 for K shells. It can clearly be seen that the probability for generating an X-ray count increases with increasing atomic number (Z^4) (*31*) which can be seen as a disadvantage for light element analysis using EDXS.

Generally, a sample emits two kinds of X-rays: characteristic X-rays and Bremsstrahlung X-rays.

Bremsstrahlung X-rays

The Bremsstrahlung X-rays arise from inelastic interaction of an incoming beam electron with a sample nucleus. The incoming electron suffers from a change in momentum due to the Coulomb field of the nucleus and may emit an X-ray. The energy of this X-ray depends on the interaction of the electron with the nucleus and can have any value up to the initial energy of the electron.

To describe the bremsstrahlung production usually the Kramers (*56*) cross-section is used:

$$N(E) = \frac{KZ(E_0 - E)}{E}$$

(3.2)

$N(E)$… number of bremsstrahlung photons of energy E

E_0… energy of incoming electrons

K… Kramers' constant

Z… atomic number of the ionized atom

For modelling a background Kramers' constant is expanded to Kramers' factor which accounts for several effects, e.g. the collection and processing efficiency of the detector, absorption effects in the specimen and Kramers' original constant (compare also (*31*)). The general approximated relation shows a dependency of the bremsstrahlung generation to the energy of the bremsstrahlung X-rays of ~$1/E$; so low energy bremsstrahlung is more likely. The probability that an incoming electron transfers all of its energy to an X-ray photon is rather small therefore the background gets lower at higher energies. The shape of the background

depends not only on the acceleration voltage but also on the specimen composition. Low energy X-ray photons are more easily absorbed therefore in the very low energy region the bremsstrahlung background is also small. The amount of the absorbed low-energy X-ray photons in the specimen is again a strong function of the specimen composition. Moreover, the detected bremsstrahlung also includes detector depended effects (type, detector window, contamination layer…). A typical background can be seen in Figure 16. For EDX quantification an appropriate method to gain only the characteristic X-rays, without the background, is essential.

Characteristic X-rays

Theoretically the X-ray generation within a specimen atom leads to the emission of a photon with a very specific energy. The energy is characteristic for the energy difference of the two involved shells of an atom. So if e.g. a hole is generated in a K shell and is filled with an electron of an L shell a K_α X-ray is generated per definition. We differentiated between an α_1 and an α_2, depending on which subshell of the outer shell the electron fills the hole (see e.g. (*31*)). In practice, if the energy is measured, the width of the characteristic X-ray peak is broadened to a Gaussian shaped peak. The broadening depends on the photon energy, the energy needed to create an electron hole pair (~3.7 eV for Si) (*57, 58*) in the detector, the Fano factor (~0.1 for Si) (*57, 58*) and the electronic noise of the detection system (*59*). These parameters determine the position and shape of the characteristic X-ray peaks. In Figure 16 a typical EDX spectrum is shown. A simulated spectrum (NIST DTSA-II Halley 2014-08-01 revision) (*60, 61*) of an Al_2O_3 sample can be seen. The red and the blue curve show the theoretical bremsstrahlung X-ray background. The red curve shows the background as generated. The blue curve shows a background as it is detected. In comparison to the red background the blue curve gives more realistic bremsstrahlung background because the absorption of low energy X-rays in the sample and in the detector layers is considered.

The characteristic X-ray signal is shown in green.
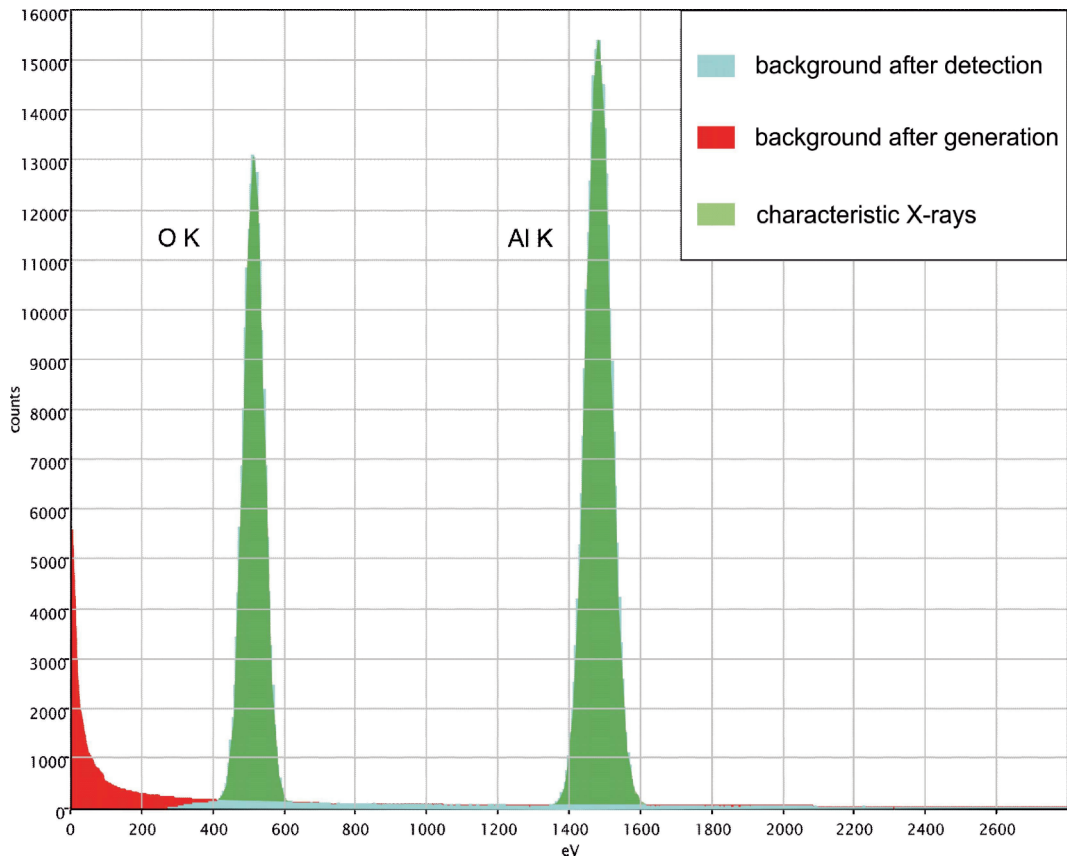
Figure 16: Simulated EDX spectrum of Al_2O_3. The background after detection is shown in blue, the generated bremsstrahlung background is shown in red and the characteristic X-ray peaks are shown in green.

3.2 EDXS quantification

The following chapters are giving an introduction to quantitative EDXS, the Cliff-Lorimer and the ζ-factor method.

3.2.1 Cliff-Lorimer method

Traditionally, the quantitative EDXS of bulk samples is mainly done by comparing the absolute X-ray intensity from an unknown sample to the absolute intensity from a standard, measured under the same instrumental conditions. In an iterative way corrections are made for the stopping power, back-scattering, X-ray absorption and fluorescence in the specimen. This procedure is called the ZAF-correction (*Z*… atomic number. *A*… absorption, *F*… fluorescence) and is still widely used in SEM EDXS in further developed versions. The main difference of EDXS in SEM and in TEM is the sample thickness, hence the interaction volume. So the X-ray intensity is not only a function of the composition but also a strong function of the local sample

thickness. To perform a reliable EDXS quantification with thin samples not only the probe current and the X-ray intensity have to be known but also the sample thickness at each analysis point. Therefore, in the TEM EDXS quantification it is common practice to work with a ratio technique, because the ratio of a sufficiently thin sample is not thickness dependent. In 1975 G. Cliff and G. W. Lorimer introduced the so called Cliff-Lorimer ratio technique (*51*). They assumed a sufficiently thin specimen so that incident electrons only lose a small amount of energy passing through the sample, assuming a negligible X-ray absorption and secondary X-ray fluorescence within the specimen. These conditions are called "thin film criterion". If the thin film criterion is fulfilled the ratio of characteristic X-rays is directly related to the composition of the specimen, the corresponding weight fraction ratio. As a proportionality factor, they introduced the k- or Cliff-Lorimer factor.

$$\frac{c_A}{c_B} = k_{AB}\frac{I_A}{I_B} \tag{3.3}$$

The k-factor accounts for the relative efficiency of X-ray production and also for detection related influences. It depends on the following parameters:

$$k_{AB} = \frac{(Q\omega a)_A}{(Q\omega a)_B}\frac{W_A}{W_B}\frac{\varepsilon_A}{\varepsilon_B} \tag{3.4}$$

W…   atomic weight

Q_A…   ionization cross-section

ω_A…   fluorescence yield

a…   relative transition probability

ε_A…   detector efficiency

The ionization cross-section is the probability that an atom gets ionized by an incident electron. The fluorescence yield is the ratio of ionization events, which lead to the generation of an X-ray. The relative transition probability takes into account if e.g. a K_α or a K_β X-ray is more probable.

Usually the k-factors are given relative to silicon. They can be determined experimentally for each system setup or theoretically by calculations from first principles. The k-factor is independent of the probe current for a single measurement but depends on the TEM EDXS system (influencing ε_A) and the acceleration voltage (influencing Q_A).

Theoretical k-factor calculations have a relative accuracy of ±10-20% which is mainly due to the uncertainties in the ionization cross-section and the detector dependent parameter (ε) (*31*).

An experimental determination of k-factors can give more accurate results but is laborious and also bares a lot of difficulties. Especially the availability of suitable multi-element standards is a challenge. Multi element standards with a well-known and homogenous composition which are stable throughout the preparation and analysis have to be found. The k-factors have to be measured at each high tension and microscope several times to improve statistics. For more information see standard text books on electron microscopy like e.g. (*31*). Here several approaches how to determine k-factors (*62–65*) are listed. Nevertheless, if the thin film criterion fails absorption correction cannot be neglected. For an absorption correction using the Cliff-Lorimer method the mass thickness of the sample has to be known. Ignoring absorption effects in light element analysis using the k-factor method alters the determined results significantly (*52*).

3.2.2 The ζ-factor method

The ζ-factor is also a proportionality factor, which relates the measured intensity I_A to ρt, C_A and D_e as follows:

$$\rho t = \zeta_A \frac{I_A}{D_e}_A \qquad (3.5)$$

$$D_e = N_e I_p \tau \qquad (3.6)$$

ρt…   mass-thickness (ρ… density, t…thickness)
ζ_A...   ζ-factor of element A
D_e…   electron dose
c_A…   concentration of element A
N_e…   number of electrons in a unit electric charge
I_p…   probe current
τ…   acquisition time

This relation is based on the following equation describing the measured X-ray intensity considering the thin film criterion (*9*):

$$I_A = N_v \frac{Q_A \omega_A \alpha_A}{W_A} c_A \rho t D_e \left(\frac{\Omega}{4\pi}\right) \varepsilon_A \qquad (3.7)$$

$$\zeta_A = \frac{W_A}{N_v Q_A \omega_A \alpha_A \left(\frac{\Omega}{4\pi}\right) \varepsilon_A} \qquad (3.8)$$

W...   atomic weight

N_v...   Avogadro's number

Q_A...   ionization cross-section

ω_A...   fluorescence yield

α_A...   relative transition probability

$\frac{\Omega}{4\pi}$...   detector collection angle in the whole space

ε_A...   detector efficiency

It can be seen immediately that the ζ-factor depends on similar parameters as the k-factor does. The relation between ζ-factor and k-factors is:

$$\frac{A}{B} = \quad {}_{AB} \qquad (3.9)$$

A theoretic ζ-factor calculation would suffer from even bigger uncertainties compared to a k-factor calculation. Ω and ε_A have to be known for the used detector system and ω_A, Q_A and α_A have to be measured or calculated. A good summary on available, calculated values for ω_A, Q_A and α_A can be found in (*66*). For the fluorescence yield values of (*67–69*) are often used. Values for the ionization cross section can be taken e.g. from the NIST database (*70*) based on work by (*71, 72*). Generally, the uncertainties for the fluorescence yield vary between 10-30%, depending on the considered shell. For the ionization cross section an extensive evaluation on calculated values can be found in (*73*).

For an experimental determination of ζ-factors one has to know the used electron dose, the density and the composition of the standard. Because no ratio approach is needed also pure element standards can be used. The concentration and the density are needed to calculate the mass-thickness of the sample. An overview of different approaches in literature and a discussion of difficulties arising, especially with the mass-thickness are given in the following chapters (chapter 3.3.1 and 3.7).

So far the only difference in determining k- or ζ-factors is, that for an experimental determination of ζ-factors one would need to measure the electron dose and know the mass-thickness but pure element standards can be used. For a calculation of the sensitivity factors the ζ-factors would additionally depended on parameters like the solid angle and Avogadro's number.

The big advantage the ζ-factor method brings can be seen if a quantification of a specimen is considered. If for example a binary system is to be quantified the following approach is chosen.

The intensity above background of both elements is determined, and an initial mass thickness is calculated.

$$\rho t = \frac{\zeta_A I_A + \zeta_B I_B}{D_e} \ \ with \ \ _A = \frac{\zeta_A I_A}{\zeta_A I_A + \zeta_B I_B} \ and \ c_B = \frac{\zeta_B I_B}{\zeta_A I_A + \zeta_B I_B} \tag{3.10}$$

$\rho t\ldots$	mass-thickness ($\rho\ldots$ density, $t\ldots$ thickness)
$\zeta_A, \zeta_B\ldots$	ζ-factor
$I_A, I_B\ldots$	intensity above background
$D_e\ldots$	electron dose
$c_A, c_B\ldots$	concentration

This initially determined mass-thickness is used to calculate the absorption of each element following an approach given by (74) (which is in this form only valid for a plane, parallel-slab specimen geometry).

$$A_{A,sp} = \frac{(\mu/\rho)^A_{sp}\, \rho t\, cosec\, \alpha}{1 - exp\left[-(\mu/\rho)^A_{sp}\, \rho t\, cosec\, \alpha\right]} \tag{3.11}$$

$(\mu/\rho)^A_{sp}\ldots$	mass absorption coefficient of the characteristic X-ray line in the specimen
$\alpha\ldots$	take-off angle
$\rho t\ldots$	mass-thickness

The correction term is included in (3.10):

$$\rho t = \frac{\zeta_A I_A A_{A,sp} + \zeta_B I_B A_{B,sp}}{D_e}$$

(3.12)

$$c_A = \frac{\zeta_A I_A A_{A,sp}}{\zeta_A I_A A_{A,sp} + \zeta_B I_B A_{B,sp}}, \; c_B = \frac{\zeta_B I_B A_{B,sp}}{\zeta_A I_A A_{A,sp} + \zeta_B I_B A_{B,sp}}$$

And can easily be expanded for multiple element systems:

$$\rho t = \sum_i^N \frac{\zeta_i I_i A_{i,sp}}{D_e}, \; c_A = \frac{\zeta_A I_A A_{A,sp}}{\sum_j^N \zeta_i I_i A_{i,sp}}, \; ..., \; c_N = \frac{\zeta_N I_N A_{N,sp}}{\sum_j^N \zeta_i I_i A_{i,sp}}$$

(3.13)

The calculated mass-thickness is used to calculate a new composition of the specimen. This new composition is again used to calculate the absorption of each characteristic line in the specimen and so on and so forth. Usually it takes about 10-15 iterations until the composition converges to less than 0.001 wt% difference in composition and 0.01 nm difference in specimen thickness (see (9) for more information). Finally, one achieves an absorption corrected concentration as well as the mass-thickness of the specimen, which further can be used e.g. for EELS quantification as was demonstrated in (75).

3.3   Using the ζ-factor method

3.3.1   Approaches in literature for ζ-factor determination

In this chapter a short review is given on the different approaches found in literature to experimentally determine ζ-factors.

Watanabe et al. (9) proposed a ζ-factor determination using the NIST standard SRM 2063a (76) or pure-element standards (Al and Ni thin films produced by evaporation). The SRM 2063a is a glass standard containing five elements (Mg, Si, Ca, Fe, O and Ar) in a certified concentration. Using this standard an interpolation/ extrapolation of ζ-factor for K-lines of all elements, following an approach based on Zemyans parameter-optimization (77, 78), was made. The SRM 2063a is also used by (79, 80). Using this standard faces two main uncertainties: on the one hand the thickness was measured by profilometry to be 76 nm ±4 nm (confidence limit of 95%) and the density was calculated to be 3.1 g/cm³ (±0.3 g/cm³ 95% confidence) from the measured thickness, area and mass of the thin-film deposition. Both the thickness and the density are not certified. On the other hand only 5 points are measured over the whole periodic table with oxygen having the lowest ($Z = 8$) and iron the highest ($Z = 26$) atomic number. Especially, the chosen ionization cross-section during parameter optimization

has a huge influence on the interpolation/ extrapolation of ζ-factors. This is particularly sensitive for ζ-factors for light elements and elements with an atomic number >30. The accuracy of the fit would improve significantly if more than one element with an atomic number <10 and >20 would be measured (compare (*7, 9*)). Rathi et al. (*81*) describe a standard-based method of the combination of ζ-factor with multivariate statistical analysis applied to III-V alloy films. Other groups try to find a different approach to somehow perform reliably thickness determination (*75, 82*) or rather to bypass it by exactly knowing the analysed volume (*83, 84*) by using a tomography approach and nanoparticles. In (*84*) only heavy elements like Au, Ag and Pt are considered and therefore absorption effects are neglected.

3.4   ζ-factor determination

Our approach for the ζ-factor determination is explained in the following. The intention was to use pure element standards to be sure of the concentration and to bypass the thickness determination by a geometrical approach (following Kothleitner et al. (*75*)); to prepare a rotationally symmetric cone and a plane, parallel-sided lamella out of a bulk sample. Due to the known geometry of the cone the mean free path (λ) can be determined experimentally by EELS. By knowing λ of the material one can calculate the absolute thickness. The lamella is used to measure the ζ-factor using conventional absorption correction procedures (compare (3.11)) valid for the plan parallel shape of the lamella (following (*9*)). Due to the fact that the focus of this thesis is on light element analysis the sole use of pure element standards is not feasible. Therefore, also multi-component standards had to be considered.

In this work, we present the determination of 3 ζ-factors for the elements Si, O and Al. Four different materials were used as standards: single crystalline Si and Al, and crystalline Al_2O_3 and SiO_2. The aim of this ζ-factor determination was to study in great detail all aspects influencing the determination of sensitivity factors on a Super-X system, to be able to develop a procedure to reliably determine ζ-factors.

Generally, the gained sensitivity factors depend strongly on the counts generated (per time and beam current), the counts collected and the evaluation of these counts. Figure 17 illustrates all these parameters influencing the determined ζ-factors.
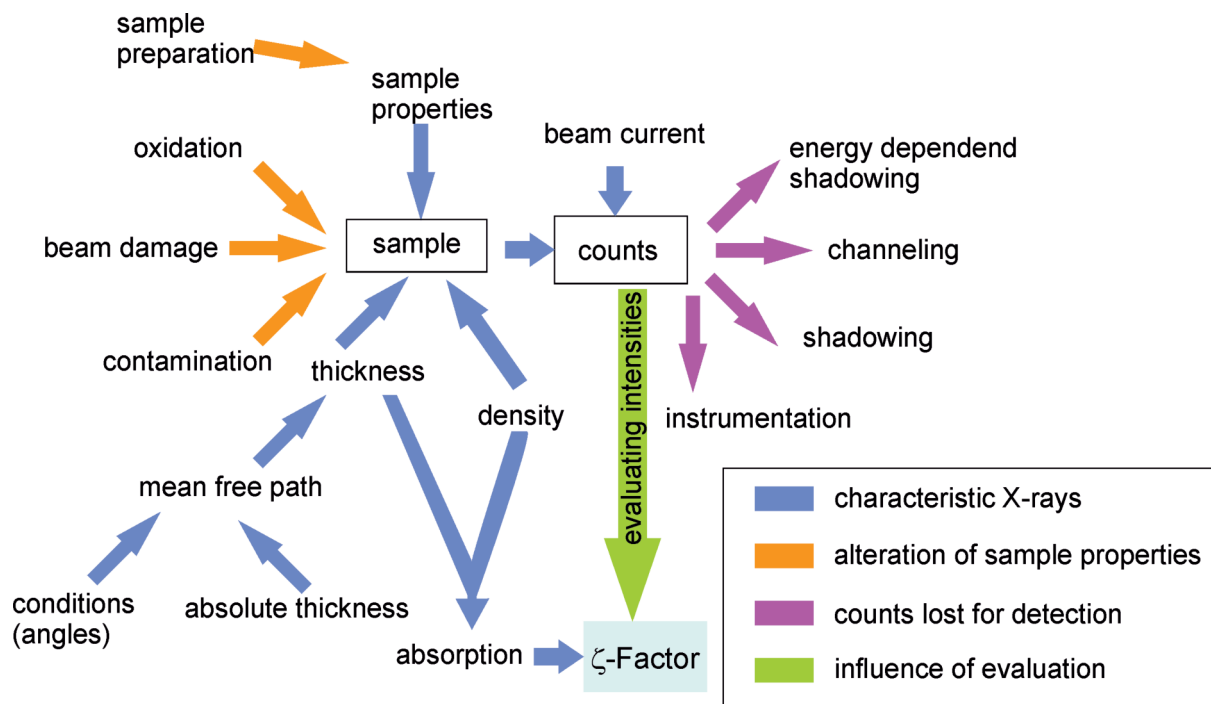
Figure 17: Parameters influencing the determined ζ-factor.

All the connections shown in blue symbolize the aspects influencing the generation of X-ray counts. This includes sample properties and acquisition conditions. In orange effects altering the sample properties and thereby the generated X-ray counts are shown. The purple arrows indicate effects associated to the difference in counts generated and counts detected. The green arrow represents the direct impact that an evaluation of the counts has on the determined sensitivity factors.

The following chapter will start out with a closer consideration on the chosen standard materials, its preparation and the used equipment. The determination of the thickness of the used TEM samples is necessary for ζ-factor determination. A short discussion on conditions which can alter the gained counts, due to an altered sample (beam damage, contamination…) and due to instrumentation (beam current measurements, acquisition time, etc.), is given. The next section is all about the intensity determination. In the end, the chapter merges into a more extensive consideration of influences like energy depended shadowing and shadowing in Figure 17.

3.5   Sample preparation, practical considerations and used instruments

The experimental determination of ζ-factors is different to the determination of k-factors and therefore poses other challenges. The biggest problem in a reliable experimental k-factor determination is seen in the availability of good standard specimens. In case of the ζ-factor method, in principle, pure-element standards can be used. Pure-element standards are easy to produce and do not change composition during specimen preparation and under electron irradiation. The problem with light element standards is the limited availability of pure-element standards.

We considered several samples as standard materials. The main focus was, that the concentration was known with high accuracy, if the usage of a pure element standard was not possible. The density, hence the structure, should also be known and homogenous. Therefore, before a material was used as a standard, we did some preliminary investigations, such as an inspection in a SEM with EDX (Zeiss Ultra 55, EDAX Octan SDD) or an XRD measurement. Finally, we decided to use pure-element standards (e.g. sputter targets), single crystalline samples such as e.g. silicon or samples taken out of a SEM mineral standard (SPI, Structure Probe Inc., West Chester, USA).

In this work four materials are presented as an example: Si, SiO_2, Al and Al_2O_3. Whereas silicon and aluminum oxide (α-aluminum oxide) were taken from a single crystal, the aluminum was a piece of pure aluminum and the SiO_2 (Quartz) was taken from the SPI standards. All densities were taken from the NIST database (*85*) or the RÖMPP lexica (*86–88*) and are listed in Table 1. The mass attenuation coefficients used for the absorption correction were also taken from the NIST database.

Table 1: Density and mass attenuation coefficient used for calculations.

	Density	Mass attenuation coefficient
	g/cm³	cm²/g
Si	2.33	Si-K: 330
Al	2.70	Al-K: 371
SiO_2	2.65	Si-K: 680 O-K: 4139
Al_2O_3	3.98	Al-K: 920 O-K: 3546

As already described before (3.3.1) we decided to follow the approach of (*75*); using FIB milled samples. Therefore, each Omniprobe grid was cleaned before FIB preparation in the plasma cleaner for 10 min (oxygen argon plasma, 30:70). Only copper Omniprobe grids were used because of the better defined shape of the edges compared to molybdenum grids. A separate Omniprobe grid for the rod and the lamella was used to be as close to the center of the holder as possible. It was tried to mount the lamella on the position marked in Figure 18b to avoid shadowing by the geometry of the Omniprobe grid. All dimensions listed in Figure 18 are taken from measurements with an infinite focus microscope from Alicona.
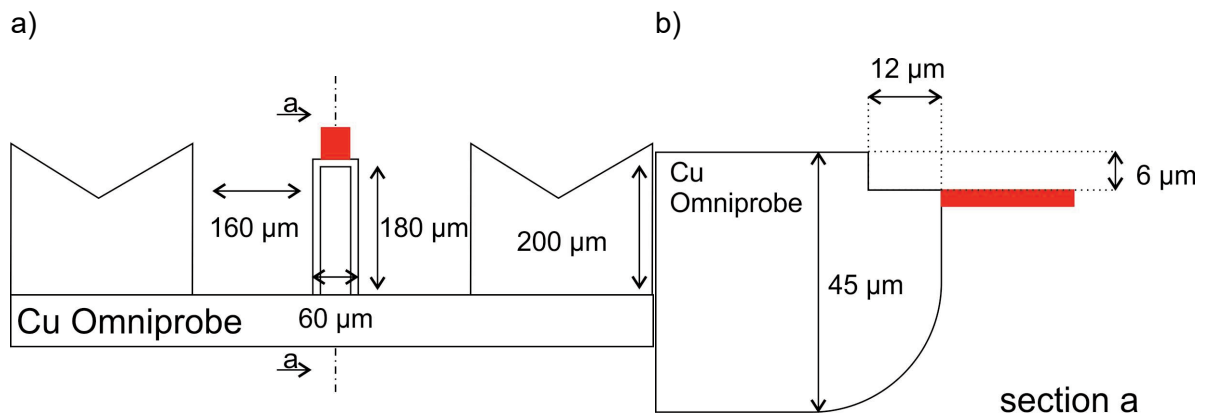

Figure 18: a) Top view of a copper Omniprobe grid. b) Cross section a. The specimen is schematically drawn in red.

In Figure 19 HAADF images of a typical set of samples for ζ-factor determination is shown. In this case the lamella (Figure 19a) and the rod (Figure 19b) are made from a bulk silicon sample.
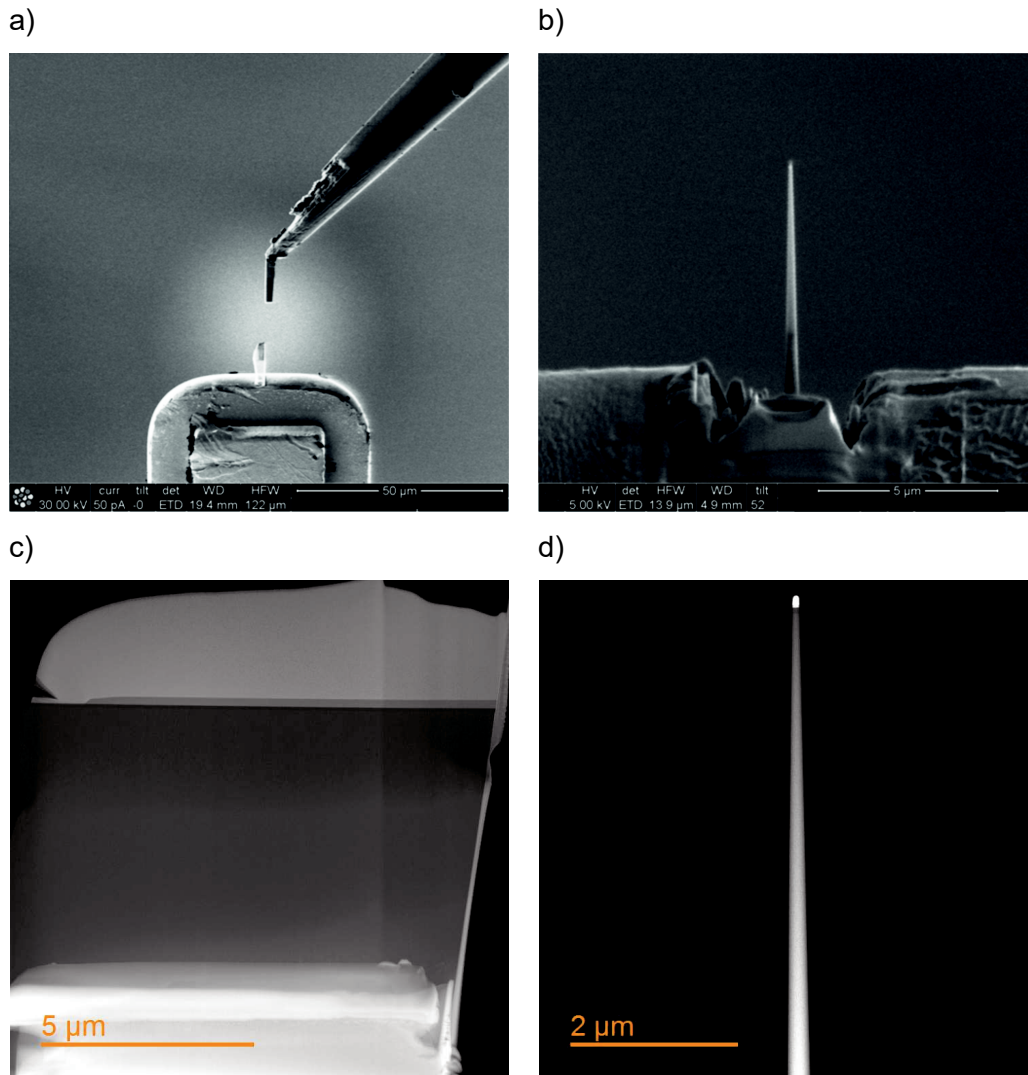
Figure 19: (a) (b) SEM images during preparation. (c) HAADF image of a silicon lamella (d) and a rod.

The sample preparation was done on a FIB instrument (Nova 200 Nanolab, FEI Company) by Sebastian Rauch. The parameters during FIB preparation were slightly adapted for each prepared material but all followed a similar workflow. The preparation was started by depositing a 5 μm thick platinum protection strip on the surface. The rod and the lamella were taken from positions next to each other to assure the same concentration and morphology. The milling was started with 30 kV and 3 nA beam current (rectangular and circular pattern). The raw rod/ lamella was transferred in-suit with an Omniprobe micromanipulator to the grid. The milling currents for the rod preparation ranged from 500 pA to finally 30 pA at 30 kV. For the lamellas an additional polishing step of 5 kV and 70 pA under an angle of 6° was used. FIB preparation can introduce several artefacts which alter the sample properties (compare chapter 3.6.1).

For the determination of the ζ-factors in the TEM FEI's "HiVis holder" (low background double tilt High-Visibility holder FP6595/20) was used. The ζ-factors presented here were all measured on a Titan^3 60-300 microscope (FEI). The microscope is equipped with the ChemiSTEM™ technology which includes four windowless silicon drift detectors (SDD), a high-brightness Schottky FEG (X-FEG) and high-speed electronics (*89*). Furthermore, the system is equipped with a monochromator (Wien filter), a probe C_S corrector (DCOR from CEOS) and a GIF Quantum (Gatan Inc).

For all EDXS measurements the specimen was always the first part mounted in the holder (afterwards the spacer ring and the clamp) and it was always put in the same direction (see Figure 20) that the lamella was on the α-tilt axes of the holder. In the microscope it was checked that the orientation of the specimen was in an off-axis condition with respect to the crystal structure to avoid channelling effects during EDXS measurements (compare (*90–92*)). For all measurements we tilted towards one side, α specimen tilt ±15°, and for Q3 and Q4 the Omniprobe grid was rotated in the grid plane by 180° (as shown in blue in Figure 20). This approach is needed due to geometrical reasons. The position dependency of the ζ-factor is discussed in chapter 0.

a)   b)
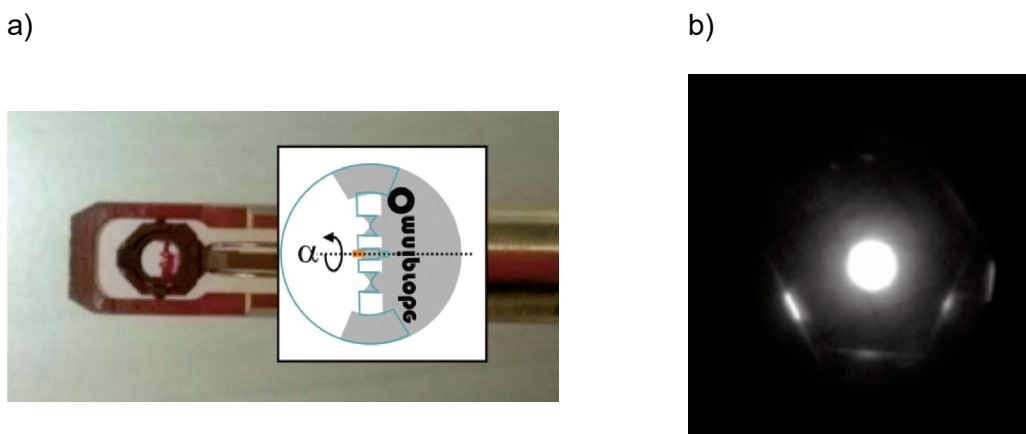
Figure 20: a) Photograph of a sample mounted in the specimen holder. Inset shows position of Omniprobe grid: normal and 180° rotated in blue. b) Convergent beam diffraction to check if sample is in a zone axis.

3.6   Interaction of electrons and ions with a sample

In this chapter a short overview on the interaction mechanisms of an ion- or electron beam hitting a sample is given. These interactions are important for the preparation of TEM samples

using a FIB instrument where a focused gallium ion beam is used to mill a sample out of a bulk specimen. The mechanisms in TEM are similar just that the beam is an electron beam and therefore the effects are different. Electron sample interactions generate signals used for imaging and analytics, but also can lead to a phenomenon generally called radiation damage.

3.6.1 Ion-specimen-interactions

Ion-specimen-interactions are important as far as sample preparation using a focused ion beam instrument is considered. The impinging particles, in our case gallium ions, transfer energy to the sample due to interaction with the electrons and/or the nuclei of the specimen atoms. Generally, the energy loss has both a nuclear and an electron contribution but in energies used in FIB preparation the effect of nuclear energy losses is dominant. At standard FIB acceleration voltages (~5-50 keV) nuclear losses due to nuclear collisions is the most likely process which can be described by an elastic two body process and lead to sputtering of the sample material. In TEM sample preparation the effect of sputtering is used. Sputtering is a statistical phenomenon and occurs if a sample surface atom receives energy higher than its surface binding energy. This energy transfer is the result of a cascade of elastic collisions initiated by the impinging ions. Sputtering depends on the relation of the initial energy and mass of the impinging ions, incident beam angle, and the specimen atoms (atomic numbers and mass). If the transferred energy is not high enough, surface and bulk dislocations and the rearrangement of specimen atoms can be the effect. If the impinging ions lose all their energy in the sample they get trapped, which is called implantation. The degree of the implantation of gallium atoms depends on the milling conditions as well as on the sample and its properties such as crystal orientation (*93–95*). The amorphization of the surface as well as the implantation of gallium ions are generally observed artefacts introduced by a FIB preparation. They can be reduced by carefully adjusting the milling parameters or by a subsequent cleaning step (e.g. NanoMill® (*96*)).

3.6.2 Electron-specimen-interactions

If the interaction of an electron beam with a specimen is considered the same categorization is made in electron-nuclei and electron-electron interaction. The electrostatic interaction of the incoming electron beam with the Coulomb field of the atomic nuclei is referred to as elastic scattering. It conserves kinetic energy and momentum. Whereas the interaction of the incoming electron beam with the electrons of the sample is referred to as inelastic scattering. It conserves the total energy and momentum by partly transferring the kinetic energy into electronic excitations. As already mentioned these effects are essential for TEM analysis

(giving signals used for imaging and analytics) but also give rise to radiation damage as described in the following sections. The following sections are based on (*31*), (*97–100*).

Knock on damage

A result of elastic interactions can be **atomic displacement**. A degradation in crystallinity due to high-angle elastic scattering can appear if the transferred energy exceeds the displacement energy. The displacement energy depends on the bond strength, crystal lattice and atomic weight of the specimen atoms. Due to the surface to volume ratio of a TEM lamella also surface effects have to be considered. The threshold for displacing a surface atom is far lower than for a bulk atom and often leads to the loss of atoms. This effect is generally called **electron-beam sputtering**. With the chosen conditions for ζ-factor determinations (300 keV acceleration voltage and specimens containing atoms with a low atomic number) generally displacement effects have to be expected. They can be minimized by keeping the electron dose (current density times the recording time) as low as possible.

Since the effect of inelastic scattering is a 'collision' between particles of similar mass (beam electrons and specimen atom electrons) considerable energy can be transferred. This energy transfer mainly ends up in a local temperature rise, **electron beam heating**. The local heat generation is balanced by the heat loss by radiation (usually has a negligible effect) and radial conduction in the sample which is directly related to the thermal conductivity of the specimen. In TEM conditions using high incident current and also for samples with a low thermal conductivity such as polymers heating effects can lead to thermal degradation or melting. At STEM conditions the local heat increase remains small and is usually insignificant, even if a material with a low thermal conductivity is investigated,

Radiolysis generally refers to inelastic scattering effects which lead to the breaking of chemical bonds under the influence of radiation (e.g. electron-electron interactions such as ionizations).

Ionization damage is the effect of inelastic scattering resulting mainly in the ionization of a specimen atom. Depending on the specimen material the resulting effect is different. In case of metals the transferred energy either may lead to a single-electron transition or the energy is shared among many electrons in the form of plasmons. Plasmon oscillations are rapidly damped resulting in one or more single-electron transitions. In metals the electron transition

are mainly conductive electron transitions which are exited above the Fermi energy in empty states creating a vacancy in the conduction band. Due to the high electron density in metals the thereby generated vacancies are filled on a time scale much shorter than the nuclei would need to react on the changed electron configuration. The de-excitation process results in phonon creations (temperature increase) but no permanent displacement of atoms.

In insulating and semiconducting specimens the mechanism of inelastic scattering are the same but the available electron density is lower and therefore the consequences are different. The excitation process mostly involves a valence electron excited into the conduction band which creates an electron-hole pair. These excited electrons represent internal secondary electrons which can again produce further electron-hole pairs within the specimen. The life time of an electron-hole pair is longer than the atomic-vibration period, because of the low electron density in the conduction band. Within this time the atom can accumulate enough energy (stimulated e.g. by atomic vibrations) resulting in a change of interatomic bonding (creation of radicals). If the energy needed for breaking a chemical bond is low, most of the transferred energy goes into the production of secondary electrons. This is particularly true for organic materials because the bond energies are rather weak (covalent and van der Waals). Therefore, it is said that especially for organic materials, the main source of damage is triggered by the secondary electrons.

Another effect attributed to secondary electron generation in insulating samples is the creation of a positive space charge. This space charge may deflect the primary beam (negligible), lead to mechanical forces and may even tear apart the specimen. The internal electric field may also produce a lateral drift of ions, dielectric breakdown or even Coulomb explosion that results in the electron beam drilling a hole in the specimen.

In Figure 21 obvious changes in the sample due to electron irradiation can be seen. On the left side a spectrum image over a very small sample area of a SiO_2 rod was acquired with a dwell time of 5 ms for EDXS acquisition. On the right side a rod made out of the NIST SRM 611, which is mainly amorphous SiO_2, is shown. The rod is severely altered by the electron beam (cut-off and bent) after a few spectrum images.
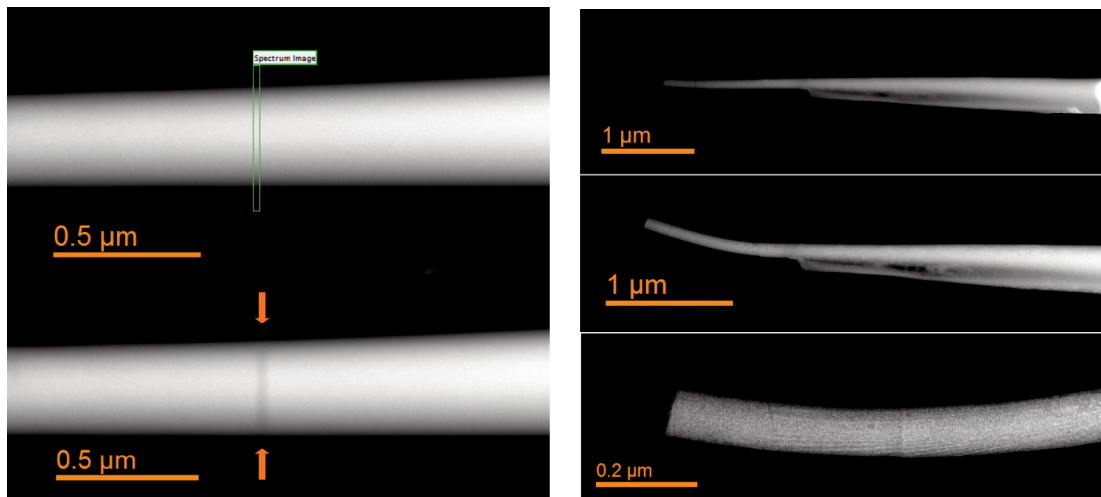
Figure 21: All images are STEM HAADF images acquired with 300 kV acceleration voltage. Left: SiO₂ rod before spectrum image (top) and after (bottom). Right: Rod of a NIST SRM 611. Sample alteration during investigation (top to bottom).

Hydrocarbon contamination occurs if mobile hydrocarbon molecules are polymerized under the electron beam. In nowadays microscopes the influence of gaseous hydrocarbons (arising from pump oils, vacuum grease…) and a bad vacuum are mostly eliminated. Nonetheless hydrocarbons attached on the TEM sample or holder still can lead to contamination. These hydrocarbons can be related to the sample preparation and the storage, as well as to the transport through normal air. Generally, there are several approaches to reduce the mobile hydrocarbons, but most of them include a procedure which can alter the sample properties such as heat or a treatment with oxygen /argon plasma. Therefore, we did not apply any of these on our ζ-factor standard materials. The specimen holder as well as all additional parts (clamp and spacer ring) were pre-cleaned in a plasma cleaner without the sample mounted.
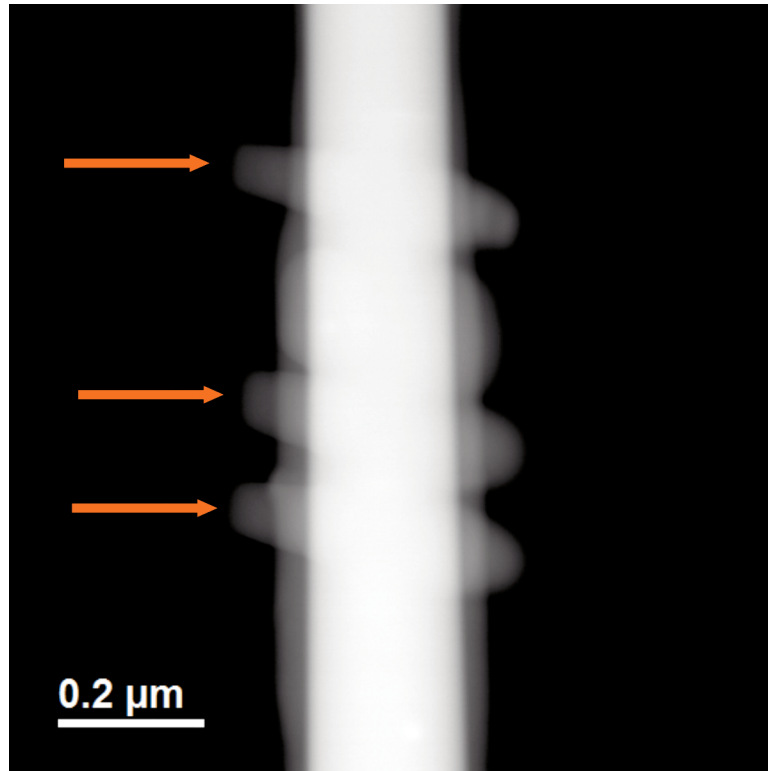
Figure 22: STEM HAADF image of a Carbon contamination on a Strontium titanate rod.

In Figure 22 a Strontium titanate rod can be seen. The light grey areas are hydrocarbon contaminations. The orange arrows mark points of previous investigations.

Monitoring the stability of sample

The stability of the standard material has to be given throughout the whole measuring process to gain reliable values. To be sure that the sample did not change during the acquisition a t/λ map was made before and after the acquisition of the EDXS spectrum over the same area. The average change in the relative mean free path stayed constant within 1% to 2%. The EDXS measurements discussed here were all done using a focus window in which the electron beam was scanned (~100 nm x ~ 100 nm) while a single EDXS spectrum was acquired due to issues with the erroneous acquisition times using DM spectrum imaging and considering sample damage. Due to the high scan speed (~20 µs/ pixel) the damage done by the electron beam should be at a minimum and the change in thickness as well as potentially hydrocarbon contamination should be spotted thereby.

3.7   Properties – mass-thickness

The thickness of a TEM sample is an essential parameter for imaging methods (beam spreading with $t^{3/2}$) (31) as well as for analytics. It is important for EELS because the increase of plural scattering leads to a loss of information due to an increased background (SBR worsens). In EDXS the absorption of characteristic X-rays within the sample increases.

In case of the ζ-factor determination the mass-thickness needs to be known (see equation (3.5)).

It is common practice to use the bulk density of the used material for the thin TEM sample. This is done for TEM specimens prepared from bulk material (75) as well as for nanoparticles (84). We only worked with TEM samples prepared from well-defined, crystalline bulk materials using a FIB instrument. The preparation will definitely affect the materials crystallinity and thereby its density on the surface of the specimen, but generally the structure remains the same as in the bulk and the assumption of similar density is valid.

The second parameter needed for the mass-thickness is the thickness of the TEM specimen. Generally, there are several methods to determine the thickness of a TEM sample which can be found in standard TEM textbooks (e.g. (31)). These methods vary in accuracy and range of application. Some provide the thickness of a sample very accurately, such as convergent beam electron diffraction (CBED) method. ($101, 102$). However, this method only works well with rather thick samples and provides only the thickness of the crystalline part of the sample. If an additional, non-crystalline layer is present, the thickness will be underestimated by the CBED method. Methods which are usually used for non-crystalline samples mainly provide the mass-thickness and not the specimen thickness. The Contamination-Spot method is one method which would measure the total specimen thickness but is not state of the art anymore because the effect of contamination is undesired and generally minimized if possible. Furthermore, it would not give the thickness with the desired accuracy. The most widely used method is the determination of the relative thickness using EELS. The big advantage of this method is that it can be used on all kinds of specimens. Given that the TEM is equipped with an electron energy loss spectrometer, the method provides readily available relative thickness information. In this work we used EELS in combination with the geometry of the sample to determine the absolute thickness needed for ζ-factor determination.

3.7.1 Relative thickness determination – t/λ

Generally, EELS can be used to determine the sample thickness because the amount of inelastically scattered electrons is a function of sample thickness. The log-ratio method is often used, which defines the thickness of a sample as follows (*50*):

$$t = \lambda \, ln\frac{I_t}{I_0} \tag{3.14}$$

t…	thickness
λ…	mean free path
I_t…	total intensity in the whole spectrum
I_0…	Zero loss peak intensity

I_t is practically measured by integrating the EELS intensities up to 50 eV. Electrons which suffered higher energy losses, do not contribute significantly to I_t. The mean free path of an electron in the specimen is the second parameter needed for calculating the thickness using (3.14). This value can be calculated using a parameterized formula by (*103*):

$$= \frac{106 \left(^0/_m \right)}{\left(^2 \; ^0/_m \right)} \tag{3.15}$$

λ…	mean free path in nm
F…	relativistic correction factor
E_m...	average energy loss in eV for a material with average atomic number Z
E_0…	primary Energy in keV
β…	collection semi angle in mrad

with:

$$_m = 7.6 \; ^{0.36} \tag{3.16}$$

$$= \frac{1 + \left(^0/_{1022} \right)}{\left(1 + \left(^0/_{511} \right) \right)^2} \tag{3.17}$$

Equation by (*103*) is based on the dipole approximation ($< \sqrt{2\Theta_E}$). It assumes TEM conditions (*α*, the convergence angle ≈ 0 and thereby much smaller than the collection angle, *β*). It is not fully valid if the collection semi angle is similar or smaller than the convergence semi angle. Furthermore, equation (3.15) assumes a refractive index of >>1 which is valid for metals but not for all semiconductors and insulators. The accuracy of the mean free path calculated following (*103*) is 10%-20%.

Another parameterized formula to calculate the mean free path is suggested by (*104*). It is parameterized in terms of specimen density ($\lambda \sim \rho^{-0.3}$) and also considering the convergence semi angle. This parametrized formula is more suited for STEM conditions.

Practical mean free path determination was done by acquiring a relative thickness map of a rod shaped sample. Assuming that the rod shaped sample is symmetric we fitted a cone to the rod and gained the actual thickness at any position. In a next step the mean free path length is calculated and the mean value over the rod was used for further measurements.

The method is explained in more detail in the following paragraph. An EEL spectrum image over the rod sample was acquired. The zero-loss peak was extracted using the reflected tail model (implemented in DM). The difference of either using the reflect tail or the fitted logarithm tail model was <2%. In a next step the mean free path was calculated following (equation (3.14)) (Figure 23a). For the perfectly round rods a DM script written by Uusimaki and Kothleitner was used (compare (*75*)). The script fits a rotary cone to the rod and calculates a thickness map (Figure 23b) and a *λ* map (Figure 23c).
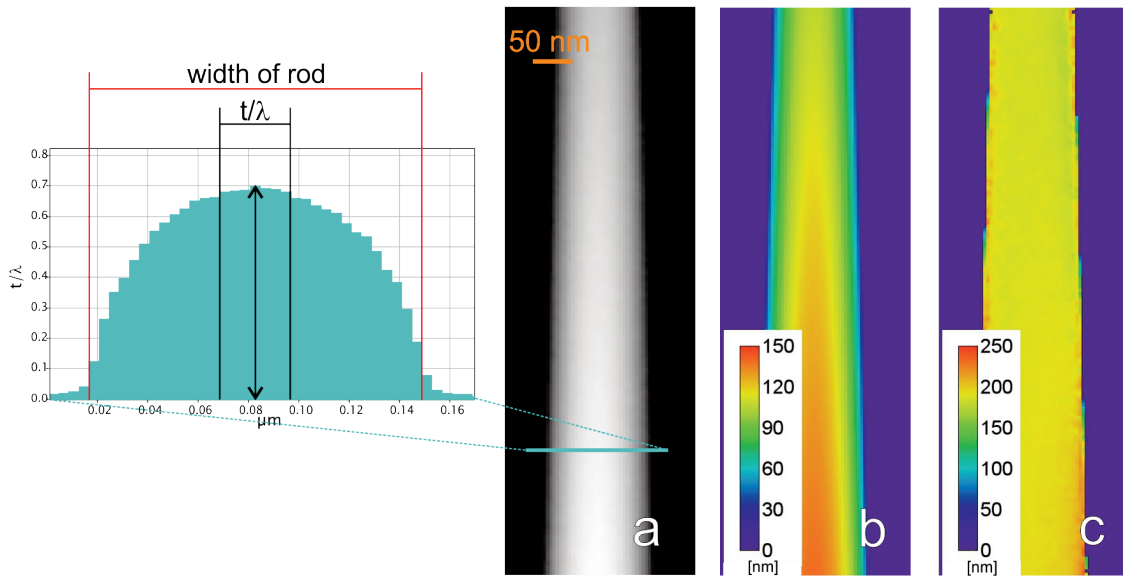
Figure 23: In a) a relative thickness map of a rod is shown. In b) the absolute thickness map is depicted and in c) a map of the mean free path. The profile extracted from a) shows a perfect rod. The area marked in red corresponds roughly to the width of the rod and the area indicated in black corresponds to the area used to determine the maximum relative mean free path.

The samples, which were obviously not perfectly symmetric over the whole length of the rod, were not evaluated with the DM script because the assumption of a perfect cone would have led to wrong values for λ. This was the case for the Al_2O_3 and the SiO_2 rod. These two samples were evaluated by extracting a line profile over symmetric parts of the rod (checked via a profile of the relative thickness map as shown in Figure 23), measuring the absolute thickness at that position and the maximum relative mean free path. This was done over several positions along the rod. The chosen step width during the spectrum image acquisition determines how precise the thickness of the rod can be measured. As can be seen in the profile shown in Figure 23 one is limited by the step width of the spectrum image. Due to the choice of the area of the rod an error of approximately 10% has to be assumed.

In case of aluminum and silicon no obvious deviation of a perfect symmetric rod were observed. The thickness map and the map containing the relative mean free path were used to create a bivariate histogram as shown in Figure 24 (second row, left side). The bivariate histograms all showed a nice linear behaviour over a large range. Plotting the relative thickness versus the absolute thickness in a bivariate histogram give rise to the relative mean free path length being the slope of this linear relation. The example shown in Figure 24 is an exceptional case. Here the tip of the silicon sample is shown. The silicon sample was cut out of a silicon bulk substrate with a silicon oxide on top. Therefore, the top of the rod contains also a thin

silicon oxide layer and finally the platinum layer deposited during the FIB preparation. These phases can also be seen in the bivariate histogram. The silicon phase is the most pronounced feature (#1 in Figure 24). The mean free path was calculated by fitting the slope in the bivariate histogram in the linear regime (corresponding to phase #1). The other phases in the bivariate histogram can also be nicely assigned to the other materials. Silicon oxide has a steeper slope than pure silicon and therefore a higher λ. The platinum phase has a smaller slope and therefore a lower λ. It also can be seen that at lower absolute thicknesses the silicon phase broadens. This is due to the increased influence of the surface layer to the total thickness of the rod and probably also edge artefacts play a role. This area was neglected during the λ determination of the pure materials.
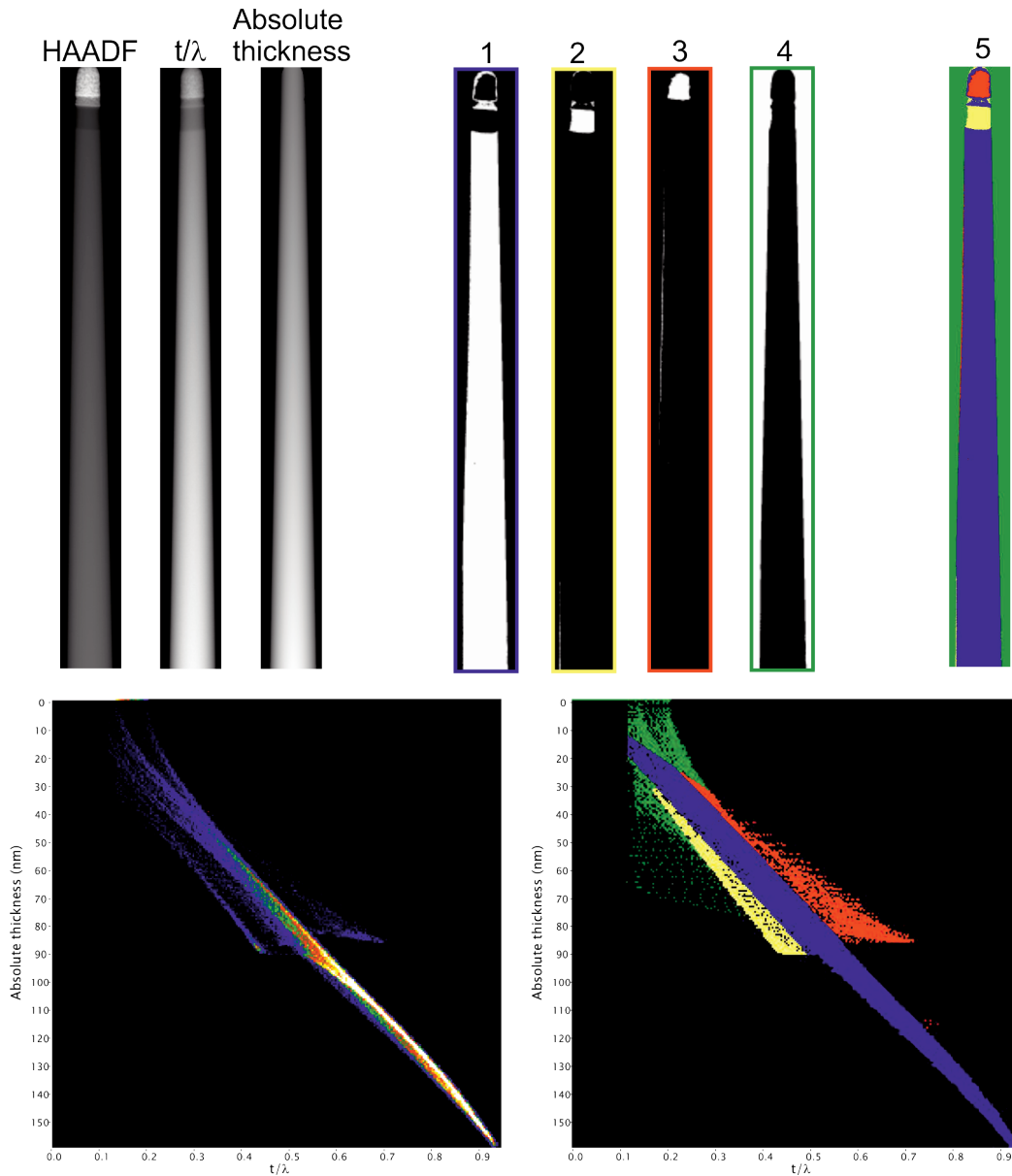
Figure 24: First row: From left to right: HAADF image of a silicon rod. On the tip of the rod are a SiO₂ and a platinum layer; corresponding relative thickness map (t/ λ) and the absolute thickness map; extracted phases 1-4 and overlay images of the phases. The image width is always 206 nm. Second row: A bivariate histogram of the relative thickness map and the absolute thickness map is shown. The coloured area correspond to the extracted phases above.

To make the influence of a surface layer even more clear a multi linear least square fit of an EEL spectrum was performed. Therefore, spectra of silicon oxide and pure silicon were extracted (both over the range of 60 eV – 300 eV) and fitted to the top of the silicon rod. In Figure 25 a colour map of the fit coefficients of the multi linear least square fits are shown and a silicon oxide layer on top of the silicon of around 6.5 nm can be identified.
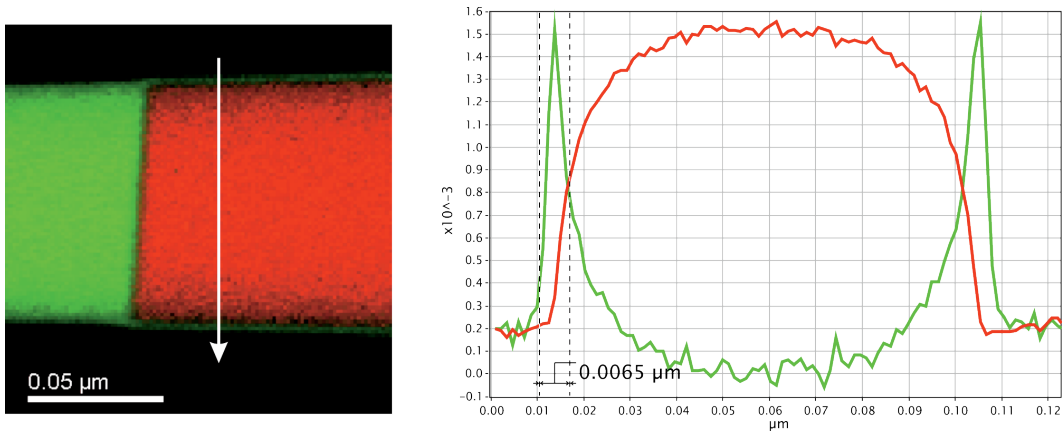
Figure 25: Multi linear least square fit of the EEL spectrum of silicon oxide (green) and silicon to the top of the silicon rod.

In Table 2 the determined values for the mean free paths are listed. Moreover, calculated values following (*103*) and (*104*) are also shown. The calculated values following (*104*) generally show a better agreement to the measured values except for Al_2O_3. The values were calculated using the MFP Estimator by D. Mitchell (*105*) available for DM.

Table 2: Determined mean free path for Si, SiO$_2$, Al and Al$_2$O$_3$ as well as calculated values following (*103*) and (*104*). All values were determined for an acceleration voltage of 300 keV. TEM corresponds to very a small convergence angle.

	β (mrad)	α (mrad)	λ (nm)	
Si	41.1	20	187	This work
	41.1	20	182	Iakoubovskii
	41.1	TEM	116	Malis
SiO$_2$	41.1	20	181	This work
	41.1	20	176	Iakoubovskii
	41.1	TEM	129	Malis
Al	41.1	20	152	This work
	41.1	20	176	Iakoubovskii
	41.1	TEM	119	Malis
Al$_2$O$_3$	41.1	20	130	This work
	41.1	20	159	Iakoubovskii
	41.1	TEM	129	Malis

The mean free path is also a function of the collection angle (*106*). Comparing the practically determined mean free path length with other literature values such as ((*75*), (*106–108*)) one can see a strong variation with used conditions (~20%, same acceleration voltage but different α and β). Therefore, the measuring conditions were always kept the same, during the measurement of the rod and the lamella. The collection angle was chosen to be 41.1 mrad and the convergence angle 20 mrad. Using these conditions the convergence angle should have no effect on the mean free path ($\alpha<\beta$) and the influence of β saturates with $\beta>20$ mrad (*106*), (*109*). These conditions are also important to avoid any influences arising from strong diffraction conditions. To avoid any influences of the sample orientation it was always checked that the sample was oriented not along a zone axis. If that was the case it was tilted to avoid strong diffraction conditions.

Finally, it can be noted that the mean free path for aluminum and silicon were reliably determined. The influence of a surface layer is not considered and might have an influence if

thinner regions are chosen for the ζ-factor determination. In case of the investigated oxides the mean free path determination is not so reliable due to the imperfect shape of the rods. Generally, if the mean free path is wrong for a particular material it will only apply a constant factor to the determined ζ-factors. This could explain a different ζ-factor determined for Al from the pure aluminum sample or the Al_2O_3 sample.

3.8   Instrumentation and online system

3.8.1   Current measurement

The probe current and the live time have a direct influence on the electron dose which is inversely proportional to the ζ-factor. The probe current was measured with the spectrometer drift tube. This was done before and after each EDXS measurement by moving the specimen out of the electron beam and acquiring 10 measurements with the drift tube. In addition the calibrated fluorescence screen was used to monitor the stability of the current. The current gained by the calibrated fluorescence screen is overall ~20% higher than the current measured with the drift tube. The mean value of 10 measurements before and after the EDXS acquisition was used for ζ-factor determination. The beam currents ranged from 0.27 nA -0.32 nA for all measurements. Generally, the beam current was very stable (relative variation was below 2%).

3.8.2   Time measurement - detectors

Three time periods are important for EDXS measurements; the real time, the live time and the dead time. The real time is also called the clock time. The live time is the time period the EDXS detector is actually measuring X-ray counts and is not busy processing and analysing the counts. The dead time is the time where the detector is busy processing counts and the generated X-rays are not detected. With nowadays electronics and SDD technology high count rates are usually no longer a problem. In all EDXS measurements the dead time was <5%. The live time was used to calculate the ζ-factors.

Individual EDX spectra were acquired by scanning over a sample region (The acquisition of spectrum images would have been preferred but was not possible as the used version of DM provided wrong values for the acquisition times).

Another problem considering the live time also interfered with our measurements. The detectors (Q2-Q4) tend to stop counting if the count rate drops below a threshold value. This value is different for each detector and highest for detector 3. It obviously influences the

measurements in two ways: if the count rate is too low the detector does not count at all (therefore e.g. no measurements for SiO_2 for Q3 exist) and on the other hand it sometimes takes the detector a few seconds before it starts counting. This time period only can be guessed and probably ranges up to 5 s. This effect did get better recently due to the newly configuration of the detectors by Bruker but could neither be completely solved nor be sufficiently explained yet and was present during all the measurements presented here.

3.9 Intensity determination

A reliable characteristic X-ray intensity determination includes the removal of the bremsstrahlung background and the extraction of characteristic X-rays intensities.

As already mentioned before (chapter 3.1.1) the background arises due to the interaction of beam electrons with the coulomb field of the nuclei of the sample. A theoretic background would have a continuous decrease until it reaches zero at the beam energy. Practically, the bremsstrahlung background may get absorbed in the sample and in the detector barrier layers (e.g. window, contact layer, dead layer).

In the following chapters three different approaches for background subtraction and subsequent intensity determination are described: the window method, Kramers and the top-hat approach. The window method is the most basic method and is based neither on a model nor on mathematic routines. In most EDXS software a routine for background removal and intensity determination either based on the Kramers model or on a top-hat approach can be found. The following discussion on the Kramers and top-hat approach are mainly based on the usage of DM. Due to the reason that the acquisition is done in Digital Micrograph it would be practical also to use it for the intensity determination.

3.9.1 Window method

The window method is the most basic method presented here. Three windows are defined in the EDX spectrum: two background windows and a signal window. The background windows need to have the same width as the signal window and should be equally positioned on either side of the signal window. The average of the two background windows is subtracted from the signal window. If this approach is used in this work it is done via a command-line based software called 'gawk' using the free software implementation GNU awk (*110*). The program galled 'gawk' sums up the counts over user-defined energy ranges. The recommended window width is 1.2 x FWHM (full width at half maximum) because FWHM would neglect a substantial

amount of counts whereas FWTM (full width at tenth of maximum) would include more bremsstrahlung (*31*).

This method fails if the background has a high curvature because the linear approximation is not valid anymore e.g. in the low energy regime. Moreover, if overlapping lines are considered the window method cannot be used. Nevertheless, it presents the simplest method and it does neither depend on user defined properties nor on the ability of the software to fit the spectrum.

3.9.2   Background subtraction by Kramers' model

Most programs used for EDXS in TEM have implemented a background removal approach following the work of Kramers' (*56*) modelling the bremsstrahlung (compare equation (3.2)). To achieve a satisfying background removal with Kramers the absorption of X-rays in the low energy regime has to be considered within the used software (e.g. Esprit). The Kramers' as implemented in DM does not account for the absorption of X-rays in the specimen. In Figure 26a it can be seen that in the range of 0.2 keV the background model (red) is too high, whereas after the aluminum line it is too low. It is not possible to achieve a more accurate bremsstrahlung fit in DM (2.31). The signal fit (shown in green) does also not match the real spectrum (blue) which is mainly due to the reason that the characteristic peak does not have a Gaussian shape (Figure 26b). The peak shape is a result of the detector condition for which DM cannot account for.

The advantage of this correction mode within DM is that the user can easily see how well the fit corresponds to the measured spectrum. Satisfying results can be achieved if a background removal in the low energy area is not needed and all peaks have Gaussian shape.
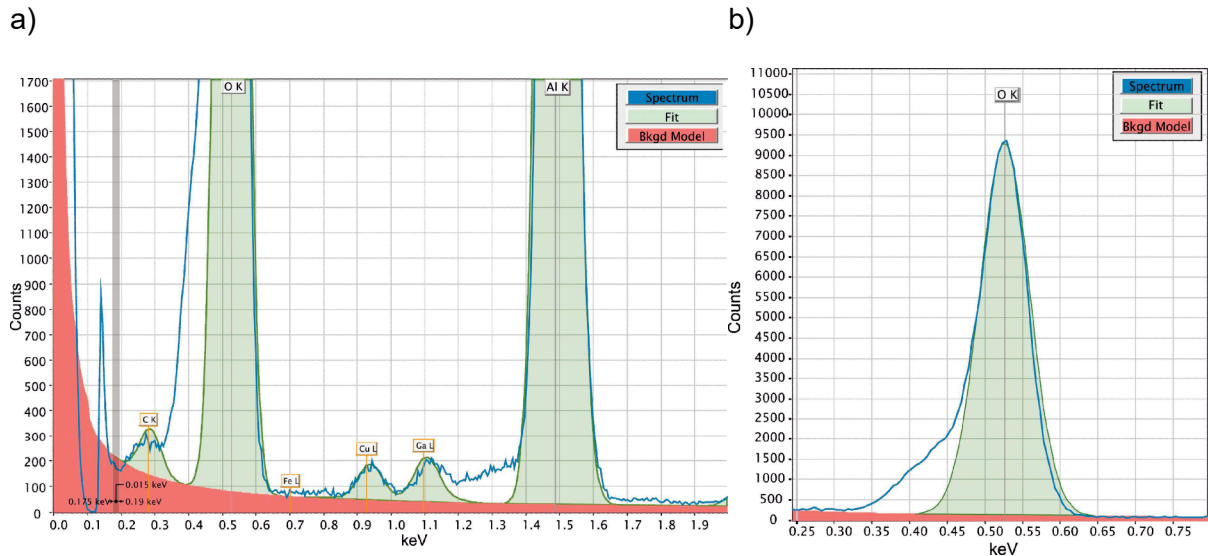
a)

b)

Figure 26: Background and Signal fit with the correction mode Kramers. The original spectrum is shown in blue, the background fit in red and the fitted signal in green. In (a) the energy range from 0 keV – 2 keV is shown and in (b) only the energy range at the oxygen signal.

3.9.3 Top-hat filter background subtraction

The top-hat approach is a purely mathematical one without any physical basis. The bremsstrahlung is removed by digital filtering. It relies on the effect that the change of intensity as a function of energy is far more pronounced in case of a characteristic line than for the bremsstrahlung. Hence *dI/dE* is larger for characteristic lines than for the background. The spectrum intensity is filtered by convoluting the spectrum with a 'top-hat' filter function; this corresponds to the second derivative of the spectrum. Thereby a constant offset and a steady slope are removed from the spectrum. Presumably DM fits the second derivative of Gaussian peaks to the filtered spectrum and uses the fitting parameters to calculate the area of the Gaussians (see Figure 27). The disadvantage of the method using DM is that the residual signal is not visible for the user and therefore it is hard to judge how well the fit corresponds to the spectrum. In other programs there is a residual spectrum shown which allows the user to estimate how good the background and the fitted spectrum match the measured spectrum (e.g. TIA by FEI). The top-hat approach is often used for multi-element samples and in energy regions below ~1.5 keV where the modelling of the background becomes more challenging. The influence of the user on the gained characteristic intensity is at a minimum using this method.
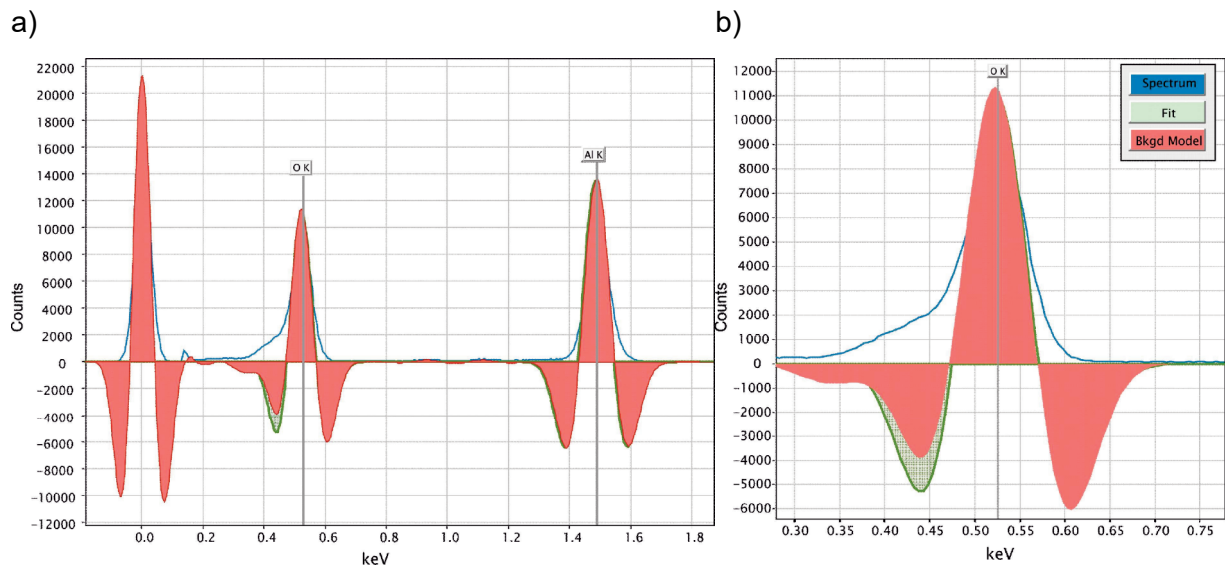
a)

b)

Figure 27: Correction mode top-hat. The original spectrum is shown in blue, the background fit in red and the fitted signal in green.

3.9.4   The programs

In this chapter the influence of the chosen program and its settings for EDXS evaluation is emphasized. A spectrum of Al_2O_3 (Figure 28a) and a spectrum of an AuPd film on a silicon nitride membrane (Figure 28b) (both measured with Q1) were evaluated with TIA (TEM imaging & analysis offline by FEI, 4.6), Esprit (Quantax 400 by Bruker, 2.0.0.2108) and DM (Digital Micrograph by Gatan, 2.31.734.0). The adjustment of the settings for the microscope and the EDX spectrometer (e.g. window type, dead layer…) are mandatory to achieve realistic results.
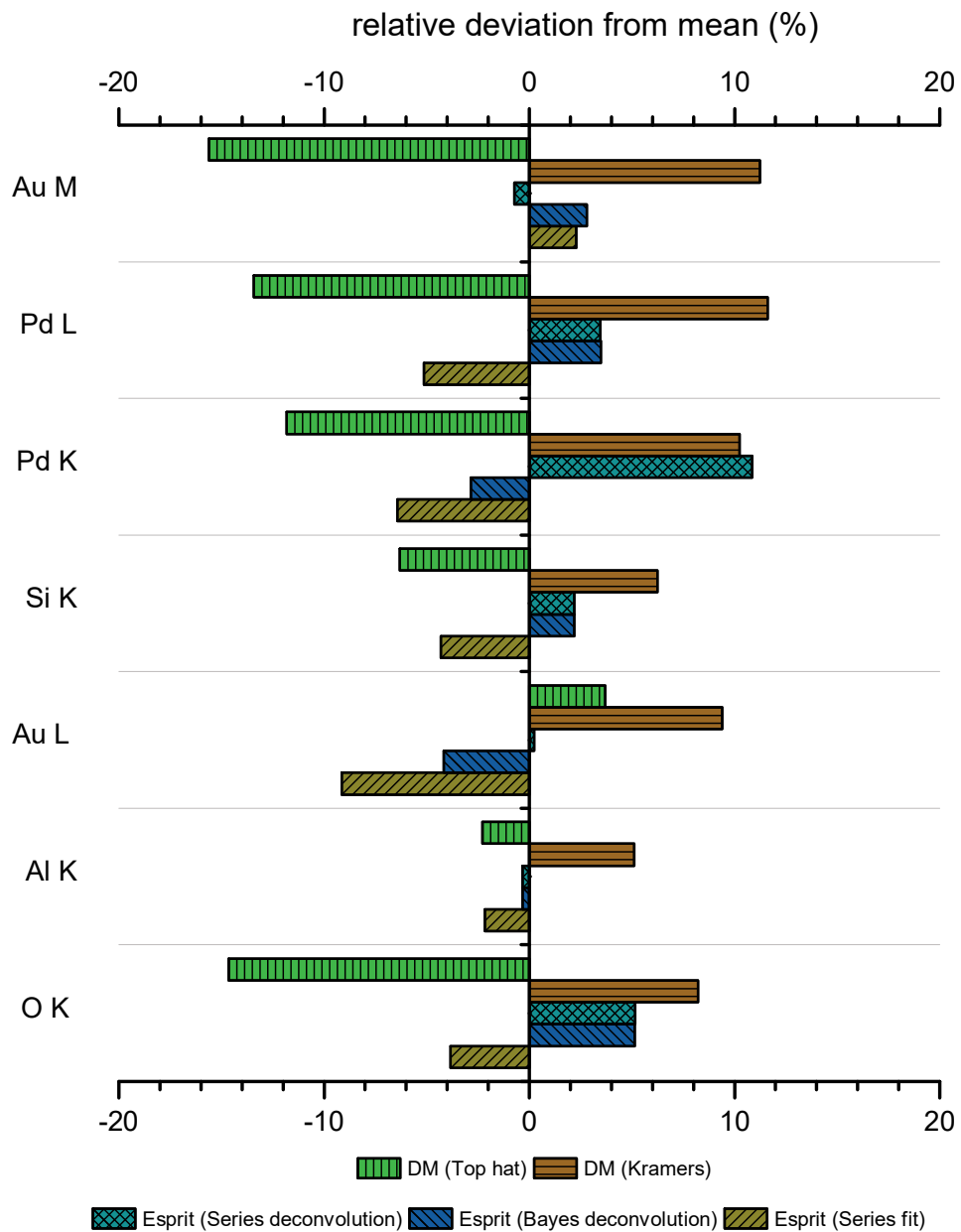
Figure 28: Relative deviations of characteristic line intensity determination with different EDXS programs and setting.

Table 3: X-ray intensities for several X-ray lines determined with TIA, Esprit and DM with different methods.

	TIA		Esprit			DM	
	Modeled	Top-hat	Series fit	Bayes deconv.	Series deconv.	Kramers	Top-hat
O K	113045	146622	136887	149693	149706	154071	121495
Al K	177654	190160	181938	185373	185373	195474	181722
Au L α	10051	11422	10499	11069	11583		
Au L			17543	18503	19355	21125	20025
Si K	17995	22899	19635	20968	20968	21801	19221
Pd K α	576	417	691	742	818		
Pd K			806	837	955	950	760
Pd L α	3693	5885	5493	5583	5991		
Pd L			8186	8929	8928	9630	7471
Au M α	14410	17242	14888	13785	14450		
Au M			23714	23834	23016	25791	19563

In Esprit only 3 approaches are chosen: Series deconvolution, Bayes deconvolution and Series fit. It is not entirely clear what the different routines do within Esprit. According to the user manual Series Fit is a robust approach strongly recommended for overlapping lines but the system needs to be well calibrated. Series deconvolution is less sensitive on slightly varying parameters (e.g. energy calibration) and optimizes the line intensities separately. It separates the partially overlapping peaks on the basis of probability calculations. In Figure 28 the relative deviations from the average of characteristic line intensities of the samples are shown. It compares the results gained from the different programs with varying settings for the background removal and the intensity determination. Figure 28 shows that the choice of the program as well as the choice of the method has a significant influence on the results. The results not only depend on the program and method but also on the element analysed. In case of e.g. the Al K line the relative deviation is, for all settings below 5% (average relative deviation of 2%). Whereas in the same spectrum the relative deviation of oxygen rises up to ~15% (average relative deviation of 7%). TIA was also used for the intensity determination but in Figure 28 only the other programs are shown. This is due to the fact that TIA seems to determine the intensities of only the α-lines of the corresponding family. In case of L and M and also some K families the β line has a significant contribution (like e.g. Au L) (compare Table 3). It has to be pointed out that it is not always obvious which lines are included to the gained characteristic line intensities. If absolute sensitivity values like ζ-factors are used one has to keep in mind which lines contributed to the characteristic intensity. It also has to be stated here that in the following chapter DM does not consider the whole family but only the

α-lines. The spectrum evaluation was done with the same DM version but an update of the Analytical Plugins has changed the quantification routine.

As a result of this experiment one can conclude that the choice of the program as well as of the settings has severe influence on the determined intensities (up to ±16%). It has to be recommended to always use the same program and same settings if one wants to compare results of different measurements. Special care has to be taken if one software or version uses only the α-lines and the other the whole family.

In case of sensitivity factors differences in intensities are cancelling out as long as ratios are considered. If absolute intensities are used one has to keep in mind that the values are strongly dependent on the chosen program and settings.

3.9.5   The user

In a next step it was tried to evaluate the influence the user has on the intensity determination. Therefore, six persons evaluated two spectra. In order to be independent of spectrum artefacts (like ICC,…) (see chapter 3.9.6), simulated spectra are used. Therefore, three different spectra were simulated with DTSA II (Halley 2014-08-01 revision). A spectrum of a pure Si sample, an Al_2O_3 sample and a TiO_2 sample are chosen and simulated with the following parameters:

Quantification algorithms:

        Correction Algorithm: XPP Pouchou & Pichoir Simplified

        Mass Absorption Coefficient: NIST-Chantler 2005

        Bremsstrahlung angular distribution: Isotropic

        Ionization cross section: Bote/Salvat – 2008

Instrument and detector:

        SDD detector with no window

            Geometry:

                Elevation angle: 18°

                Azimuthal angle: 45°

                Optimal working distance: 10 mm

                Sample-to-detector distance: 14 mm

             Crystal parameters:

                Detector Area: 120 mm²

                Gold layer: 0.01 nm

                Dead layer: 0.005 μm

                Thickness: 0.45 mm

Base Performance:

        Energy scale: 5 eV/channel

        Zero offset: 0 eV

        Resolution: 133 eV FWHM at Mn Kα

Simulation Mode:

        Monte Carlo model of a block:

Substrate material: None

Block material:

	Density (g/cm³)	Atomic Fraction
Si	*2.33*	*Si* *100*
Al₂O₃	*3.98*	*Al/O* *40/60*
TiO₂	*4.27*	*Ti/O* *66.66/33.34*

Block base: 2 μm

Block height: 0.1 μm

Sample rotation: 0°

Beam Energy: 300 keV

Probe Dose (current*time): 30 nAs

Incident Angle: 0°

Noise parameters: Apply simulation count statistics

X-ray generation modes: *Characteristics +fluorescence*

                              Bremsstrahlung +fluorescence

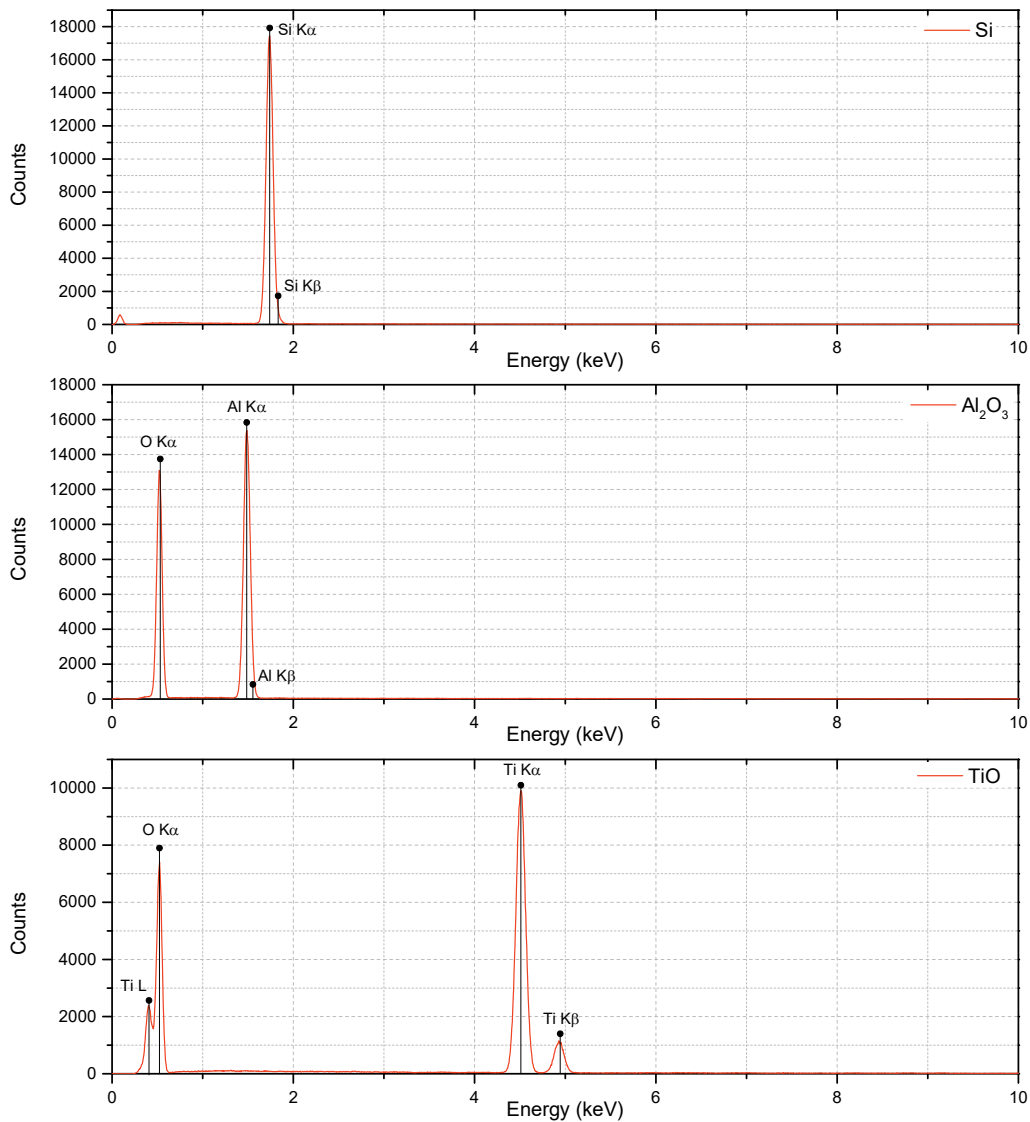Using the parameters listed above the three spectrums shown in Figure 29 were simulated.

Figure 29: Simulated spectra using the parameters listed above. From top to bottom: a pure silicon, an Al₂O₃ and a TiO₂ sample were simulated.

The intensity determination was done using five different approaches. The first two were performed in DM (2.31.734.0) using either the Kramers model or the top-hat background correction mode. All parameters were optimized at discretion of the user (Background windows, peak fitting settings, …). Esprit 2.0 (by Bruker) and a batch script following the window method (chapter 3.9.1) and written by Masashi Watanabe were also used. For the comparability of the window method with the other approaches a correction of the recommended window width (1.2 x FWHM which corresponds to 85% of the area of the whole

peak) had to be done. In the following figures the corrected intensities are called 'Gawk 100'. If the positioning of background windows using the window method was not possible as recommended in chapter 3.9.1, the user could choose a smaller background window and subtract weighted background windows from the intensity window. The category called "Fit" in the following figures represents a personal approach to achieve the best possible fitting result. Mainly Gaussian peaks were fitted after a background subtraction (mostly via a linear fit) or simply channel widths were summed up for signal and background determination.

The following figures depict the results of the experiment. The relative deviation of the EDX signal from the average value of the five different methods is plotted as a percentage. The relative deviation of each person of that value is plotted with Poissonian error bars arising from the signal intensity. Furthermore, the grey bars represent the mean value of each method to see more clearly the differences arising by the chosen approach.
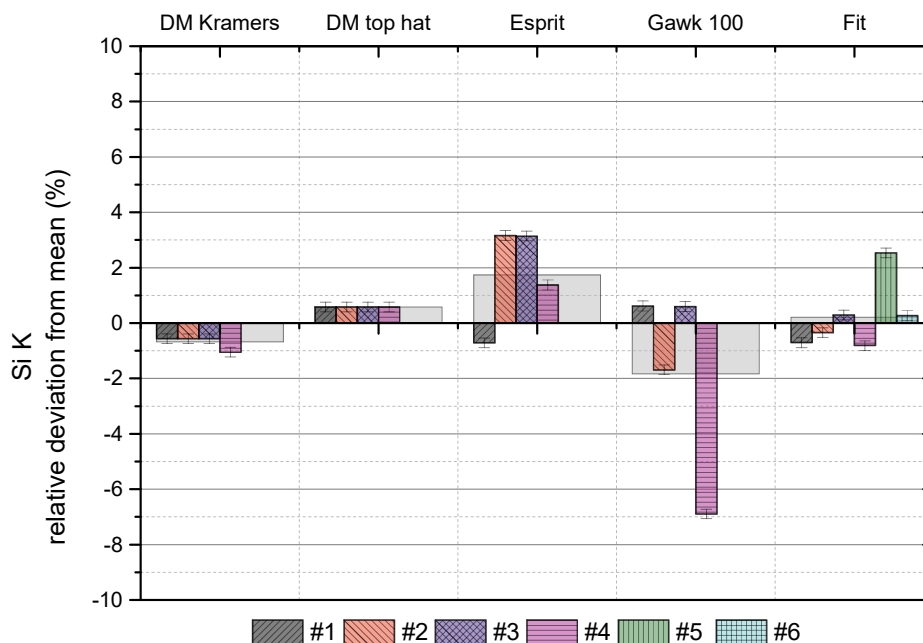

Figure 30: Relative deviation from mean Si K intensity evaluated by six different users (#1 to #6) with five approaches: DM Kramers, DM Top-hat, Esprit, Gawk 100 and Fit.

The Si sample represented the most straightforward spectrum, containing only one peak. Using Digital Micrographs Kramers or top-hat background approach the deviation of the "true"

value is rather small. Also the influence of the user is rather small, especially in case of the top-hat method. In case of Esprit higher variations are observed. This might be because not all users checked the calibration of the spectrum, which influences the intensity measurement (energy resolution, Fano factor). The deviations seen in the gawk method (and partly also in the "Fit" method) is a result from the fact that users are limited to the channel width. Slight subjective differences, including or excluding a channel, can already have an influence on the outcome. If manual fitting is used it is recommended to use a method which excludes the channel width influence e.g. fitting a Gaussian function to the peak and calculating the area underneath rather than summing intensities directly in a spectrum.

The next spectrum discussed is an Al_2O_3 spectrum. In the low energy region, e.g. O K @ 0.523 keV, background fitting is more difficult than in higher energy regions due to the more complex Bremsstrahlung. This mainly explains the deviations between the programs. Especially DM Kramers does not work well in the low energy region which is reflected in the results (still the influence of the user remains small). The "Fit" category reflects again the problem with the discrete channels.
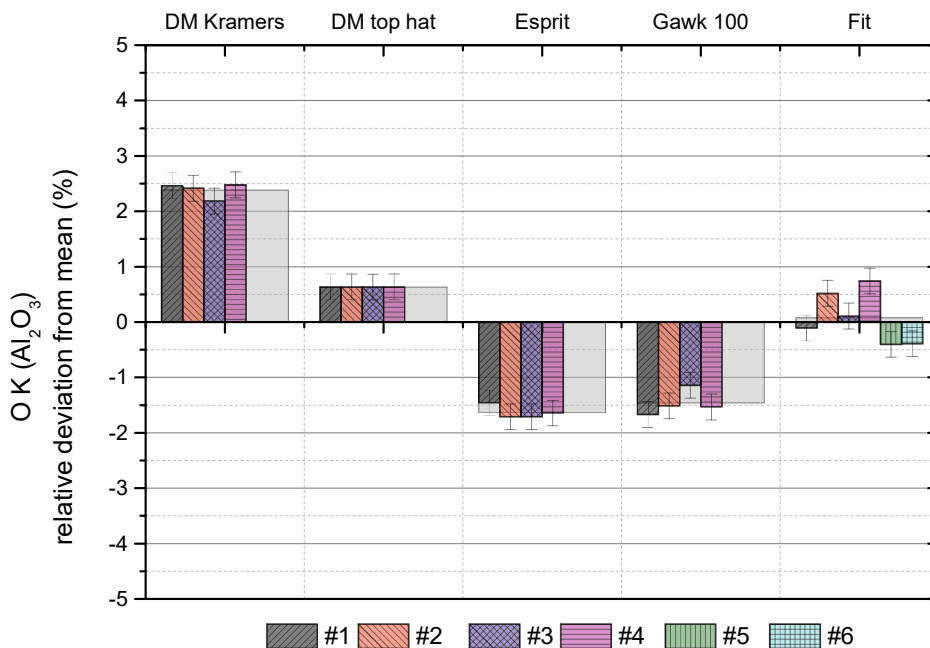

Figure 31: Relative deviation from mean O K intensity (of the Al_2O_3 sample) evaluated by six different users with five approaches: DM Kramers, DM top-hat, Esprit, Gawk 100 and Fit.
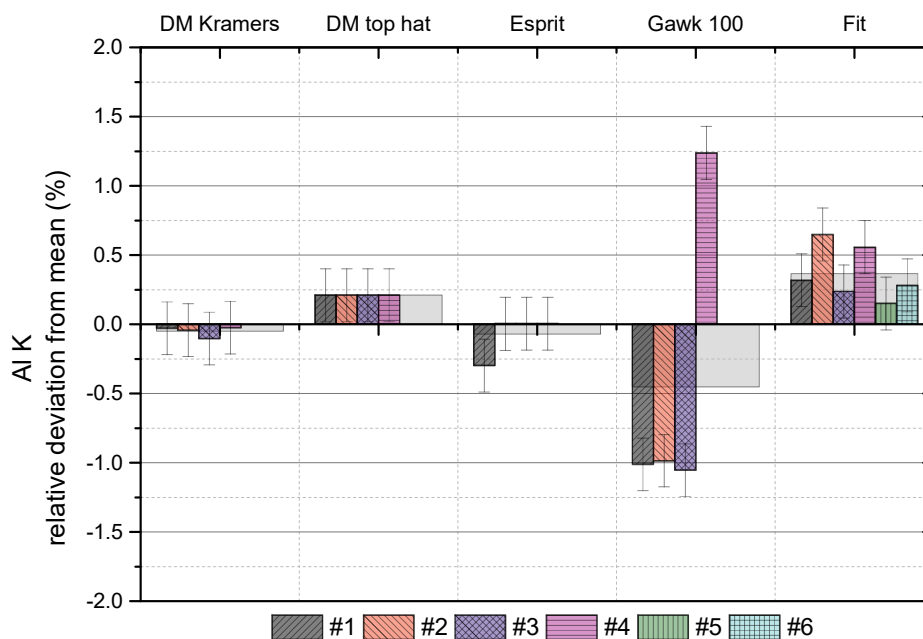
Figure 32: Relative deviation from mean Al K intensity (of the Al$_2$O$_3$ sample) evaluated by six different users with five approaches: DM Kramers, DM top-hat, Esprit, Gawk 100 and Fit

The evaluated X-ray intensities for Al show the lowest deviation between all the programs (<1.5%). The Al peak is an isolated peak in a higher energy region where background subtraction is straight forward.
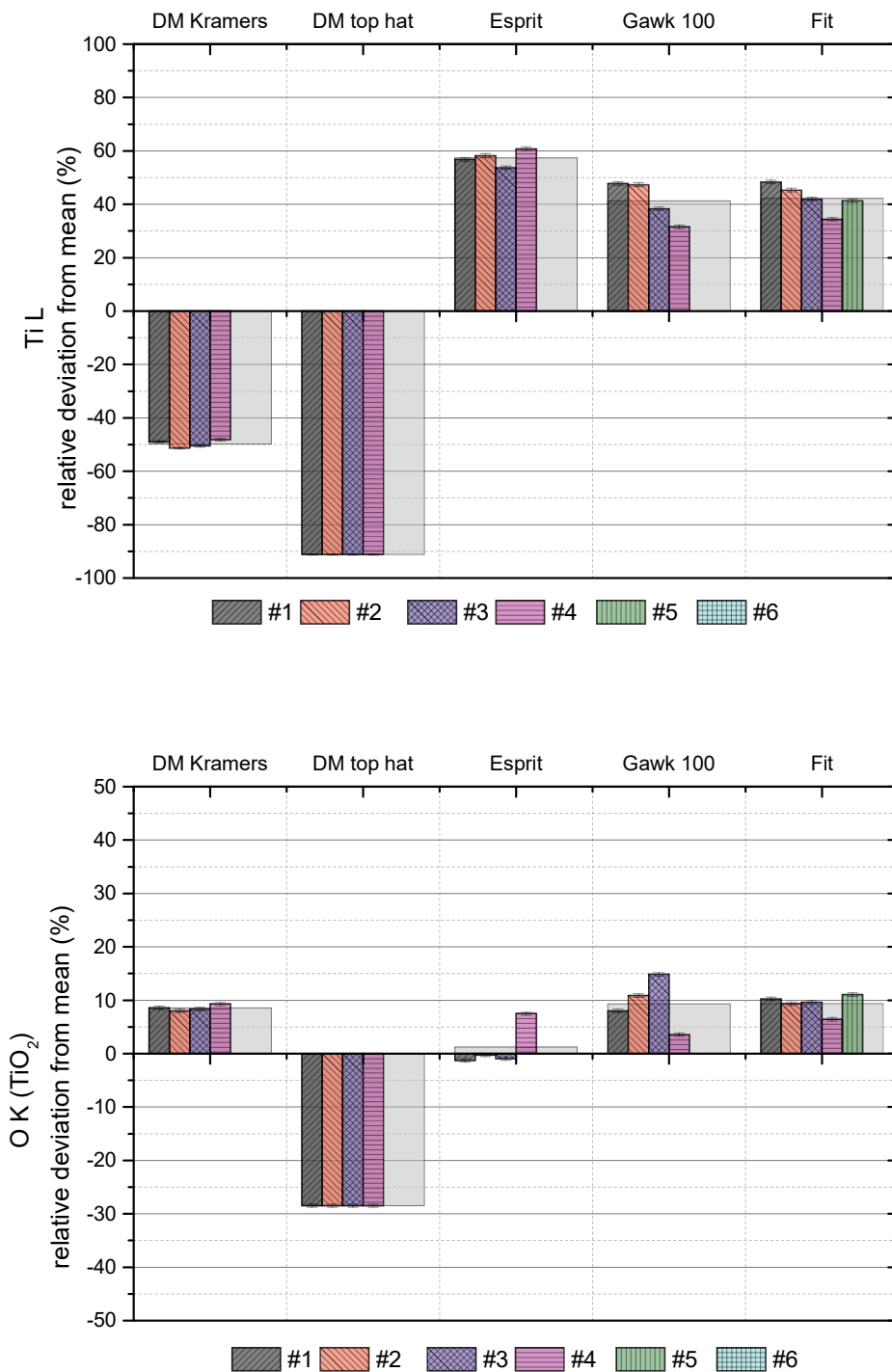
Figure 33: Relative deviation from mean intensity of a TiO₂ sample for Ti L (top) and O K (bottom) evaluated by six different users with five approaches: DM Kramers, DM top-hat, Esprit, Gawk 100 and Fit

The TiO₂ spectrum represented the greatest challenge, containing two overlapping peaks in the low energy region (Ti L and O K). The results show again that DM has big difficulties in this

energy regime as far as the agreement with the other methods is concerned. Only the Kramers model for the O K intensities leads to somewhat reliable results. In case of Ti L the intensities DM is measuring are more than 80% off from all other methods. In case of O K the top-hat method implemented in DM has the biggest deviation (~30%) compared to the other methods; whereas, in both cases, the influence of the user remains the smallest using DM.
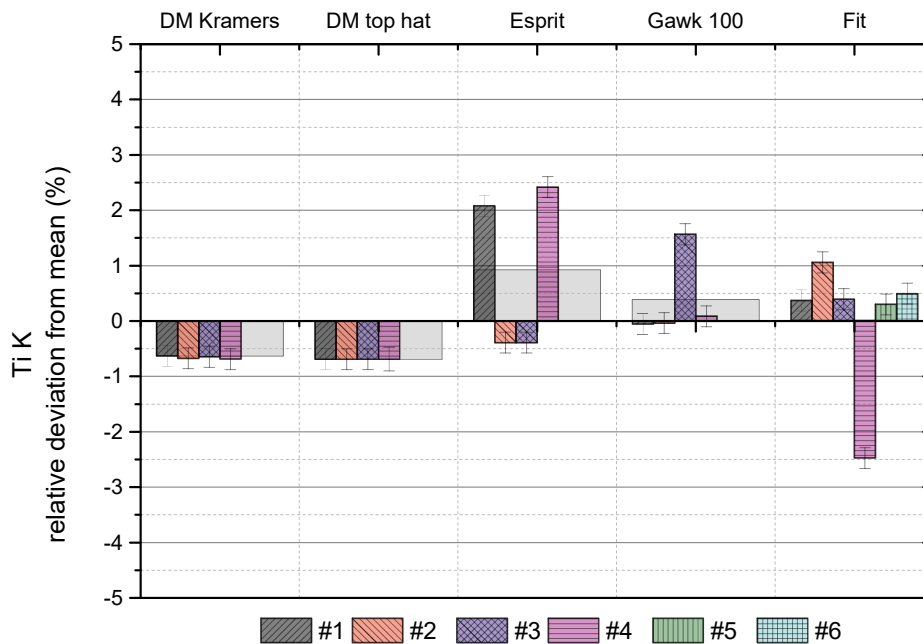

Figure 34: Relative deviation from mean intensity of a Ti K (of TiO$_2$ sample) evaluated by six different users with five approaches: DM Kramers, DM top-hat, Esprit, Gawk 100 and Fit

The Ti K family has two well separated peaks, Ti K$_\alpha$ and Ti K$_\beta$ at 4.51 keV and 4.93 keV. In Figure 34 one can see a big variation of the values determined by Esprit. On the one hand it turned out that two users used the option "fast quantification" (lower values) and two users did not. On the other hand one can notice a big difference between the values obtained with DM and Esprit. This might be explained by the fact that DM in this case (DM 2.31.734.0 with an older version of the Analytical Plugins) is only measuring the Ti K$_\alpha$ intensity, whereas Esprit gives the intensity for the whole K family. The intensity of the K family was calculated with a theoretical relation taken from Bote et. Salvat (72). Esprit has implemented different Ti K$_\alpha$/ Ti K$_\beta$ relative weights which lead to higher family intensities (see Table 4). If the absolute intensities were calculated with the ratios Esprit is using ("fast quantification" activated =

0.1377) the relative deviations would be lower (see Figure 35). Generally, the determined Ti K X-ray intensities show very small relative deviations (<4%).

Table 4: Relative weights of X-ray lines

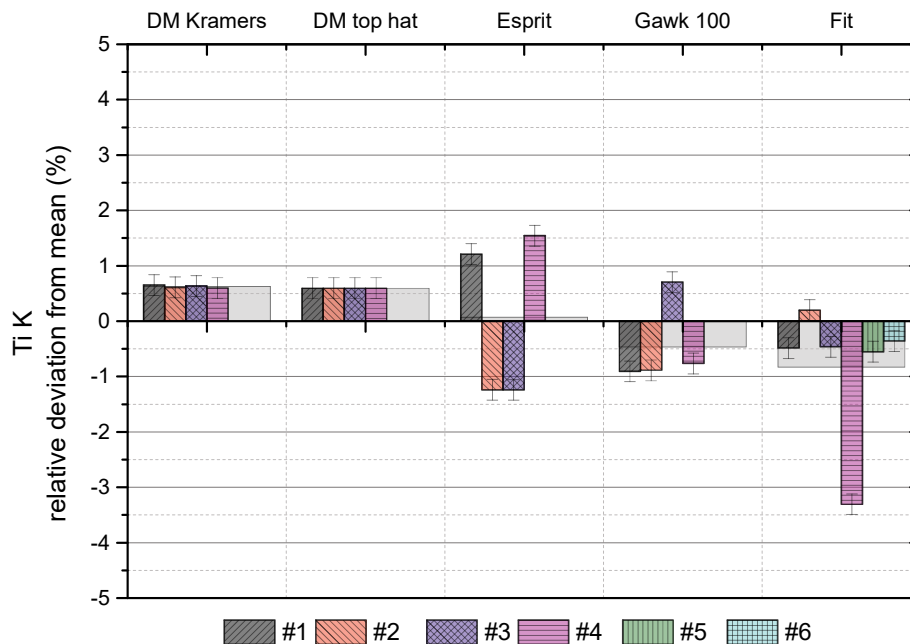|	K_β/K_α
Bote et. Salvat	0.1136
Esprit (fast quantification)	0.1377
Esprit	0.1963

Figure 35: Relative deviation from mean intensity of a Ti K (of TiO₂ sample) evaluated by six different users with five approaches: DM Kramers, DM top-hat, Esprit, Gawk 100 and Fit. The absolute intensities are calculated with a relative weight of 0.1377.

This experiment indicates that if the influence of the person determining the intensities is kept to a minimum, all receive similar results. This is the case if DM is used, especially using the top-hat method. Moreover, the experience of a user with a program also affects the reproducibility. In case of DM all users are similarly experienced the agreement of the determined intensities is good. Vice versa, in Esprit not all users share the same level of

experience and the deviations are higher. The large deviations for the fit and gawk approach are arising from the fact that if intensities are measured directly in the spectrum small differences of the width of the summed region can have a big effect due to the energy/ channel limitation. So it is recommended to use a method which is not dependent on the channel width.

Finally, no general method for intensity determination can be recommended. Top-hat filtering offers fairly reproducible values but in lower energy regions and with overlapping peaks it not always provides correct values. Moreover, it is not possible for the user to check how good the background removal and the peak fitting is, which can be seen as an advantage of the modelled methods (DM Kramers and Esprit). The influence of the user on the determined intensities remains generally low – below <~5% – if well separated peaks are considered. Even if overlapping peaks are considered the user influence is far less important than the choice of the program and its settings.

3.9.6   Real spectrum artefacts - incomplete charge collection

Incomplete charge collection (ICC) is a detector artefact which mainly affects low energy X-ray lines. Two effects contribute to the ICC. The first one is that charge carriers created close to the detector-front contact-interface are not fully collected. This loss of charge carriers leads to a reduced pulse height and therefore the assigned energy is too low (*111*) and this results in a low energy tail of the characteristic line. It can be assumed that the collection efficiency directly at the interface z_0 between contact and the active detector region is lowest and increases monotonically with penetration depth z till unity. The second contributing effect is that electrons created by an X-ray can be trapped at detector crystal defects and are thereby also lost for detection. This effect is highly depended on the quality of the EDX detector and can increase with the age of the detector. ICC leads to an asymmetric peak shape; a typical low energy tailing can be observed. Practically, this leads to the problem that, if the used detectors suffer from severe ICC the peaks cannot be fitted with a Gaussian function. Especially, the automated peak intensity determination with programs such as DM and Esprit, which cannot account for asymmetric peak shapes, provide significantly lower characteristic X-ray intensities. If e.g. an oxygen peak @ 0.523 keV acquired with one of the Super-X detectors (see Figure 36) the intensity in the tail resulting from the ICC contribution ranges from 10%-20% (of the total peak intensity) depending on the used detector. The problem gets even more severe if overlapping peaks in this energy regime are regarded, such as e.g. the overlap of Ti L an O K, because the programs cannot account for the changed shape and have difficulties unfolding the overlapping peaks.
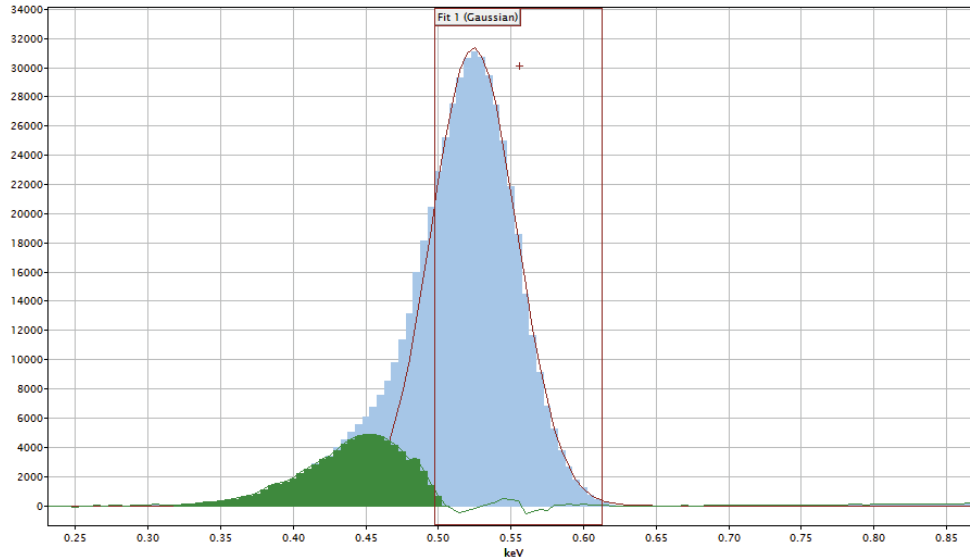
Figure 36: EDX spectrum of Al$_2$O$_3$ (Titan, SDD). Oxygen peak after linear background removal (blue), Gaussian shaped peak (red), residual signal (green).

It was tried to account for the problem of ICC by implementing an additional EDX line in the analytical database of DM. Practically, due to the four-quadrant detector system, another problem arises because the ICC is not the same for all four detectors. Hence, the shape of the peak always changes if a different combination of detectors is used (see Figure 37). To be able to exclude this influence during the determination of ζ-factors in this work only separated peaks in the low energy regime are considered. The intensity determination is done by choosing the 'right' approach for each line. For the oxygen line this was always the manual fit of two Gaussian peaks to include the intensity in the ICC peak. An example is shown later in this work.
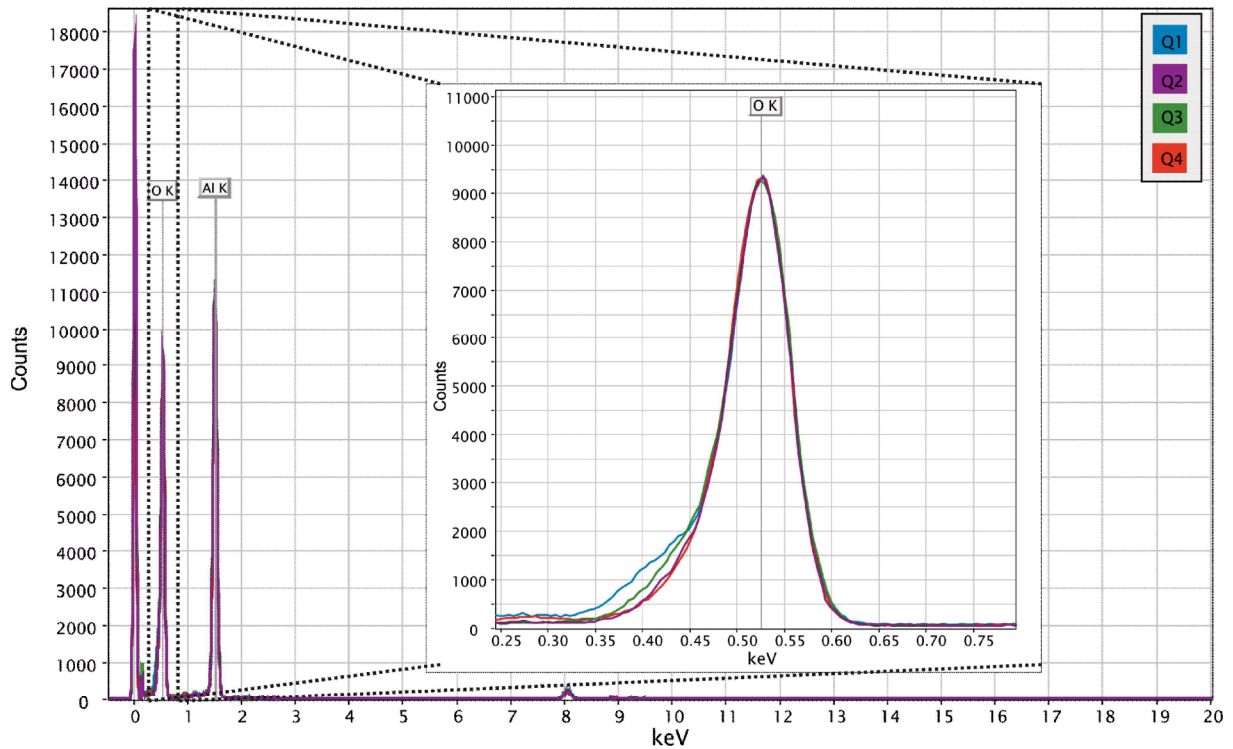
Figure 37: Al$_2$O$_3$ EDX spectrum for each detector (Q1 – blue, Q2 – purple, Q3 – green, Q4 – red) aligned to the maximum of the oxygen peak. The inset shows the shape of the oxygen peak for each detector.

3.9.7   Final intensity determination approach

After this close consideration on all aspects which have to be considered for background removal and intensity determination we cannot recommended one universal approach. The choice of the way the characteristic X-ray intensities are determined depends usually on the evaluated elements. In the low energy regime the bremsstrahlung is more significant and complex, compared to higher X-ray energies, and a simple approach like the window method, fails. Simple approaches also cannot be used if overlapping lines should be evaluated. In the following section we present the way we chose to evaluate the spectra used for ζ-factors determination.

For the elements presented here: O, Si and Al, different approaches for the intensity determination were used.

For the determination of the oxygen line always a fitting approach was chosen to account for the ICC. Initially, a background was fitted to the spectrum using Esprit 2.0 (see Figure 38).

Esprit 2.0 was chosen because it allows the user to correct the background fit so that it also matches the spectrum in the low energy region.
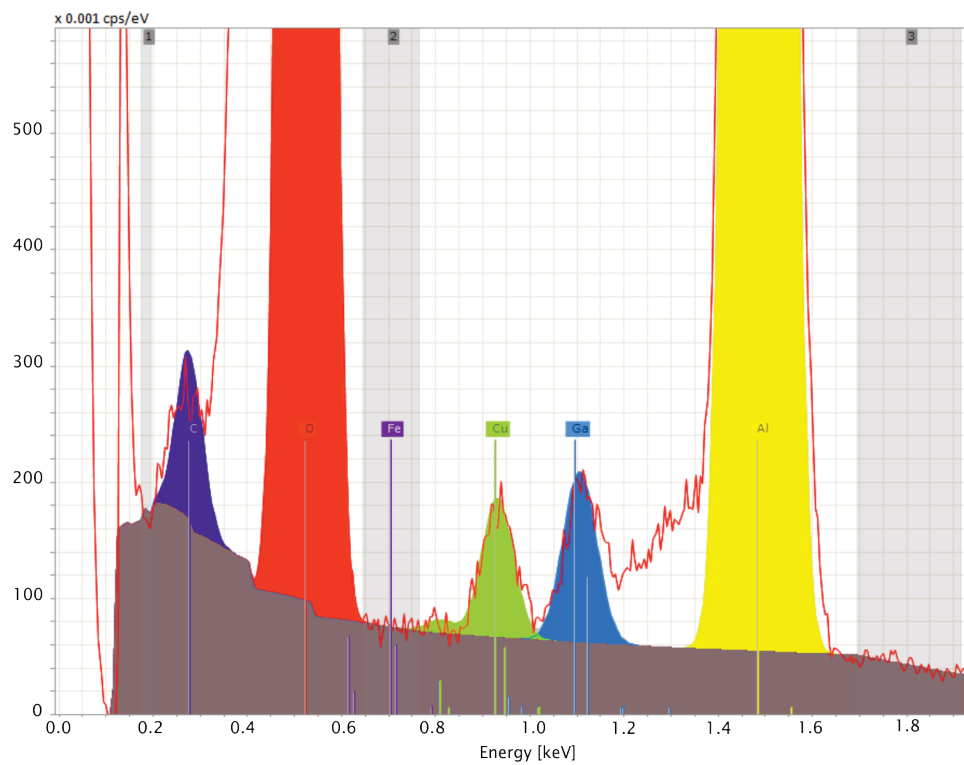

Figure 38: Background fit in Esprit 2.0

In Figure 39a an Al_2O_3 spectrum after background subtraction is shown. The same spectrum was further used to determine the characteristic intensity of oxygen and aluminum.
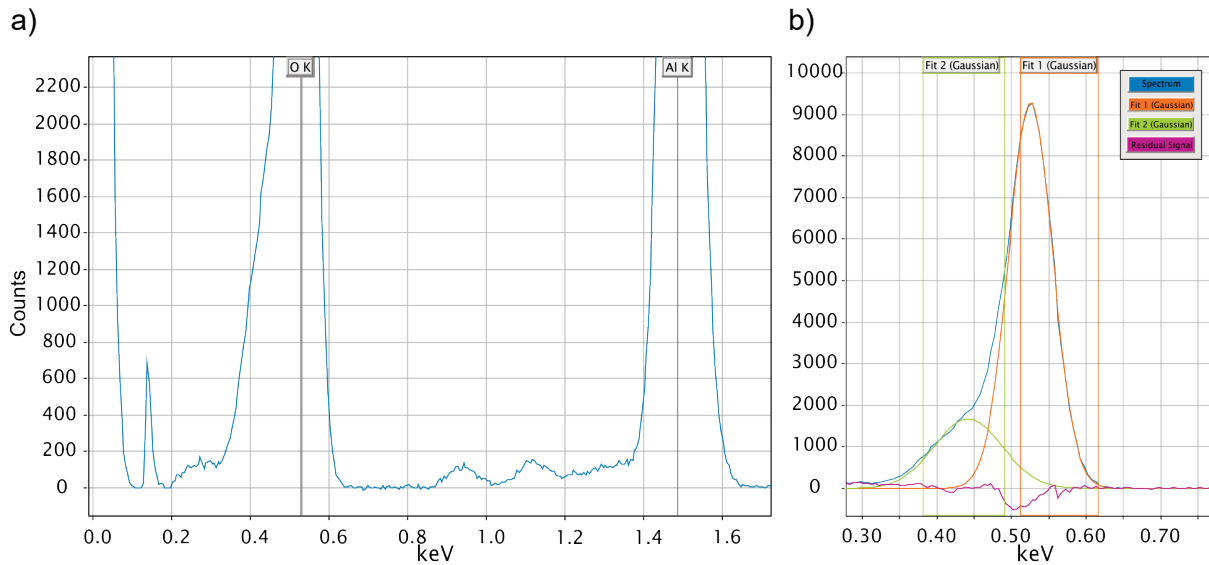
a)

b)

Figure 39: a) Background subtracted spectrum (using Esprit 2.0) b) Fit of two Gaussian functions (green, orange) to model the background corrected spectrum (blue) in the energy range of oxygen. In purple the residual signal is shown.

The intensity determination was done by fitting two Gaussian functions to the spectrum as shown in Figure 39b for oxygen. One Gaussian to measure the main intensity in the characteristic peak and the second for collecting the intensity lost due to the ICC. The parameters of the Gaussian function ($(\ ) = \quad \cdot\ ^{-\frac{(x-x_0)^2}{2\cdot\sigma^2}}$); the amplitude N and the FWHM; were further used to calculate the area I, of the Gaussian peak $= \int_{-\infty}^{\infty}(\ )\cdot \quad = \quad \cdot \quad \cdot \sqrt{2\cdot\ }$ with $\quad = 2\cdot\sqrt{2\cdot\ \ 2}\cdot$ leading to $= \quad \cdot \qquad \cdot\frac{1}{2}\sqrt{\frac{\pi}{2}}$.

The fitting windows of the Gaussian function were chosen so that the residual signal (in purple) was minimized.

Table 5: Effect of incomplete charge collection on determined intensities of the oxygen and aluminum signal.

	oxygen	residual	aluminum
		0.27 keV– 0.6 keV	
	(%)	(%)	(%)
Q1	20.4	0.8	2.5
Q2	16.9	1.1	2.2
Q3	20.3	0.6	2.8
Q4	17.0	0.3	2.2

In Table 5 the influence of the ICC on the intensity determination is shown. Moreover, the accuracy of the chosen approach can be assessed. The listed percentages all refer to the overall intensity determined for the corresponding elements (100% intensity corresponds to the sum of the area of both Gaussian functions). In the row 'residuals', the residual signals over an energy range of 0.275 keV to 0.625 keV were summed and also referred to the overall peak intensity.

It is obvious that the influence of the ICC is much more severe in case of oxygen. The ICC tail contains up to 20% of the intensity of the oxygen peak. In case of aluminum the effect is far less pronounced (<3%). The intensity remaining in the residual signal is below <2% of the oxygen signal, hence negligible for all detectors. The intensity determination for the presented materials Al_2O_3 and SiO_2 was done with the fitting approach. In case of Al and Si the top-hat method implemented in DM was used.

3.10   Summed Results

Under consideration of all aspects discussed above ζ-factors for the elements: Si, O and Al are presented. As already mentioned the samples were a single crystalline silicon wafer, a quartz (SiO_2), a piece of pure aluminium and a sapphire (Al_2O_3). The sample preparation, measurement and evaluation is done as explained in the chapters before. From each material a lamella and a rod was prepared. By using the geometry of the rod, λ was gained for each material and so the absolute thickness of the lamella was available. The EDX signal was acquired for each detector separately tilted toward each detector. The evaluation of the spectra was done, in case of the oxygen containing samples, by removing the background using esprit

and determining the characteristic intensities by fitting Gaussian functions to the peaks. In case of the pure element standards, Al and Si, the top-hat method implemented in DM was used.

Table 6 summarizes the determined ζ-factors. The variations within one measurement and between the measurements of different materials are rather high (up to 20% of the mean value). This can be seen even more clearly if Figure 40, Figure 41 and Figure 42 are considered. The figures show the relative deviation of the calculated mean value (which is also depicted). Some of the higher deviations seen in the figures can be explained others remain.

Table 6: ζ-factor for Si, O and Al for Q1-Q4 (Q2 and Q3 only Al and O) based on the measurement of four samples (Si, SiO$_2$, Al, and Al$_2$O$_3$) and the relative standard deviation are given.

	Si		O		Al	
Q1	Mean	%σ	Mean	%σ	Mean	%σ
Si	504	4%				
SiO$_2$	564	13%	519	13%		
Al					534	6%
Al$_2$O$_3$			475	16%	539	15%
Q2						
Al					483	3%
Al$_2$O$_3$			538	15%	616	13%
Q3						
Al					498	2%
Al$_2$O$_3$			513	9%	582	10%
Q4						
Si	523	3%				
SiO$_2$	548	18%	524	20%		
Al					560	3%
Al$_2$O$_3$			404	8%	461	11%

For all materials the mean free path length was determined. The mean free path length for Si was 187 nm, for SiO$_2$ 181 nm, for Al 152 nm and for Al$_2$O$_3$ 130 nm (for more details see chapter 3.7.1). All measurements were done in STEM mode with a beam current range from 0.27 nA -0.32 nA.
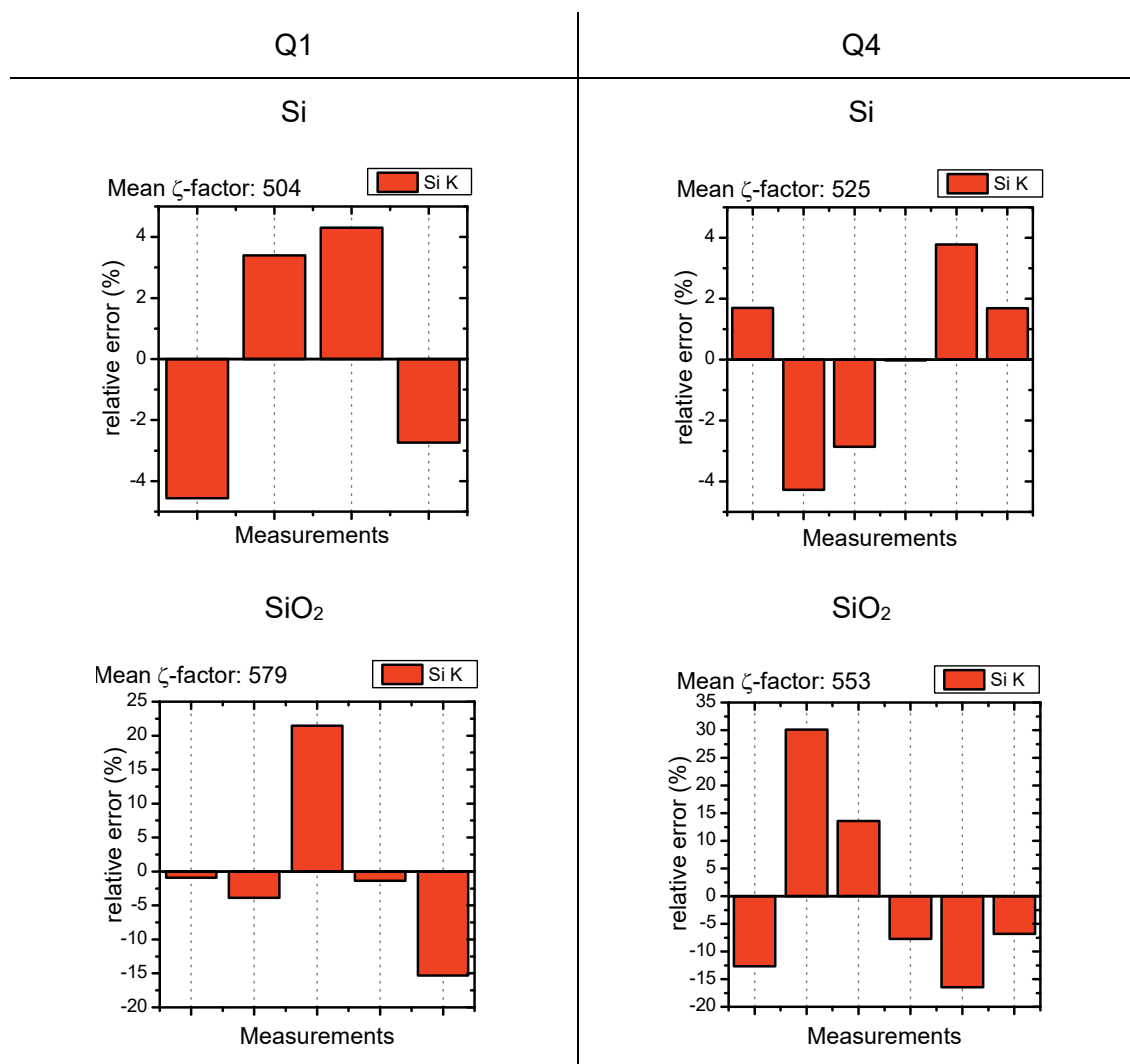
Figure 40: Relative deviation from mean ζ-factor value for Q1 (left column) and Q4 (right column) determined using a pure silicon lamella (first row) and a quartz crystal – SiO₂ (second row). The intensities were determined with the Top-hat method implemented in DM.
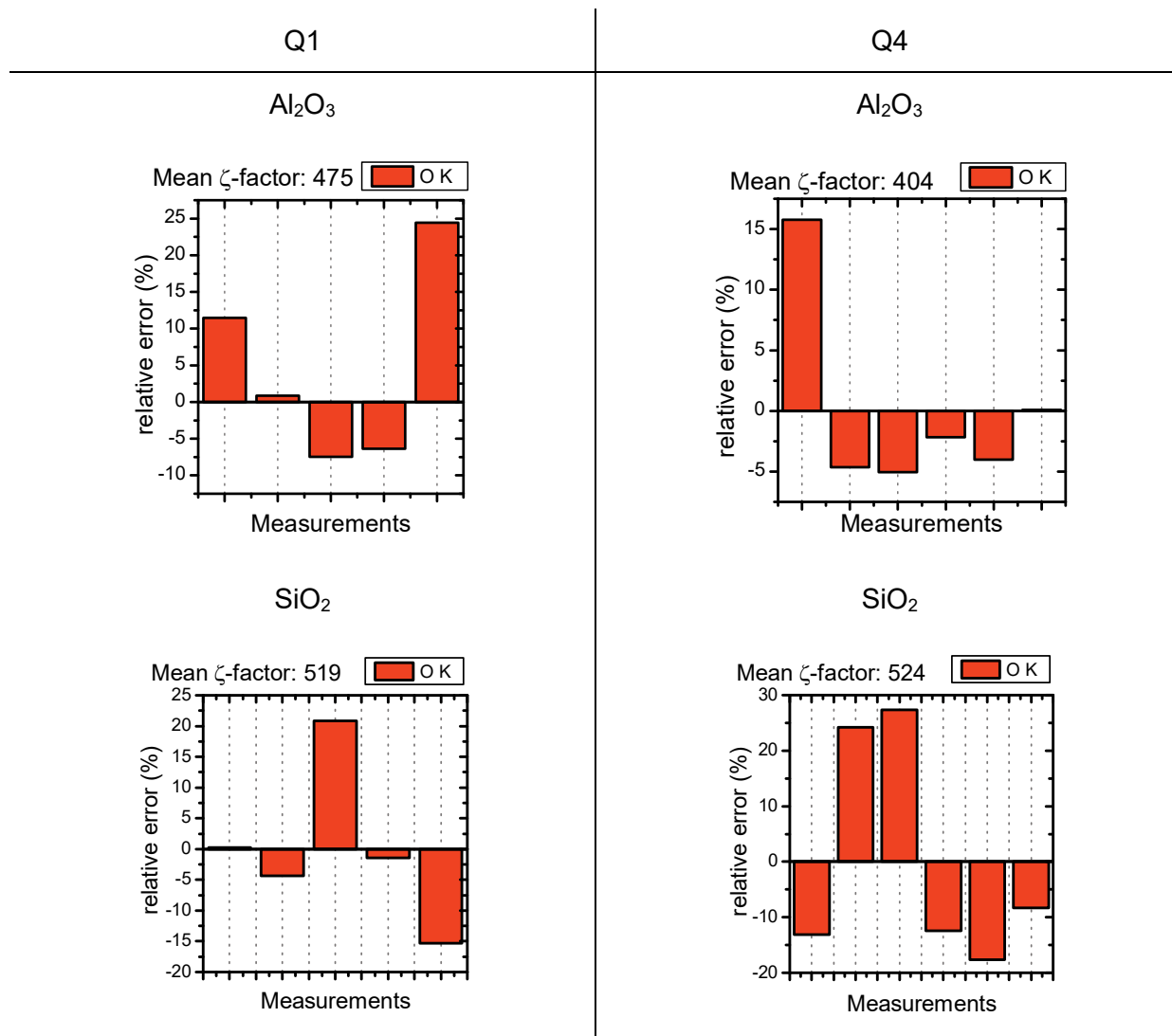
Q1	Q4
Al₂O₃	Al₂O₃

Mean ζ-factor: 475   OK

Mean ζ-factor: 404   OK

SiO₂   SiO₂

Mean ζ-factor: 519   OK

Mean ζ-factor: 524   OK

Figure 41: Relative deviation from mean ζ-factor value for Q1 (left column) and Q4 (right column) determined using a sapphire – Al₂O₃ lamella (first row) and a quartz crystal – SiO₂ (second row). The intensities were determined using a fitting approach described in chapter 3.9.7.
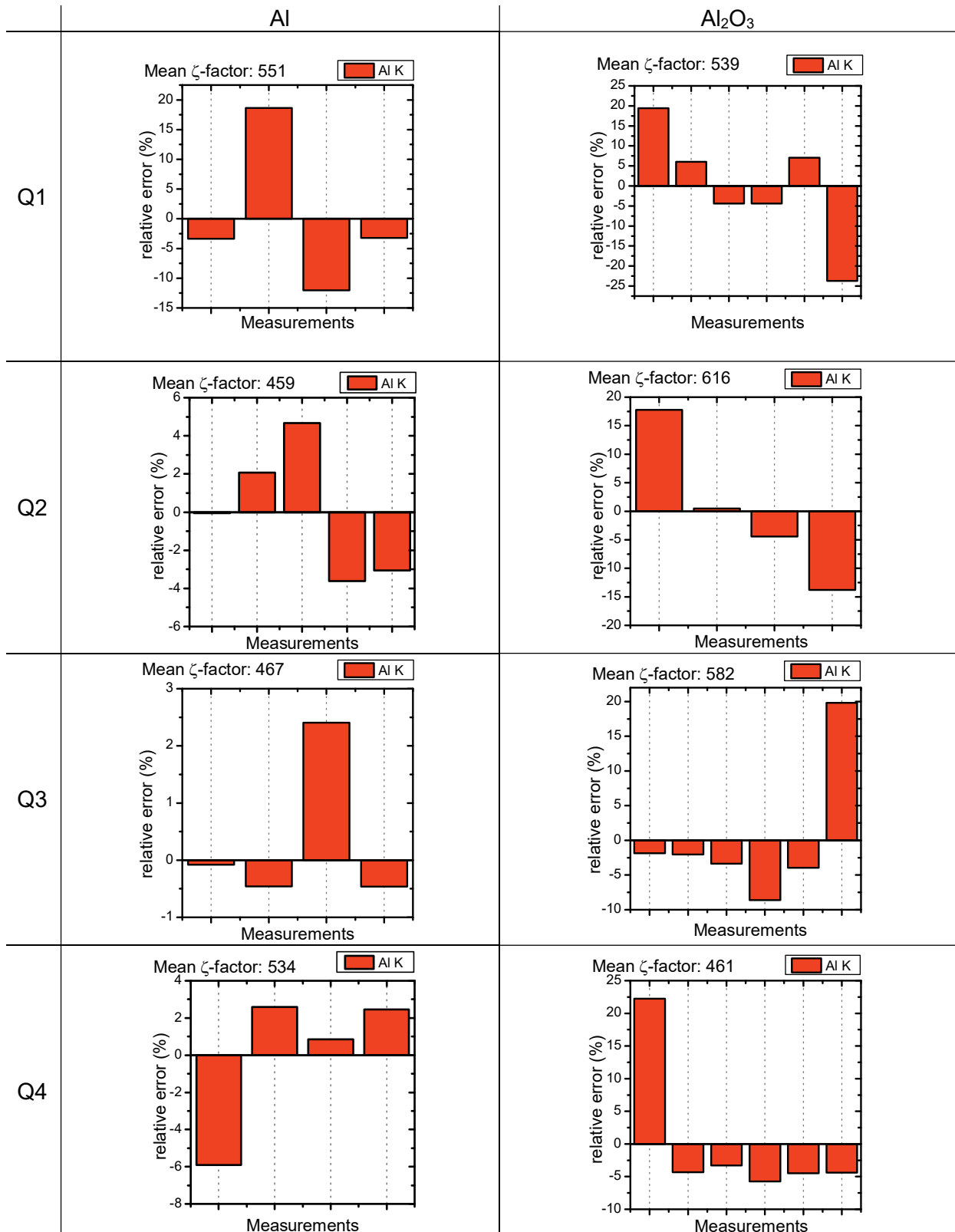
Figure 42: Relative deviation from mean ζ-factor value for Q1 (top row) to Q4 (right row) determined using a pure aluminum lamella (first column) and a sapphire – Al₂O₃ (second column). The intensities were determined using a fitting approach described in chapter 3.9.7.

Deviations of ζ-factor comparing one material to the other

The difference between the determined ζ-factor for aluminum using the aluminum standard (Figure 42) or the Al_2O_3 sample (Figure 41) can be related to: an incorrectly assumed density for one of the materials, to an altered density/composition during the preparation or the investigation of one of the materials, or to a wrongly determined mean free path length. All these influences would have the effect of an erroneous ζ-factor determined with one material. Whereas ζ_O from Al_2O_3 and SiO_2 (the ζ-factor from Al_2O_3 is lower than ζ-factor of SiO_2) or ζ_{Si} from silicon and SiO_2 (pure silicon gave a slightly lower ζ-factor than using SiO_2) show a tendency in one direction this is not the case for ζ_{Al} from aluminum and Al_2O_3 (at least not for Q2 and Q3).

An inaccurately determined thickness or modified density would also have an effect on the absorption correction and thereby also on the ratio of ζ_O/ ζ_{Si}. If we assume a mean free path length of ±20% in case of SiO_2 (so 223 nm for +20% and 149 nm for -20%) for example, the ratio for Q1 and Q4 would change by ±3%. If we assume even ±50% of the mean free path we would end up with a changed ζ_O/ ζ_{Si} ratio below ±10% (8% for a mean free path length of 289 nm and 9% for 93 nm). So this influence cannot solely explain the deviations within a material.

Deviations within the measurement of one material

Some of the values deviating within the measurement of one material can be explained, such as e.g. the first one of the ζ_{Al} (using Al_2O_3). This value was acquired at a different measuring series which will lead to a slightly different inserted Omniprobe grid and thus to a different geometry. The effects will be explained in detail in the following chapter 0. This effect can also influence the agreement between different materials due to the changed sample geometry e.g. a slightly bent FIB grid.

Just looking for obvious differences the second and the third measurement of the ζ_O for Q4 (in SiO_2) e.g. were done on a thinner sample area (t/λ ~0.6 and 0.4 compared to the others 0.9 - 1.5). This could lead to the conclusion that the sample properties were different for thinner sample regions or the absorption correction was wrong due to a wrong assumed total thickness. But as already discussed above only a wrong absorption correction does not have this influence and therefore, altered sample properties are more likely. Interestingly, the ratio of Si/O counts remains relatively stable for all thicknesses and all measurements 0.94 ±0.05 for all changes in geometry and measurement series. In case of Al_2O_3 the ratio is 0.88 ±0.06.

Hence a change in composition is rather unlikely. If we take a closer look on the ratio of the two oxides, several observations can be made:

In Figure 43 results for the measurements on SiO_2 are summarized. Different parameters are plotted over the thickness. Figure 43a shows the intensity increase for Si and O X-ray counts with increasing thickness. The counts are normalized using the electron dose making the values independent of the life time and the probe current. As can be expected the X-ray counts increase with increasing sample thickness. It has to be mentioned that the effect of differences between the detectors is neglected (e.g. detector efficiency) in this plot. In Figure 43b on the left axis the ratio of the O counts to the Si counts are plotted. In this case they are not normalized because the effects are cancelling out anyway. Different detector properties are also cancelling out. The ratio generally decreases with increasing thickness which can be attributed to the increased absorption of the O K X-rays with increasing sample thickness. On the right axis the ratio of the ζ-factor is plotted. It can be seen that the absorption effect is compensated. The first value at a sample thickness of approximately 88 nm is statistically relevant (within 3σ) but very close to 3σ. If it is neglected the relative deviation of the ζ_O / ζ_{Si} ratio drops from 5.4% to 1.8%. Generally, the plot shows that the ζ_O / ζ_{Si} ratio remains almost constant. In Figure 43c the ζ-factor of oxygen and silicon against the thickness are plotted. One can observe a change of the ζ-factor with the sample thickness. This effect cannot necessarily be attributed to the thickness but can also be an effect of a change in mass-thickness, which can also be attributed to a change in the density of the material. It can be stated for sure that the relative thickness does not change over the measurement but it cannot be assured that the overall density during e.g. FIB preparation does not change. This effect of an alteration of the density due to a change in surface density would be more pronounced at thinner sample regions which could also explain the effect.

In Figure 44, the same plots as in Figure 43, are shown, but this time for the Al_2O_3 measurements. The only difference between the Al_2O_3 measurements and those of SiO_2 are, that in case of Al_2O_3 all 4 quadrants were measured, and that different measurement series were performed. In Figure 44a the trend is, unsurprisingly, the same as in Figure 43a. But in case of Figure 44b and Figure 44c no trend can be seen; just a wide overall variation can be observed. This can be attributed to geometrical effects due to the different measurement series and thereby slightly different conditions. This slight change in geometry can lead to an energy dependent absorption and thereby a changed Al:O ratio. A change in collection angle, originating from an incomplete illumination of a detector, would lead to increased ζ-factors. The ζ-factors are inversely proportional to the measured X-ray intensities (for more detail see chapter 4.1.1). In this case values for all 4 detectors were acquired which also could lead to a

greater variation. It could also be that the effect of a mass-thickness dependent ζ-factor cannot be observed in case of the Al_2O_3 sample. It also has to be noted that there are more values for Al_2O_3 and it cannot be assured that the effect in SiO_2 is not only due to bad statistics. Another plausible, but maybe unlikely influence, could arise due to aspect of detector properties. The Al_2O_3 measurements were done a year before the SiO_2. The problem with the detectors switching off did progress and worsen over time and it is not known if this has any further influence on the counted X-rays.
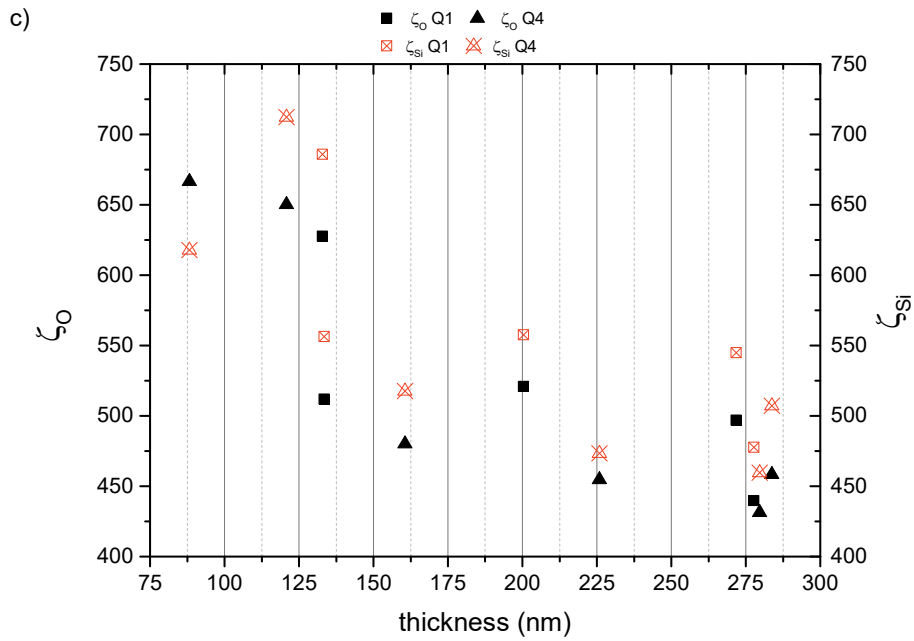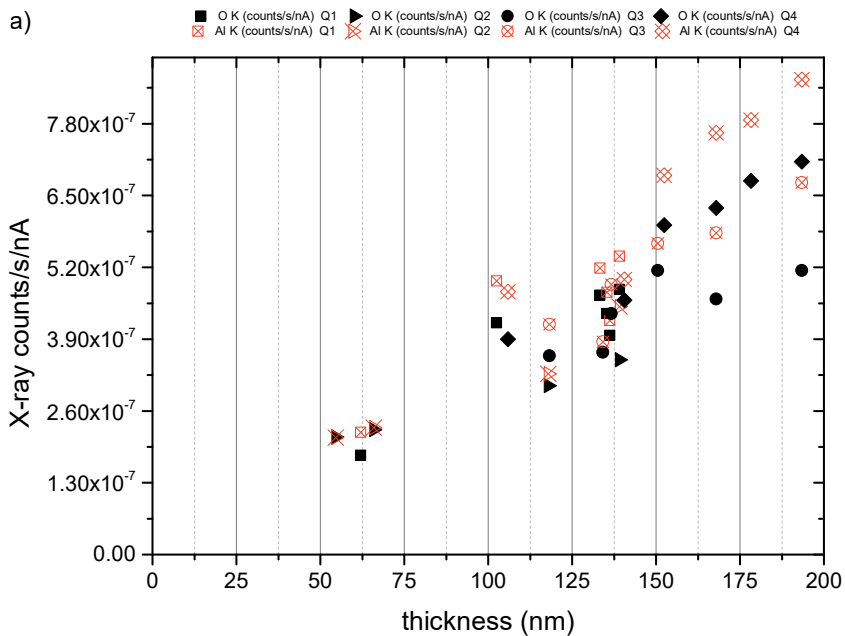
a)

b)

c)
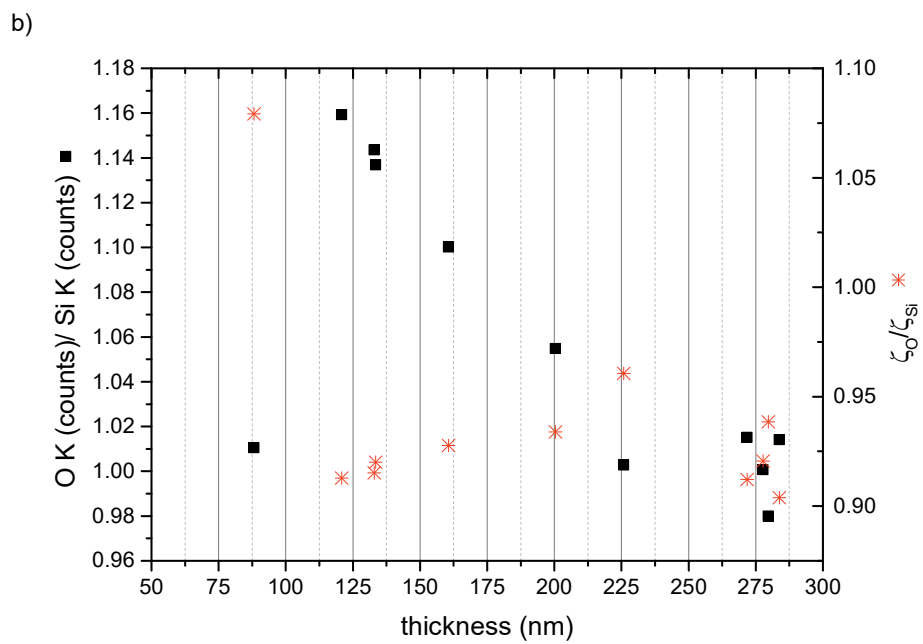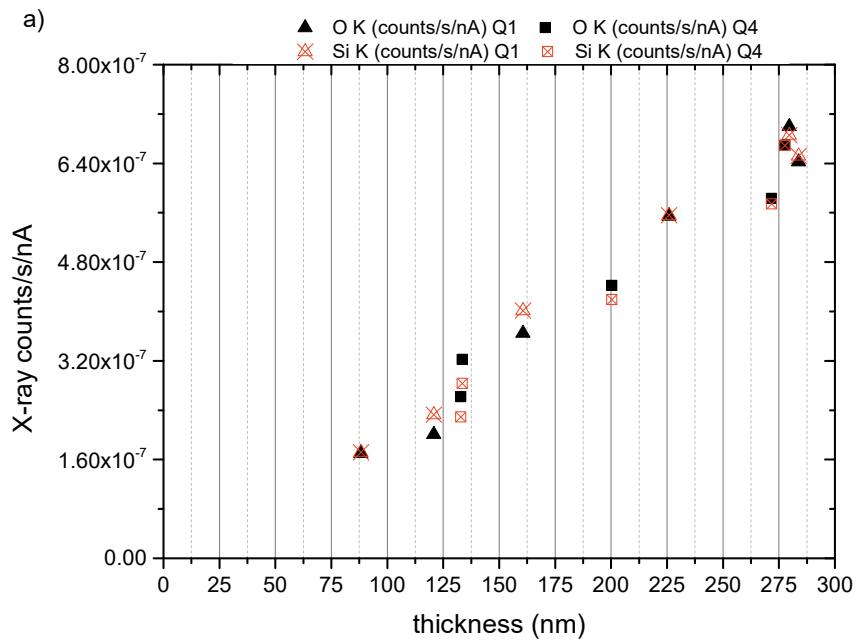
Figure 43: In all graphs different parameters of the SiO₂ sample of Q1 and Q4 are plotted against the sample thickness. In (a) the X-ray counts (per electron dose) vs thickness; in (b) the ratio of the O K/ Si K counts (left axis) and the ζ_O/ ζ_{Si} (right axis) vs thickness and in (c) the ζ-factors vs thickness.
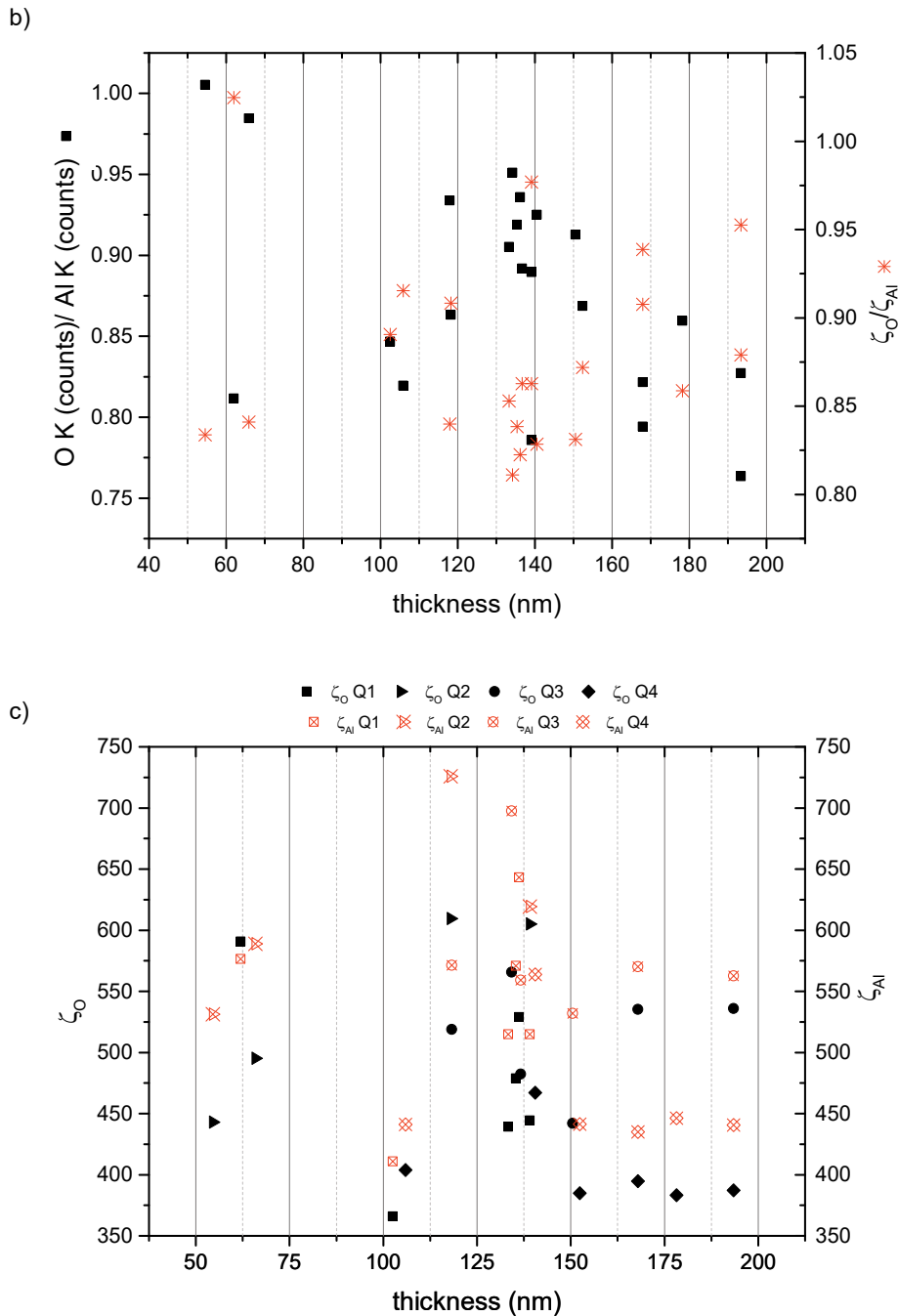
a)

Figure 44: In all graphs different parameters of Q1-Q4 of the Al$_2$O$_3$ sample are plotted against the sample thickness. In (a) the X-ray counts (per electron dose) vs the thickness; in (b) the ratio of the O K/ Al K counts (left axis) and the ζ$_O$/ ζ$_{Al}$ (right axis) vs the thickness and in (c) the ζ-factors vs the thickness.

In case of the pure element standards, Al and Si, no consideration on the composition considering the ratio of elements can be made. In both cases the values are rather stable (deviations <±5%) except the measurements for the ζ$_{Al}$ with Q1. If Figure 45 is considered in

case of Q1 it can be noted that the values are not trustworthy, as far as the agreement between the counts/s/nA with the sample thickness is considered. This should be a linear relation, neglecting absorption, as it is found for all other detectors. The comparison with simulations also implies that the measurements with Q1 are not reliable. If the four spectra are simulated with DTSAII (also used in 3.9.5) using the same conditions as for the measurements, the order of the measured and simulated counts/s/nA is different. It might be possible that an absorption in e.g. parts of the holder or the sample did have an influence because all measurements were done on different positions. It could also be the case that something went wrong with the detectors. Current fluctuations and a wrongly determined thickness are rather unrealistic but could have also this effect.
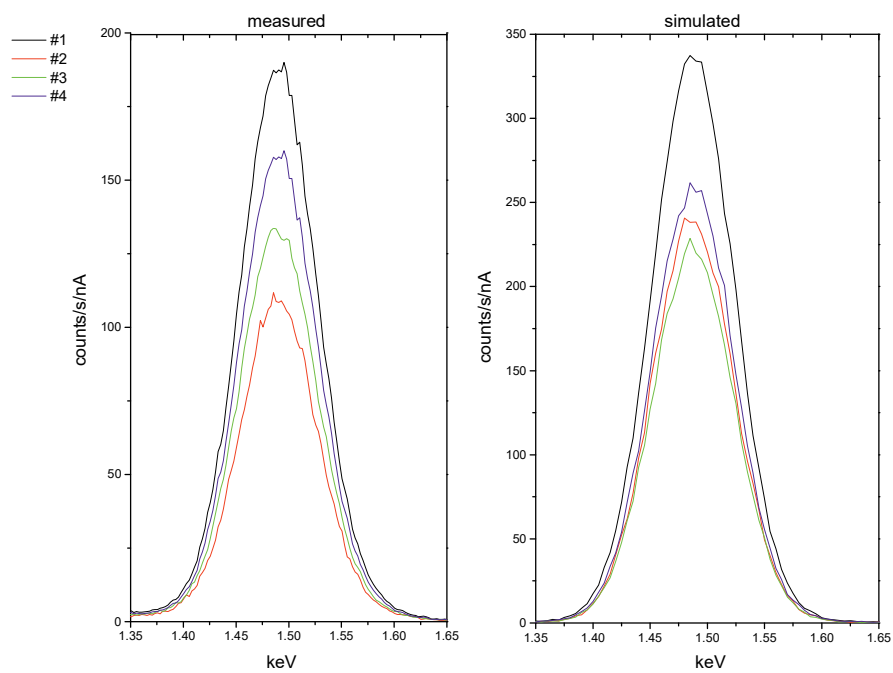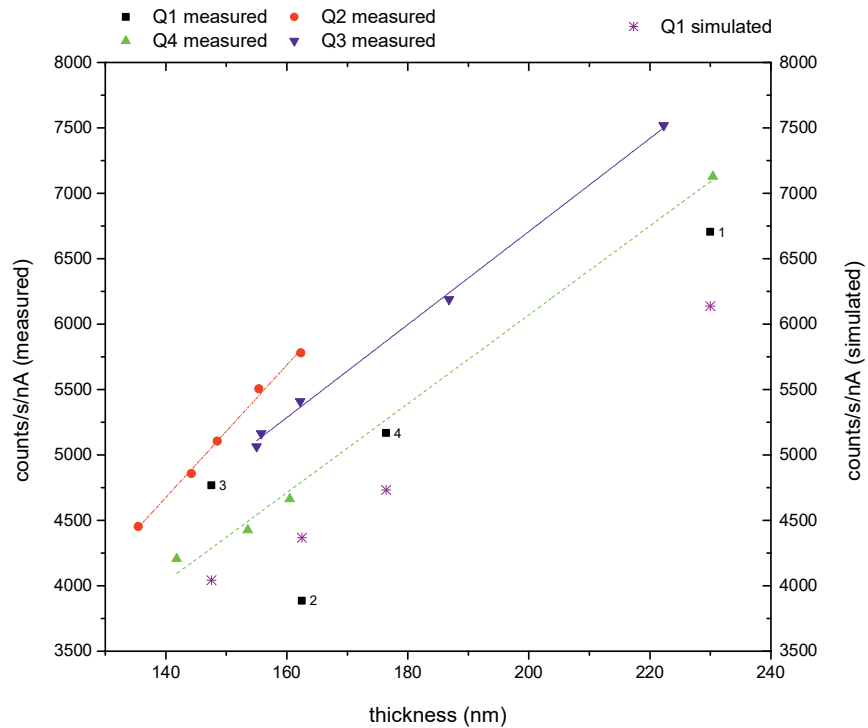
Figure 45: Aluminum measurements. In the first row the counts/s/nA for all quadrants are shown (right axis) and the simulated counts/s/nA for the conditions of Q1. In the second row the measured (left) and simulated (right) spectra are plotted.

Summary

The reliability of the presented ζ-factors is not satisfying. However, we have learned a lot on the determination of sensitivity values on a Super-X system but do not completely understand all influences yet.

The approach by (*75*) is still a good approach but for light elements standards one faces the same challenges as with k-factor standards. It is hard to ensure that the material stays unchanged for multi element systems.

A much more elegant way, which we also tried, would be to use 2D materials like BN or Graphene if available for the element. One would exactly know the thickness and if the composition changes one could immediately tell. We tried to determine the ζ-factors of B, N and C using this approach but besides the limitation to 60 kV acceleration voltage (due to sample stability) the used detector system was not able to work with such low count rates. This was a general problem of the used Super-X system; the detectors tended to switch off if the count rate was too low (the threshold level changed but was around <300cps). Therefore, one could not use very thin sample areas and also the displayed measuring time could be wrong. This is also the reason why no measurements for SiO_2 exist for the other two detectors; it was not possible to get enough X-ray counts that the detectors did start to measure. The threshold value that the detector did switch on wat not achievable with that material and at the current state of the detectors. Moreover, this problem became worse with time, and will finally lead to an exchange of the whole detection system. Nevertheless, these measurements presented here were all made with that system.

We also found out that using DM spectrum images is not feasible at our system, because the measuring time given by DM was wrong. Therefore, we chose the method of scanning over an ROI and acquired singe spectra.

We also spent a lot of work on the evaluation of the X-ray spectra. We focused on the reproducibility of the gained characteristic X-rays using different programs and different operators. It has to be stated again that different programs lead to rather different results. Therefore, it is important that the same program (and also version) is used during the determination and the usage of sensitivity factors. Especially, because some programs include the whole family of X-rays and others do not. As far as results using DM are considered, we identified the top-hat method as the method showing the best reproducibility if different people are evaluating the same spectrum. Considering the correctness of results the top-hat method

has difficulties in the low energy regime and using a different approach would lead to better results.

Another aspect, which we identified to be very important for the determination of sensitivity factors, is the geometry. We can state that on a four-quadrant detector system the sensitivity factor determination has to be done for each quadrant separately because of geometrical effects. Doing the measurements separately is not enough; moreover a full illumination of the detectors has to be assured. This full illumination is not assured if one measures at 0° holder tilt. Even worse, the illuminated detector area strongly depends on the position of the area of interested inside the specimen holder because of the shadow the specimen holder casts on the detectors. After we realized that this has a severe effect we tried to ensure a full illumination by tilting toward the detector by $\alpha = 15°$ and measuring each detector separately. Still, the aspect of not illuminating the whole detector is identified to have a severe effect on the gained characteristic X-ray counts. Therefore, further work was devoted to the subject of geometry.

4   Geometry in EDXS

Geometry in EDXS is another big topic in this thesis. This arose from two circumstances. Firstly, the precise characterization of the Super-X system in terms of geometry was a goal. This is needed to be able to exactly calculate the path length of a characteristic X-ray through the sample to the detectors. This path length is mandatory to perform an accurate absorption correction using the ζ-factor method. In the progress of the determination of the detector positions we learned that the geometry may have even more influence on the sensitivity factors. In the following chapters a short recapitulation of geometry aspects in EDXS quantification is given. The experiments and simulations, used to determine the exact detector positions are explained. Finally, the results are presented and the effects on X-ray measurements are discussed.

4.1   Linking geometry to ζ-factors

The background of the ζ-factor method is already discussed in chapter 3.2.2. The geometry comes into play already at the definition of the X-ray intensity (equation (3.7)), by the solid angle Ω. Therefore, the parameter is also found in the definition of the ζ-factor (equation (3.8)). The solid angle defines the amount of X-rays collected. It is assumed that X-rays are isotopically emitted in all directions from a point source. An EDXS detector is only able to collect a minority of the emitted X-rays because of its limited area. An ideal EDXS detector would have a collection angle of 4π steradians and would thereby collect 100% of the emitted X-rays, which is technically not possible. Nevertheless, with the advent of silicon drift detectors (*112, 113*), EDXS systems got more and more sophisticated: In order to improve collection efficiency, large area X-ray detectors (up to 100 mm^2) and multi detector systems (2-4 individual detectors) (*114*) have become common in analytical transmission TEM (*115, 116*). SDDs provide the possibility to increase the area of the detector without a loss in energy resolution.

In the FEI Super-X system the increase in detector area is realized by using four detector quadrants as schematically shown in Figure 46. Although this gain in active detector area provides higher detection sensitivity, it also leads to a higher geometrical complexity of EDXS detector systems and invokes several new aspects to be considered for EDXS quantification. On the one hand, with a relatively large detector area located quite close to the specimen, conventional procedures including for instance the calculation of the solid angle turn out to be

inappropriate and not accurate enough anymore (*117*). On the other hand, the geometrical arrangement of the EDXS detectors, sample and specimen holder may strongly influence the active detector area due to casting shadows.

The take-off angle α_{TO} is, besides Ω, the second geometric factor influencing quantitative EDXS. The take-off angle α_{TO} defines the path length of the X-rays through the sample (see (3.11)) and is therefore essential for an absorption correction in the specimen. The take-off angle is directly related to the position of the detectors.

The two important parameters involved in EDXS quantification related to detector geometry are the detector solid angle Ω and the take-off angle α_{TO} (compare equation (3.13)). If the exact detector position and its size are known, the solid and take-off angles can be calculated. In multi-detector systems, as the Super-X system, this step must be performed for each detector separately. We concentrate on determining the actual positions of the detectors, which are defined by the elevation angle ϑ_e directly influencing the take-off angle, the distance from the sample d and the azimuthal angle ϑ_A (depicted in Figure 46).
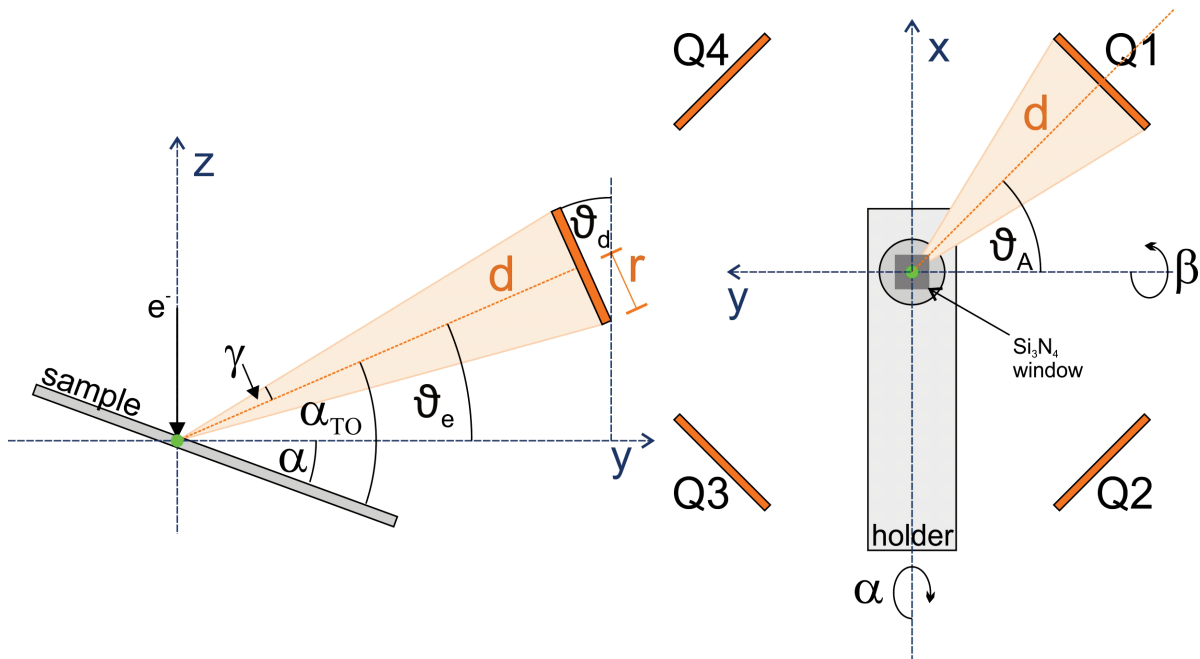
Figure 46: Left: Schematic of detector geometry. Specimen tilt: α; take-off angle: α_{TO}; detector elevation angle: ϑ_e; angle between the detector and the optical axis: ϑ_d; cone opening half-angle: γ; radius of detector disc: r; and detector distance: d. Right: Top view of the holder scheme (azimuthal angle: ϑ_A). The coordinates of x and y and the directions of the α and β specimen tilts are indicated. The positive z-axis extends out of the drawing plane (toward the electron gun).

4.1.1 Detector solid angle

The detector solid angle is so far mainly used as a measure for the collection efficiency of EDXS detectors. EDX manufacturers promote systems with bigger collection angles. The bigger the solid angle is the better the collection efficiency of the detector. In principle this fact is true, a larger detector area, as close as possible to the specimen provides the best collection efficiency. As far as no quantitative EDXS is used, nothing will change compared to conventional small EDXS detector systems and an increase in collection angle goes along with an increase in collection efficiency. This is also true for quantitative EDXS using a ratio approach without absorption correction because influence of the solid angle is canceled out in quantification. Because if a ratio approach is used the solid angle cancel out during quantification. In most common single detector systems the solid angle usually is constant. The situation increases in complexity for a-four-quadrant detector system. Considering a four quadrant system, as the Super-X system, using all four quadrants at once to work with the maximum possible collection angle, a full illumination of all four quadrants has to be given at all time to have a constant solid angle. The full illumination of all four quadrants is not possible

at any holder tilt using standard specimen holders due to geometrical reasons. This is mainly due to the holder, which casts a shadow onto the detectors.

If there is a change in solid angle, it has two effects:

During the determination of ζ-factors, as done throughout this thesis, it has the effect that a different ζ-factor is determined each time the solid angle changes because the ζ-factor is directly related to the intensities collected by the detector. So, if e.g. only half of the detector area is illuminated a 100 nm thick sample will provide only half of its counts and the ζ-factor will by twice as large as if the detector would be fully illuminated.

Assuming that all ζ-factors were determined or calculated with the same solid angle, but the effective solid angle during the EDXS acquisition of an unknown specimen is different, the gained concentration values will be correct (Ω cancels out). The mass thickness value however, also gained using the ζ-factor technique, will be incorrect. Therefore, the measured X-ray intensities in the spectrum must experience the identical solid angle as the measured or calculated ζ-factors.

Typically, the solid angle remains constant for a given system. People tilt toward the detector in a single-detector system to increase the take-off angle (less absorption) and to avoid shadowing the detector. However, tilting toward one detector of a multi-detector system will create shadowing for other detectors. Therefore, a tilt of the specimen or a movement of the specimen (i.e., movement of the specimen holder's center away from the optical axis) will effectively change the solid angle of one or more detectors.

If a full illuminated detector is considered the solid angle is given by the following parameters. The shape and area of the detector A_{det} (or radius r, if circular), the distance from the specimen d, and the tilt of the detector surface with respect to the optical axis ϑ_d are required to calculate the detectors solid angle. Such an arrangement of a single EDXS detector is shown in Figure 46 (left).

If the tilt angle of the detector ϑ_d is equal to the elevation angle ϑ_e, the detector normal is directly pointing to the specimen and the solid angle Ω covered by a circular detector can be computed:

$$\Omega = 2\pi \left(1 - \cos\gamma\right) \tag{4.1}$$

γ is half the apex angle of the cone (see Figure 46). Introducing the radius r of the detector and its distance from the sample d this equation becomes:

$$\Omega = 2\pi \left(1 - \frac{1}{\sqrt{1 + (r/d)^2}} \right) \tag{4.2}$$

This expression for the solid angle is equivalent to the formula presented in (*117*). The radius and the area of the detector disc are usually known, but the distance is not. However, the expression for $\vartheta_d \neq \vartheta_e$ is more complicated and can be solved using elliptic integrals (*118*), which we used for the calculation of solid angles. Other formulae for an approximation of this general case have been proposed elsewhere (*117*).

4.1.2 Detector take-off angle

The take-off angle of an X-ray detector is defined by the angle between the surface of the specimen and the line from the specimen to the center of the detector (compare Figure 46). Some geometrical considerations lead to a formula in which the take-off angle α_{TO} can be computed from the specimen tilt angles α and β, the detector elevation angle ϑ_e, and the detector azimuthal angle ϑ_A.

$$\sin \alpha_{TO} = \frac{\cos \vartheta_e (\sin \beta \cos \vartheta_A - \sin \alpha \, \cos \beta \, \sin \vartheta_A) + \cos \alpha \, \cos \beta \, \sin \vartheta_e}{\sqrt{(\quad_A - \quad_A)^2 + (\quad)^2}} \tag{4.3}$$

This equation was already derived in (*119*) but our equation looks slightly differently but yields the same results (*120*). In the conventional EDXS arrangement $\vartheta_A = 90°$ (the detector is oriented perpendicular to the α-tilt axis) and $\beta = 0°$, this equation converts to the frequently used relationship between specimen tilt and take-off angle:

$$\alpha_{TO,90°} = \vartheta_e + \alpha \tag{4.4}$$

In a four-detector system, the detectors are placed symmetrically around the optical axis and the azimuthal angles for the individual detectors are 45°, 135°, 225°, and 315° (counted counterclockwise from the positive *x* axis, which is between Q1 and Q4, compare Figure 46). Each detector will have a different take-off angle unless the specimen is not tilted. Table 7 depicts the result for a specimen tilt of α = -10° and β = 3° (ϑ_e = 18°):

Table 7: Take-off angle for the Super-X system with α = -10°, β = 3°, ϑ_e = 18°.

detector	ϑ_A	α_{TO}
Q1	315°	13.0°
Q2	225°	8.8°
Q3	135°	23.0°
Q4	45°	27.2°

Whereas the specimen tilt angles α and β, as well as the azimuthal angle ϑ_A are typically well defined, the user must rely on manufacturer information for the elevation angle ϑ_e. A method has been proposed to obtain this angle experimentally using coherent Bremsstrahlung (*121*). In previous experiments, we found elevation angles significantly higher than the manufacturer's value (*7*). The reason for this discrepancy remains unclear.

In addition, the take-off angle can be different for different parts on the active area of detector. If small detectors are used this effect does not play a major role. Although this effect was not taken into account in this thesis, it might have a significant influence on the absorption correction and consequently on the quantitative results when big solid angle detectors are used. So far, detectors were small and far away enough that only one take-off angle was used to calculate the path length of X-rays in the specimen. If the detector moves closer to the specimen or increases in area this assumption is not completely valid. This effect is not part of this thesis but should not be forgotten. For more information see e.g. (*122*).

4.1.3   Influence of geometry on EDXS in literature

Groups doing tomography always had to deal with the effect of shadowing of the EDXS detector because tilting the specimen inevitable leads to a holder shadow casted on the EDXS detector. On a four-quadrant detector system the situation is even more complex for tomography experiments but also for conventional, single detector systems because shadowing one of the quadrants is unavoidable. An optimal solution for such a system would be to get rid of all parts of the holder, which reduce characteristic X-rays produced by the specimen to reach the EDXS detectors. This concept is realized e.g. with the On-Axis Rotation Tomography Holder by Fischione (*123*), which allows a 360° tilt, and similar holders using rod shaped samples (*124*). This holder geometry completely avoids any shadowing of the detectors and uses the full collection angle of all detectors. Nonetheless, many samples do not allow the usage of such a holder. Hence, shadowing of the detectors by the holder is an

essential factor for the efficiency of the EDXS detection system. Just recently Slater et al. (*125, 126*) and Yeoh et al. (*127*) reported the effect of holder shadowing during EDXS tomography on a four-detector system. Both worked with a simplified holder model. Xu et al. (*128*) considered standard EDXS measurements and used a more sophisticated holder model and also included the effect of the beryllium specimen carrier. Nevertheless, all three authors did not measure the detector positions.

Considering the geometry of EDXS detector Zaluzec's work needs to be mentioned too. He has done a lot of work on the geometry of EDXS systems (*117, 129, 130*). Calculating the solid angle for a variety of detector shapes and positions, studying the influence parts reducing the active detector area (as e.g.: collimators, shadows of window and sample grid bars and the specimen holder).

4.2   Experiment and simulation

Our aim was to model the geometrical situation as realistically as possible, particularly without relying on the manufacturer's values for the detector positions, to be able to determine precisely the position of the four quadrants in our Super-X system. The exact position is needed to assess the influence of geometry on quantitative EDXS. As already discussed earlier (compare chapter 4.1.1 and 4.1.2) the geometrical data is of huge importance to perform absorption corrected quantitative EDXS (solid and take-off angle). Both geometrical parameters can be determined if the exact positions of the detectors are known. The position is defined by the distance and the elevation angle. Therefore, a tilting experiment was performed to assess the detected X-rays with respect to the holder α-tilt. The same tilt experiment was simulated using a precise specimen holder model to varying detector positions. Each tilt simulation with a certain detector position gave a so-called shadowing curve, illuminated detector area at a given α-tilt. These shadowing curves were compared with the intensities obtained by the tilting experiment. Thereby the detector positions could be experimentally determined. In the following chapters the experimental measurements and the simulation are explained in more detail.

4.2.1   Experiments

For the experimental measurements an appropriate sample was needed. The sample had to fulfil certain criteria to allow comparison with the simulations. It has to be homogenous in composition. The sample should emit enough X-ray counts in a reasonable measuring time to

achieve a good signal-to-noise ratio (characteristic X-ray lines at medium energy). The energy of the X-rays should not be too low because of absorption in the sample. The volume emitting X-rays has to be well defined. The amount of X-ray emitted should be independent on the sample position; hence the sample has to be flat (same z-height with respect to the detectors) and no grid bars should influence the amount of X-rays arriving at the detector.

Many groups interested in detector geometry are working with nanoparticles (e.g. (*121, 124, 125*)) to assure that always the same amount of X-ray counts is generated because the volume stays constant. However, the operator cannot precisely control the z-positon of the nanoparticle and the x-y-position is also tied to the availability of a nanoparticle.

We chose a Silicon Nitride Support film by TED Pella (nominal thickness of 15 nm, 0.1 x 0.1 mm window, TED Pella Inc., Redding, USA) and applied an Au:Pd film (80:20, via sputtering, 10 nm thick). The TEM measurements were done immediately after sample preparation.
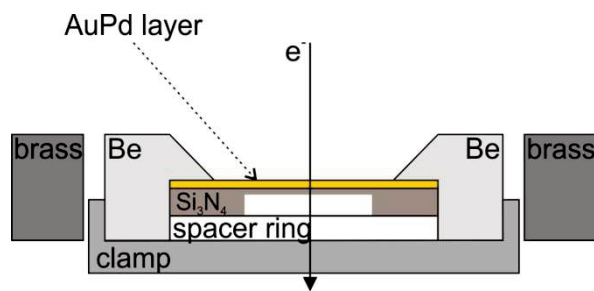

Figure 47: Cross-section through the specimen holder with inserted sample. From bottom to top: clamp, spacer ring, silicon nitride substrate with AuPd layer.

Before mounting the specimen in the sample holder, the holder was ultrasonically cleaned in ethanol twice (technical and p.a.). The holder, the used spacer ring (Al) and the clamp (Al) were further cleaned in a plasma cleaner (oxygen: argon, 30:70) for 10 minutes. Afterwards the sample was mounted in the HiVis holder with the coated side facing downwards. No spacer rings were put in underneath the sample. The sample was fixed in the holder with the spacer ring and the clamp (see Figure 47). The sample was oriented as centered as possible and in a way that each corner of the membrane was facing a detector quadrant (see Figure 46a right).

The measurements were done in STEM mode. The sample was brought to eucentric height. To check the samples flatness the positions in the corner of the silicon nitride window were focused (by changing the z-height at constant defocus values of the condenser lens). To assess the flatness of the sample a plane was calculated from three of the corner points of the
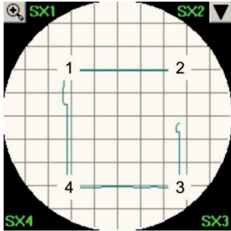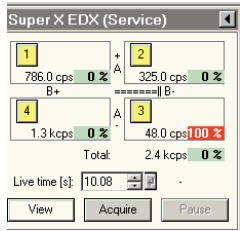
sample and the distance of the fourth corner point to this plane was calculated. This distance was 0.2 μm, so the sample can be considered as sufficiently flat (see Table 8).

All measurements were done at a magnification of 160kx. For the measurements in the center ($x = y = 0$) the z-height remained constant over 155 measurements at z= -220.7 ± 0.5 μm. The position change in x and y was: x= -1.5 ± 1.0 μm and y= 0.1 ± 0.2 μm; so can be considered negligible. The beam current was monitored during all measurements and was constant at around 1 nA (1.06 ± 0.06 nA). Each of the tilt series was approached from the negative side. Hysteresis effects of the stage can be neglected which was confirmed by a tilt series, which approached once from the negative side and once from the positive side without having an effect on the results.

For focusing the magnification was increased to 640kx and the z-height was used to focus the image. The EDX spectra were acquired while the electron beam was scanned over an area of 512x512 pixels with a pixel size of 757 pm which resulted in an area of around 0.15 μm². The EDX spectra were acquired for 30 s (real time) for each detector separately. For Q1 and Q2 a tilt range of -26° to 20° and for Q3 and Q4 of -20° to 32° was measured in 2° steps. These tilt ranges completely covered the shadowing curve from "completely dark" to "fully illuminated". For the positions at x/y = ±350 μm we tilted the specimen from -20° to +20° in 10° steps.

Table 8: Coordinates of the positions at the corner of the silicon nitride window for the AuPd sample. The images indicate the positions in the user interface at the microscope and the position of the EDXS detectors.

[μm]	x	y	z		
1	-474.8	389.8	-224.5		
2	527.5	402.7	-229.5		
3	540.3	-611.0	-214.2		
4	-465.7	-623.7	-209.3		

So finally, we achieved an EDX spectrum for each specimen holder position for each detector separately. The gained spectrum is created by a well-defined sample volume and at a constant electron beam.

4.2.2 CINEMA 4D - simulations

To be able to compare our measurement to simulations, a very precise model of the specimen holder was made by X-ray computed tomography (CT) measurements (shown in Figure 48) by Dr: Bernd Oberdorfer at the Österreichisches Gieserei Institut (ÖGI). The 3D holder model was imported in CINEMA 4D (MAXON Computer GmbH, Friedrichsdorf, Germany), a 3D modelling, animating and rendering program. CINEMA 4D offers a visual approach and allows a simple addressing of certain elements of the modelled system. Position and layout changes of elements of the given system such as detector quadrants or the holder can be modified easily. Furthermore, ray calculations of CINEMA 4D were used.

As this program is not primarily intended to give quantitative results we checked the validity of the results by comparing results obtained by AutoCAD (used in an earlier more basic modelling approach (*131*)) and CINEMA 4D using the same holder model and the same geometrical conditions. As both programs gave exactly the same results CINEMA 4D can be seen as a suitable simulation tool for the proposed purpose.
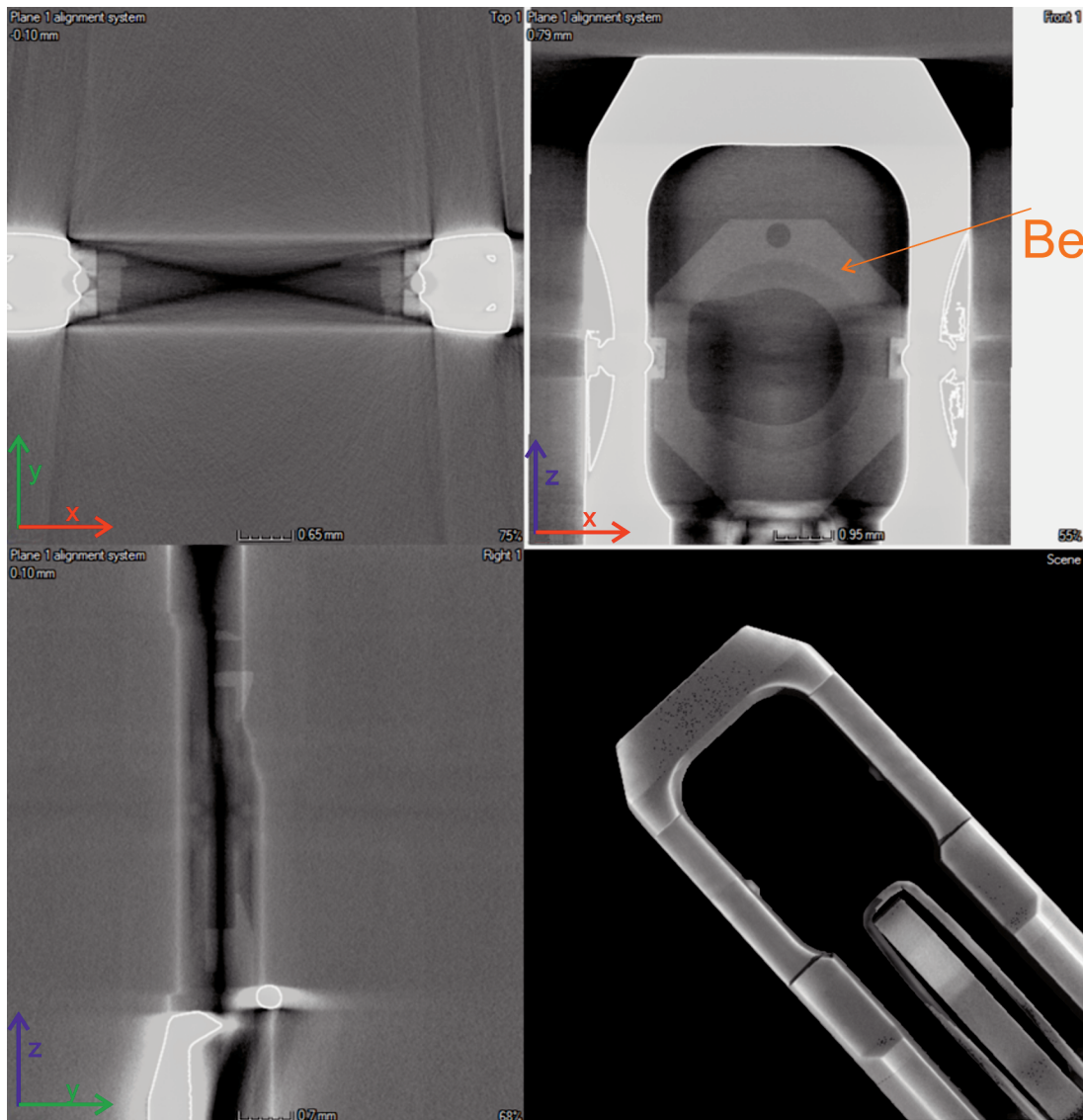
Figure 48: Results of CT measurement. Cross sections through the *y-z*-plane (top left), *z-x*-plane (top right), *z-y*-plane (bottom left) and the 3D model (bottom right).

The CT model of the holder had a voxel size of 0.02 mm³. It was not possible to reconstruct a 3D model of the entire TEM holder out of the CT measurement because the beryllium specimen carrier of the holder did not offer enough contrast for 3D reconstruction. Therefore, only the brass part was directly reconstructed as a 3D model. The beryllium specimen carrier was reconstructed manually in CINEMA 4D with dimensions taken from the CT measurements. The beryllium specimen carrier was still visible in the CT measurements but the contrast was insufficient for automated 3D reconstruction (see Figure 48 top right image). The exact sample position (along the *z*-direction), which is defined by the beryllium specimen carrier, was also taken from the CT measurements. This height defines the intersection point of the electron

beam with the sample and thereby the source of X-rays. In the microscope, this position corresponds to the eucentric height. The β-tilt axis was also defined using the CT holder model corresponding to the center of the rods with which the beryllium part is mounted in the brass part.

Using the CT data a complete model of the LB DT HiVis holder FP6595/20 could be constructed in CINEMA 4D. In Figure 49 the CINEMA 4D simulation setup can be seen. Additionally to the holder, the detector discs are added. The Omniprobe grid, which can be seen Figure 49 was not present during the simulations.

Having the simulation setup at hand a similar experiment, as done practically at the microscope, could be performed. Tilting the holder creates a shadow on the detector disks. The loss in intensity or increase in shadow should correspond to the loss in X-ray intensity during the measurements if the detector positions in the simulation are the same as in the Super-X system.

The tilt series simulations, used to determine the detector positions, were done by a Python based script directly in CINEMA 4D. A text file contained detector positions, defined by the elevation angle ϑ_e and the distance d to the intersection-point. The exact positions in the Cartesian coordinate system were calculated as follows:

$$x = d * cos(\vartheta_e) * cos(\vartheta_A)$$

$$y = d * cos(\vartheta_e) * sin(\vartheta_A) \tag{4.5}$$

$$z = d * sin(\vartheta_e)$$

The azimuth angles (ϑ_A = 45°, 135°, 225°, 315°) and the angle δ between the detector and the optical axis were fixed (δ = -5°). The detectors had a radius of 3.09 mm.

The given start position of the holder tilt (α-tilt), the tilt interval and the number of tilting steps defined the tilt range of the simulation. If a holder offset of $y_{holderposition} \neq 0$ was applied, the z-height of the holder was adjusted at each tilt by $\Delta z = tan(\alpha) * y_{holderposition}$.
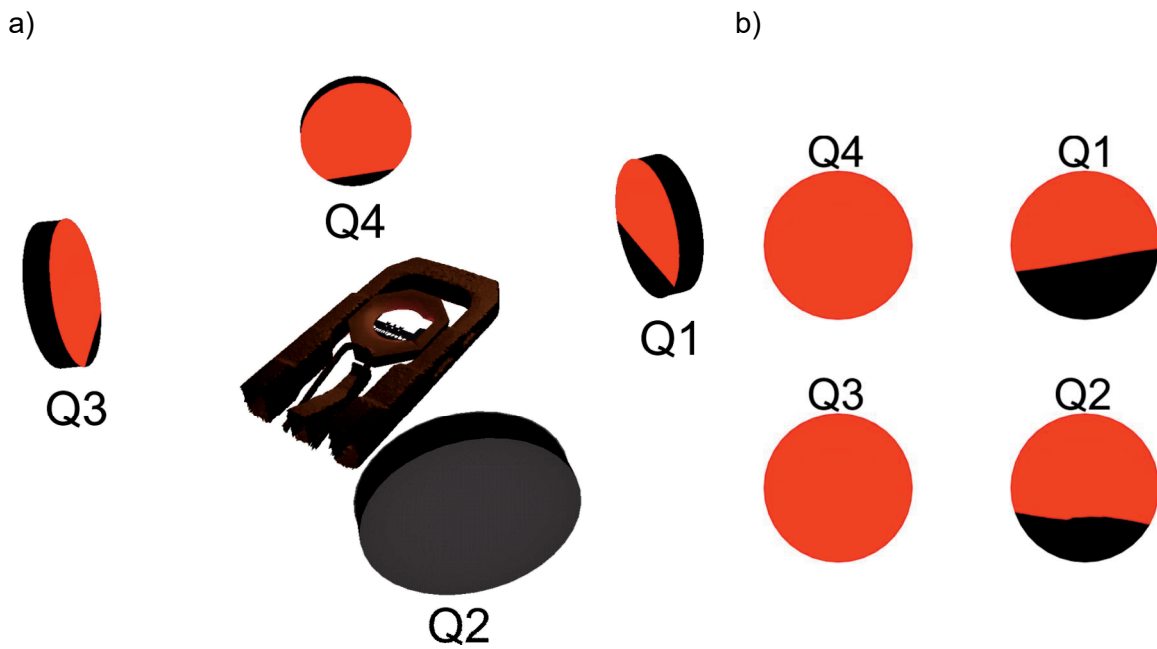
a)   b)

Figure 49: (a) Simulation setup in CINEMA 4D. (b) Shadowing images Q1, Q2, Q3 and Q4 with an applied holder tilt of α = -10° and β = 3 (ϑ_e = 18°).

Finally, a key frame was set at each scene with the holder position (tilt and/or *x, y, z*-position) and the detector position. In the program the beryllium and the brass part were two separate components and therefore simulations with and without the beryllium part could be done. All simulations compared to the Au L measurements are done without the beryllium part and all simulations compared to the Si K measurements were done with the beryllium part as explained later.

A red light source simulated the intersection point of the electron beam with the specimen, or rather the source of the spherical symmetric emission of X-rays. Each detector was faced by a camera in CINEMA 4D. By rendering the images at each set key frame a shadow image of the holder on the detectors was obtained at each holder position (*α*-tilt, *x, y, z*) (see Figure 49b). These shadow images were rendered and evaluated with MATLAB (MATLAB R2014a, MathWorks®, Natick, USA) and thereby converted to an illumination percentage. So finally, for each detector position (defined by the detector distance and the elevation angle) we obtained the illumination percentage dependent on the holder tilt which is called a "shadowing curve".

All other simulations also performed in CINEMA 4D were also script based (compare chapter 4.4 and chapter 4.5). The detector positions were either imported via text file or hard-coded in the script. The *α*- and *β*-tilts were also imported from a text file.

4.3   Determination of detector positions

4.3.1   Data evaluation

As already discussed in chapter 3.9 the intensity determination has a severe influence on the results. Here it is not so critical, because only the change of characteristic X-rays with a changed α-tilt is considered. Nonetheless, the data was evaluated using a top-hat filtering method implemented in DM (2.31) or the window method (gawk, explained in chapter 3.9.1). In case of the energy window method a window of 1.2x FHWM of each peak was defined as signal window and two windows with the same size as background windows. For characteristic low energy X-ray signals, only one background window was defined to avoid the interference with other peaks nearby. The background was linearly interpolated and subtracted from the signal window (for comparison see Table 9).
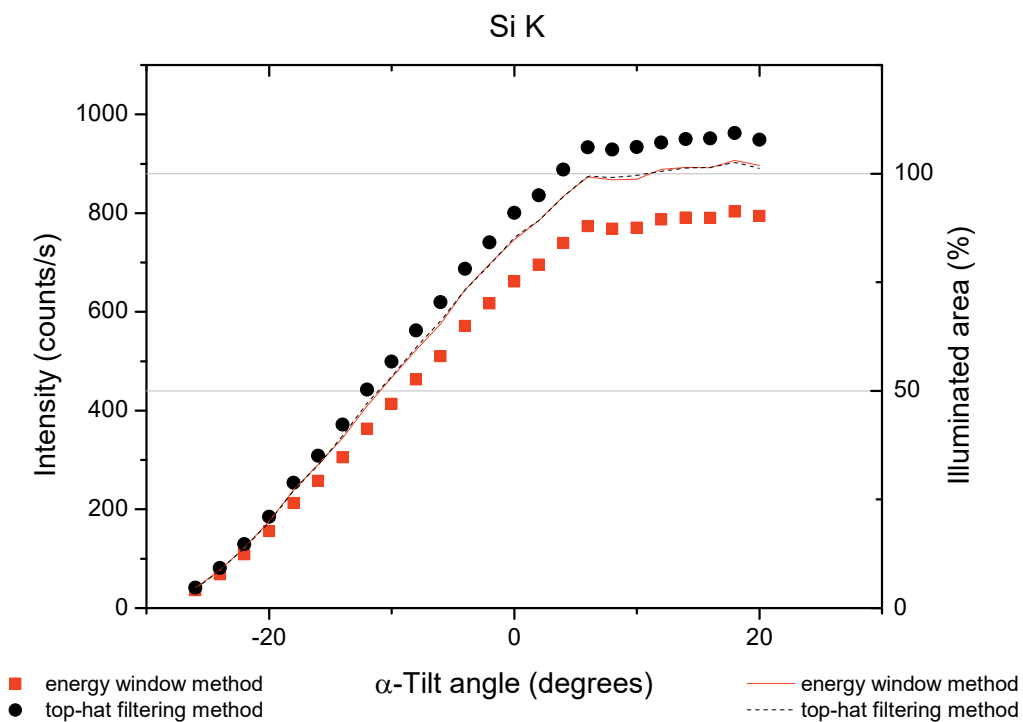

Figure 50: Comparison of intensity determination with a top-hat filtering method and using energy windows. The determined counts per seconds (in symbols) are plotted on the left axis while on the right axis the normalized intensity can be found (lines).

In Figure 50 it can be seen that both methods gave different absolute counts. If the intensities were normalized both curves have a very similar shape. The normalization in this case was

done as follows: all values greater than 90% of the maximum intensity were averaged in order to yield a factor for normalization. Even though there is a significant difference between the two approaches (as the energy window method only integrates the intensities up to 1.2 x FWHM, whereas the top-hat filtering measures the entire peak.), the overall curve shape after normalization stays the same. It was decided to further evaluate all spectra using the energy window method. The energy window method does not rely on any fitting routines, which could introduce errors if the tilt of the sample increases and the signal to noise ratio of the characteristic X-ray peaks worsens. All spectra from one series are evaluated using exactly the same energy windows.

The measured X-ray intensities were converted to counts per second using the live time. In a next step the values were corrected for the increased path length of the electrons through the sample with increasing specimen tilt (*dt*) with the cosine as shown in Figure 51.
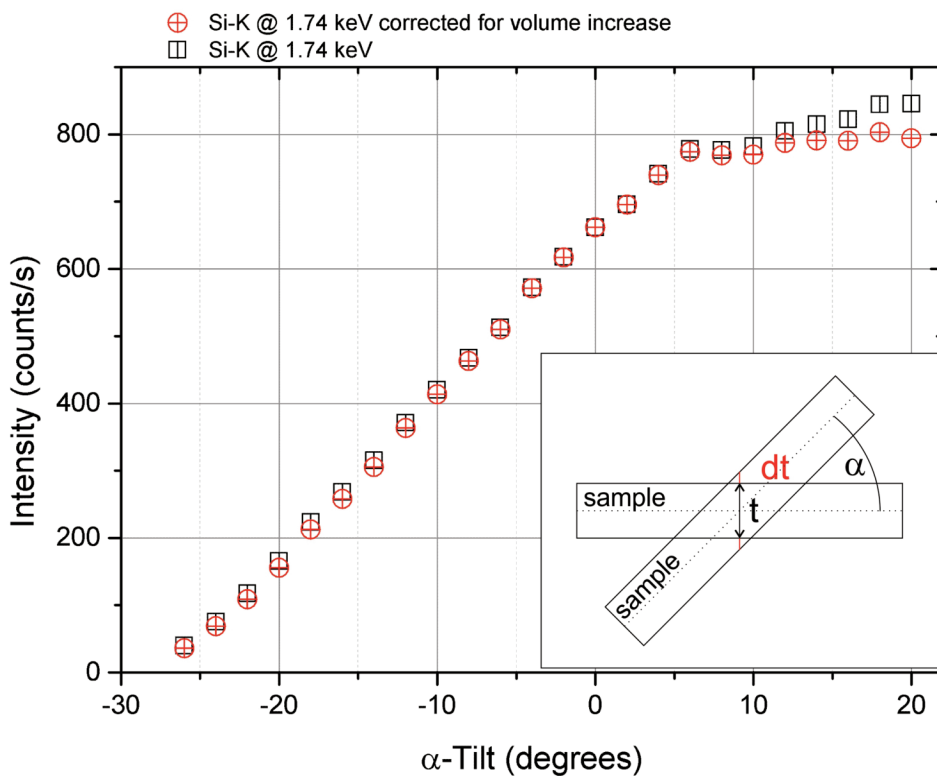

Figure 51: Effect of correction for volume increase due to sample tilt.

Figure 52a depicts an example of all characteristic X-ray energies evaluated for one series. The intensities were already corrected for the increased path length through the specimen. In Table 9 the parameters used for the determination of the peak intensities are shown. Figure

52b shows the Au L signal measured with all four detectors as well as the summed intensity of all four detectors. The highest intensity is reached at an *α*-tilt angle close to 0°. It can be seen that Q1 and Q4 are reaching the maximum intensity of Au L around 5° earlier than Q2 and Q3.

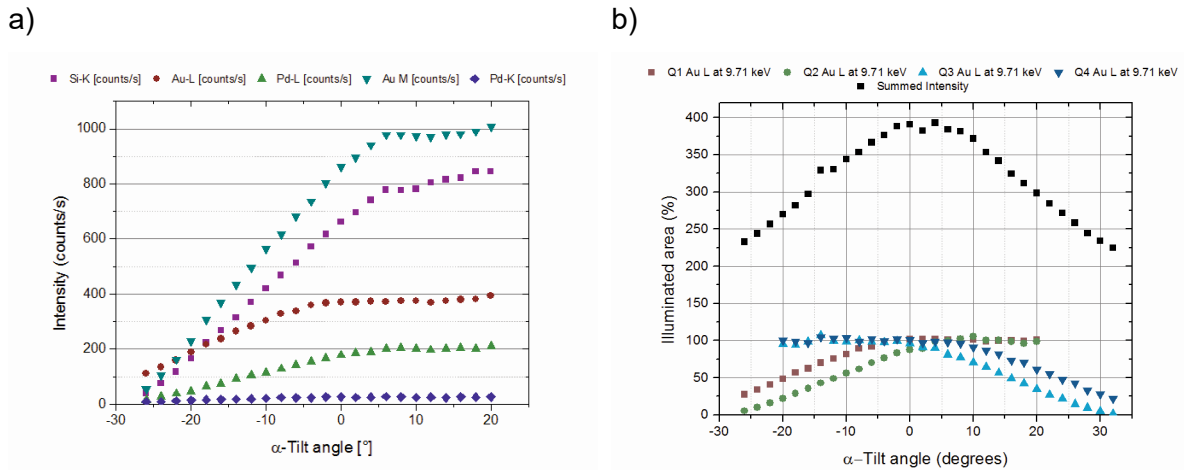a)   b)

Figure 52: a) All evaluated characteristic X-ray Signals from one series using the parameters in Table 9 for Q1. The signals are corrected for the increased path length through the sample. b) Au L for all four quadrants as well as the summed and normalized intensity.

Table 9: Energies in keV of signal- and background- windows for the evaluation of one tilt series.

(keV)	Center	FWHM	Signal		Background left		Background right	
Si	1.74	0.10	1.68 - 1.80		1.28 - 1.40			
Au M	2.15	0.15	2.06 - 2.24		0.76 - 0.94		3.36 - 3.54	
Pd L $_{α1}$	2.84	0.11	2.77 - 2.91		1.22 - 1.36		4.32 - 4.46	
Au L $_{α1}$	9.70	0.19	9.59 - 9.81		5.09 - 5.31		14.09 - 14.31	
Pd K	21.10	0.33	20.90 - 21.30		19.70 - 20.10		22.10 - 22.50	

For further characterization mainly the Au L line at 9.71 keV was used. The absorption of the Au L line in the sample and the beryllium part of the holder will be negligible. Contrary, the energy is still low enough to ensure good energy detection efficiency by the SDD and a

satisfying counting statistics can be achieved in a reasonable measuring time. Using the model in CINEMA 4D different detector positions were simulated (changing the detector distance and the elevation angle) without a beryllium part, because we assumed the absorption of the Au L line in the beryllium part to be negligible.

As already described in chapter 4.2, the simulation provided the illumination percentage over specimen α-tilt. These shadowing curves from 0% to 100% had to be compared to the experimentally measured intensities. To be able to compare the simulations to real experiments the measured intensities had to be normalized. The normalization strongly influences the experimentally measured shadowing curves. Several approaches were evaluated how to normalize the measured shadowing curves. In Table 10 the two approaches used in this work are shown. The iterative approach was used to determine the detector positions and is explained in the following section. The other approach, were we used all values above 90% of the maximum, was used to compare two measurements (e.g. in Figure 54), if no iterative fitting was performed. Table 10 shows that there are no big differences between the two approaches, but the iterative fitting approach is less dependent on outliers because the whole shadowing curve is considered.

Table 10: Normalization values determined iteratively or by calculating the average value of all values >0.9*maximum intensity.

	iterative	10% smaller than maximum	iterative	10% smaller than maximum
	Si-K	Si-K	Au-L	Au-L
Q1	784	780	368	365
Q2	684	686	341	339
Q3	687	691	331	337
Q4	829	820	379	377

The iterative normalization was done by minimizing χ^2 in comparison to the experiment. So each simulated shadowing curve had its separately determined normalization value.

$$\chi^2 = \sum_{i=1}^{N} \left(\frac{M_i - f(\alpha_i)}{\Delta M_i} \right)^2$$

(4.6)

M_i is the normalized X-ray intensity of the experiments. $f(\alpha_i)$ the simulated illumination fraction and ΔM_i is the error of the measured intensity (Poisson error). χ^2 was also used to assess the agreement of the simulated detector position to the real situation in the microscope.

Figure 53 depicts an example of detector Q1, where simulated shadowing curves for different detector positions are compared to the measured curve using the Au L line. As a measure for the agreement between simulated and measured data a χ^2 value is used (see above). In Figure 53a all positions simulated for Q1, detector distances and elevation angles, are shown. Detector distances and elevation angles were simulated with a step size of 0.25 mm and 0.25°. The colour code refers to the χ^2 of each simulation. It can clearly be seen that the point cloud for χ^2 exhibits a minimum. This result gets even clearer if Figure 53b, c, and d are considered. Figure 53b and Figure 53c show that a minimum in detector distance and elevation angle can be found respectively. To be independent of the chosen step size of detector distance/ elevation angles a polynomial fit of fifth order to the point cloud was made. In Figure 53d the fitting function is plotted. The minimum of this surface was taken as the real detector position.
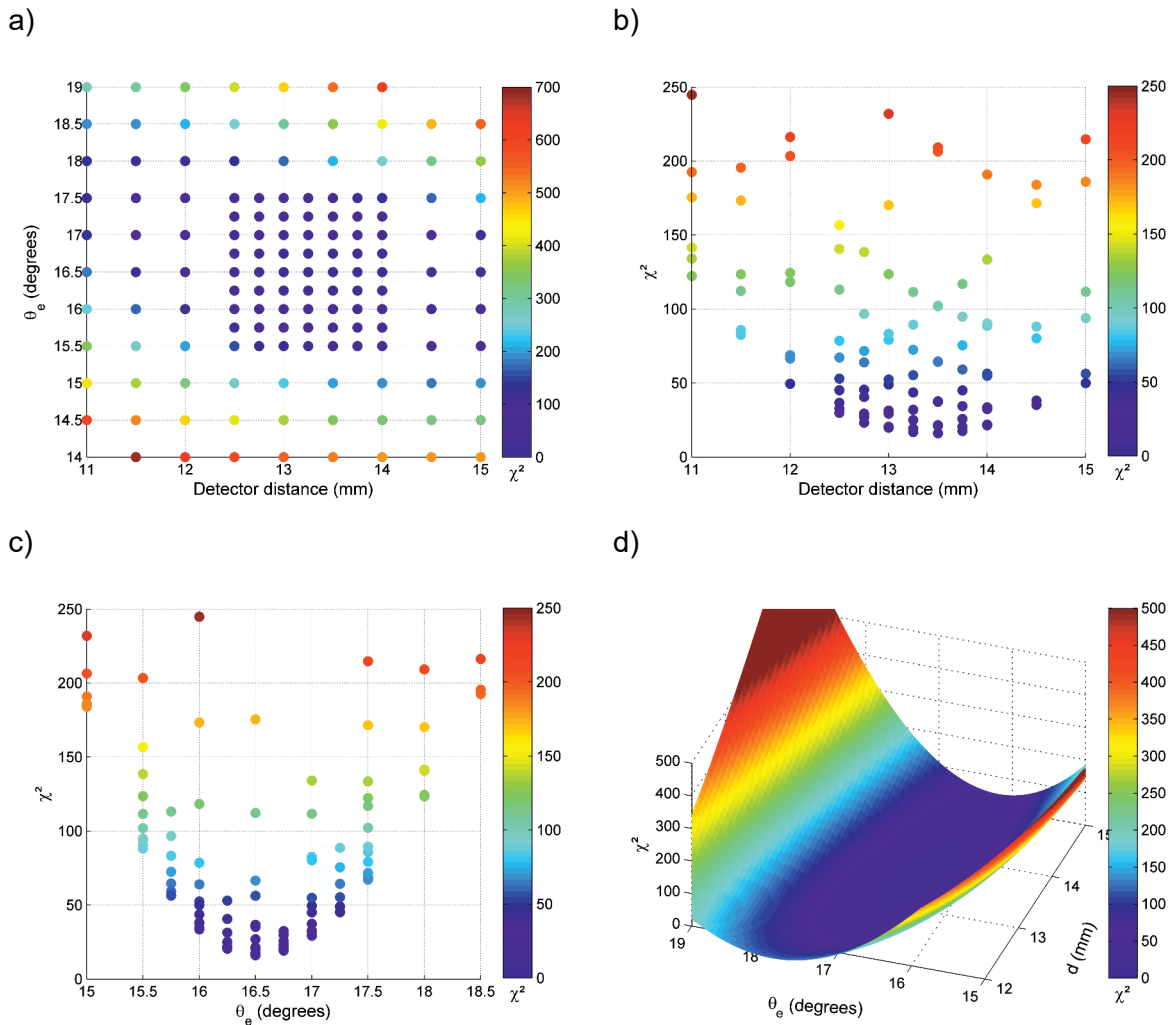
Figure 53: Simulation results for Q1 compared to Au L measurements. The colour corresponds in each plot to the value of χ^2. (a) shows the region over which the detector distance d and the elevation angle θ_e were varied. Both, the detector distance and the elevation angle exhibit a minimum of χ^2 (b, c). A polynomial of fifth order is fitted to the data points and plotted in (d).

Using this approach the exact detector position could be determined for all four detectors (see Table 11). The errors given in Table 11 are taken from an error estimation discussed in section 4.3.3.

Table 11: Experimentally determined detector positions for all 4 detector quadrants of the Super-X system (A_{det} = 30 mm^2)

	ϑ_e	Detector distance
	(degrees)	(mm)
Q1	16.5 ± 0.2	13.4 ± 0.3
Q2	15.9 ± 0.3	13.3 ± 0.6
Q3	19.0 ± 0.2	13.8 ± 0.6
Q4	19.6 ± 0.5	12.5 ± 1.0

In all the following simulations the detectors were placed at these positions if not noted otherwise.

4.3.2 Beryllium specimen carrier

It is state of the art that analytical TEM holders, especially holders designed for EDXS, have components made out of beryllium. This is to reduce unwanted X-ray signal that might interfere with the analysis. In conventional EDSX systems, with only one detector, it is common practice that the holder is tilted toward the detector to avoid shadowing problems. Due to the increased complexity of todays' detector systems, e.g. the Super-X system with its four detectors, this simple workaround of tilting toward the detector is not possible anymore; tilting toward one detector will inevitably create shadowing for other detectors. During our studies we made the observation that the shadow which the holder casts on the detector active area seems to be dependent on the emitted X-ray energy. Furthermore, this effect was far more severe for the two detectors in front of the holder; Q1 and Q4; than those in the back of the holder; Q2 and Q3. It can be excluded that this effect arose from e.g. beam current fluctuations or concentration changes in the sample. This was proven by Figure 54 which shows the shadowing behaviour of the Au M and the Au L line extracted from the same measurement. The Au L at 9.71 keV reached a 100% illumination of Q1 about 5° specimen holder tilt earlier than the Au M line at 2.12 keV. This trend of an energy dependent shadowing behaviour was reproducible over all evaluated X-ray line intensities (Si K @ 1.74 keV, Au M @ 2.12 keV, Pd L @ 2.84 keV, Au L @ 9.71 keV and Pd K @ 21.18 keV). A Cr sample (sputtered on a silicon nitride film) was also measured and the Cr K @ 5.41 also corresponds to the observed energy dependency.
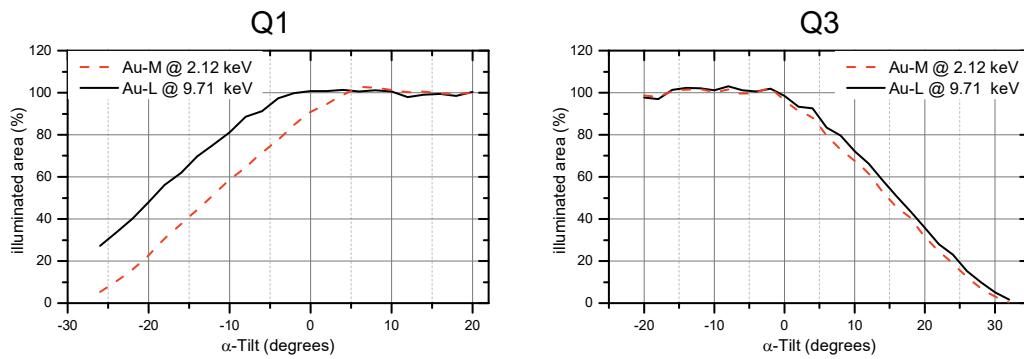
Figure 54: Extracted and normalized x-ray line intensities for Au L at 2.12 keV and Au M at 9.71 keV. Left: for detector Q1 in the front of the holder; Right: detector Q3 in the back of the holder.

In Figure 55 a 45° cross section through the holder model is shown. Due to the geometrical conditions this cross section extends from Q1 to Q3 (equivalent Q2 to Q4). It can clearly be seen that high energy X-rays (not absorbed by the beryllium specimen carrier) cast a different shadow on Q1 as low energy X-rays would (absorbed by the beryllium specimen carrier). The same effect can be found in the direction of Q3 but far less pronounced.
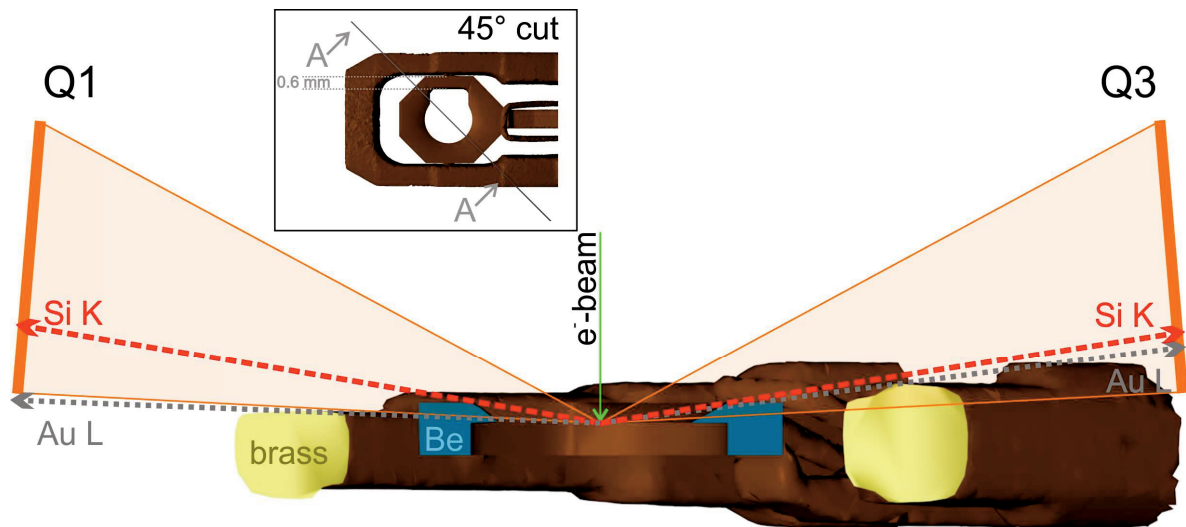
Figure 55: The inset shows the position of the section (A-A). In orange the position of Q1 and Q3 are schematically drawn. The 45° cross section through the holder shows a difference in the direction of Q1 and Q3. In blue the cut through the beryllium specimen carrier is shown. The yellow cross section region corresponds to the brass part of the holder.

Considering the results so far, the exact positions of all four detector quadrants in our system were determined. We stick to the assumption that the Au L line at 9.71 keV is not influenced by the beryllium specimen carrier of the holder. Due to the energy dependency of the shadowing curve, we chose the Si K line as the lowest energy evaluable line in our spectra to be considered fully absorbed by the beryllium specimen carrier (99.994% are absorbed in beryllium with a thickness of 0.5 mm). In the CINEMA 4D model the beryllium specimen carrier was handled as a separate element, therefore it was possible to show and hide it during simulation. So a further simulation was done with the beryllium part and compared to the Si K line. The detectors were put to the positions determined before. The result for Q1 can be seen in Figure 56. Our assumption of the fully absorbed Si K line and the fully transmitted Au L line might be rough but valid considering the agreement of the simulation with the measurements. In Figure 56 the normalized intensities for the Au L and Si K line are plotted as well as the corresponding simulations. The detector (Q1) was set to the position determined earlier (16.5° 13.4 mm) and one simulation without the beryllium part (green line) and one with the beryllium part (blue intermittent line) was made. This finding supports the accuracy of the determined detector positions as well as the influence of the beryllium part.
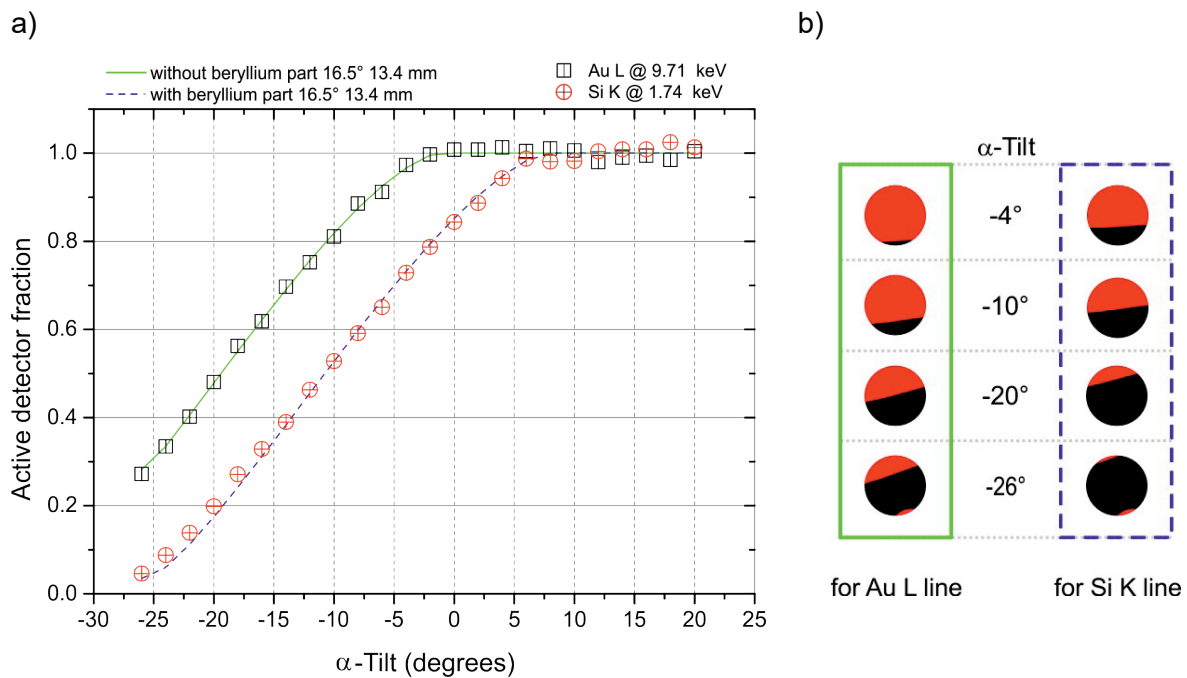
a)

b)

Figure 56: Measured line intensities for Au L and Si K (normalized) (dots) and simulation with hidden beryllium specimen carrier and shown beryllium specimen carrier (lines).

In Table 12 the deviations of the actual measurements compared to the simulations, expressed by χ^2 values (equation (4.6)) are listed. Tilt angles up to $\alpha = \pm 26°$ are considered. It is obvious that the deviations for Q1 and Q2 are smaller than for Q3 and Q4. This is probably due to the following reasons. The beryllium part has a window at the side of Q1 and Q2 and (see Figure 48 upper right image). Therefore, the beryllium volume, the X-rays have to pass, is overall smaller than the volume in the direction of Q3 and Q4. So, the assumption that the Au L line is not absorbed in the beryllium might not be as suitable as it is in the direction of Q1 and Q2. Moreover, it could also be the case that the assumed azimuthal angles for Q3 and Q4 are slightly off. The simulations without beryllium also seem to fit better to the measurements which can lead to the assumption that the total assumed total absorption of the Si K line is not entirely valid.

Table 12: Deviation between the measurements and the simulations expressed by χ^2.

	χ^2	
	with beryllium	without beryllium
Q1	1.71	0.23
Q2	1.14	0.84
Q3	3.15	0.32
Q4	4.66	0.99

For a further validation of the detector positions we acquired tilt series at sample holder positions away from the optical axis ($x, y = \pm350$ µm). These tilt series were also simulated with and without the beryllium specimen carrier and compared to the measurements. The results for Q1 are reported in Figure 57.
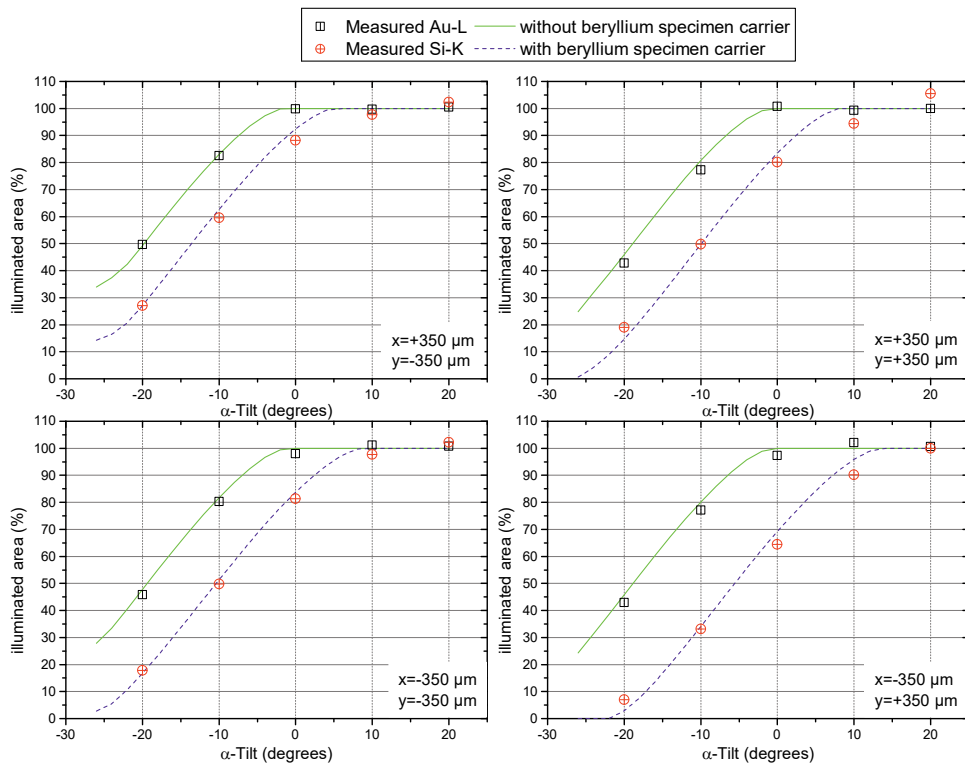
Figure 57: Each diagram contains the measured and normalized intensities for Au L and Si K measured with Q1 as well as the simulated values. Top left: *x* = 350 μm, *y* = -350 μm, top right: *x* = 350 μm, *y* = 350 μm, bottom left: *x* = -350 μm, *y* = -350 μm, bottom right: *x* = -350 μm, *y* = 350 μm.

These results again verify the identified detector positions and the assumption that the absorption behaviour within the beryllium specimen carrier is valid. The χ^2 values for all detectors at positions of ±350 μm are listed in Table 13. The deviations for Q1 and Q2 are lower than for Q3 and Q4; especially as far as the agreement of the Si K line with the simulation are concerned. So, far mostly the shadowing curves as well as the simulations for Q1 are shown. But the measurements and the simulation were also done for all other detectors and showed similar behaviour.

Table 13: χ^2 of offset positons given in x and y for Au L (without beryllium) and Si K (with beryllium)

	χ^2							
	Q1		Q2		Q3		Q4	
	Au L	Si K	Au L	Si K	Au L	Si K	Au L	Si K
-350μm -350μm	0.14	0.34	0.11	1.01	0.03	1.53	0.16	2.67
-350μm +350μm	0.35	2.04	0.27	1.39	0.10	3.02	0.09	1.48
+350μm -350μm	0.01	0.64	0.13	0.32	0.04	3.62	0.05	0.91
+350μm +350μm	0.32	1.78	0.14	2.00	0.37	1.20	0.14	6.39

So far, always the Au L line and simulations without the beryllium part were used to determine the detector positions. If the optimum detector position was found the beryllium part was inserted in the simulations and this simulated shadowing curve was compared with the Si K measurement.

For Q1 and Q4 the detector positions were also determined using the Si K measurement and simulation with the beryllium part inserted. The thereby determined positions can be found in Table 14. The determined elevation angles and distances are very close to those found before. Changing the elevation angle has the effect of a parallel shift of the whole shadowing curve. A change in detector distance has an effect on the slope of the curve. It seems that for the detector positions determined with the Si K line a slightly higher detector angle and a shorter distance are found.

Table 14: Detector positions for Q1 and Q4 determined either by simulations without the beryllium specimen carrier and compared to the Au L signal or by simulations with the beryllium specimen carrier included in the simulations and compared to the Si K measurements.

	Au L - without beryllium		Si K - with beryllium	
	ϑ_e	Detector distance	ϑ_e	Detector distance
	(degrees)	(mm)	(degrees)	(mm)
Q1	16.5	13.4	16.6	12.7
Q4	19.6	12.5	20.2	11.3

If the two shadowing curves gained at both position listed in Table 14 (either for Q1 or Q4) are compared the differences are negligible.

4.3.3   Error estimation of detector position

To estimate the error of the determined detector positions it was decided to calculate the area wherein the χ^2 increases by 10% (white circles in Figure 58). It reflects the fact that the slope around the minimum of the surface in direction of the elevation angle is steeper. Whereas, a little change in detector distance has not such a severe effect on the agreement with the experimentally acquired shadowing curve; the slope close to the minimum is lower.
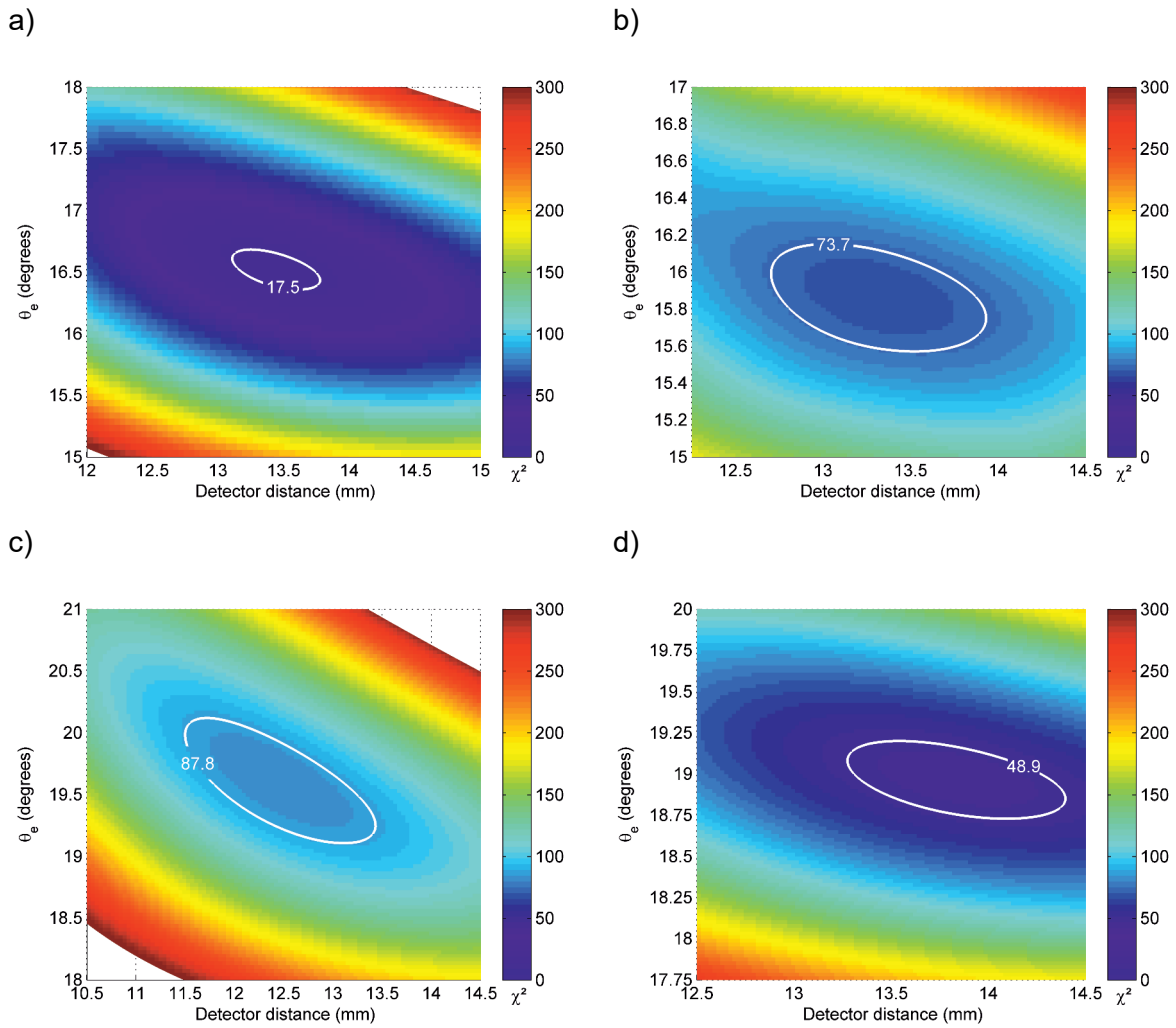
a)

b)

c)

d)

Figure 58: A polynomial of fifth order was fitted to the simulated data points. This surface is plotted for Q1 (a), Q2 (b), Q4 (c) and Q3 (d). The colour-code refers to the calculated χ^2. In each plot the white line marks the area in which χ^2 increases by 10% of its minimum (the number corresponds to the value $\chi^2+10\%$).

Table 15 sums up the values plotted in Figure 58. The highest deviation in detector distance and elevation angle gained by increasing χ^2 by 10% is used as the estimated error.

Table 15: Error estimation of determined detector positions.

	[degree]	[mm]
Q1	16.53 ± 0.15	13.43 ± 0.32
Q1 (Si)	16.55 ± 0.14	12.70 ± 0.30
Q2	15.85 ± 0.30	13.31 ± 0.61
Q3	18.95 ± 0.23	13.83 ± 0.55
Q4	19.58 ± 0.51	12.50 ± 0.99
Q4 (Si)	20.18 ± 0.33	11.27 ± 0.57

Another aspect to be considered is that the detectors are mounted pairwise (Q1/Q2 and Q3/Q4) on mounting units. The experimentally determined detector distance for Q1 and Q2 is approximately equal, suggesting a precise mounting. The distance of Q3 and Q4 is different, suggesting a tilt of the mounting unit by 6°. This tilt brings Q4 closer to the optical axis and Q3 farther away. The azimuthal angles for Q3 and Q4 are 134° and 40°, respectively.

Furthermore, it has to be stated that we relied on the displayed tilt values. The calibration of zero tilt point of the goniometer was not verified.

4.3.4   Detector tilt

Generally, it is often assumed that the detector normal points to the intersection point of the electron beam with the sample (orange detector in Figure 59). However, the detectors mounted in the Super-X system are not mounted like this, but are tilted 5° away from the vertical axes (according to the manufacturer) as is shown schematically in Figure 59 (blue detector). If the spherical symmetric distribution of the X-rays is considered, this unfavourable arrangement leads to an effective reduction of collection angle. The amount of X-rays per detector area is different comparing the upper and the lower part of the detector. It would be equal if the detector would follow the shape of a sphere but as the detector is a flat disk to lower part detects more X-rays per area as the upper part does, so the shadow cast by the holder has a different effect on the detected X-ray signal (see inset in Figure 59). A closer consideration of the aspect is made in (*117*). To asses this effect in our simulations we corrected one simulation. Therefore, an image was created (projection of the sphere on the detector plane) with which the simulated images were multiplied. In Figure 59 the image used for the correction as well

as the effect of the correction on the shadowing curve is shown. It only has a minor effect on the overall agreement of the simulation with the measurements.
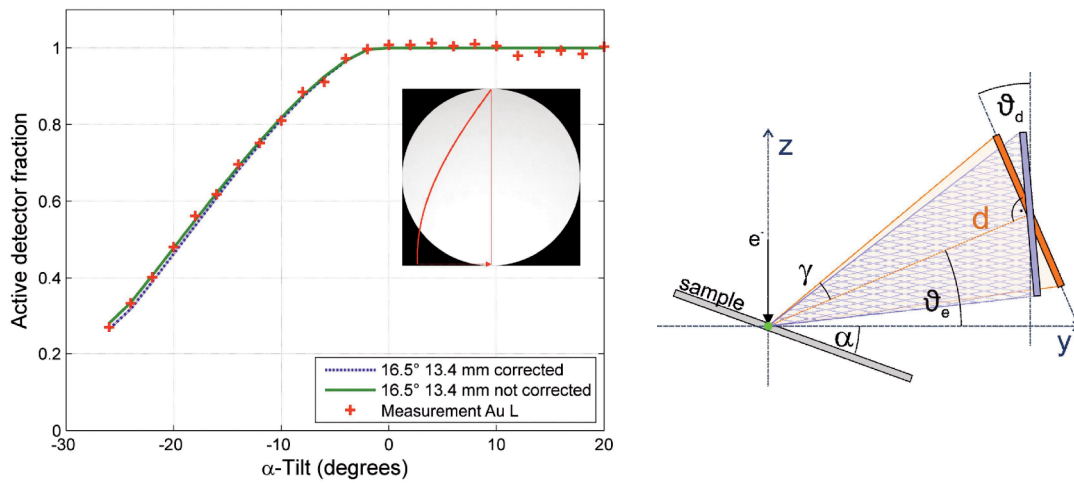

Figure 59: Effect of the correction for the detector tilt for Q1. The dotted line shows the corrected simulation (blue) the straight line (green) the not corrected. The Au L measurement is also shown (red crosses). The insert shows the image which was used for the correction.

Moreover, the 5° detector tilt was also varied for Q1. This was done because at the beginning it was not clear whether or not this value is correct. A variation of the detector tilt was done between ϑ_d = 5°- 13°. Changing this angle has a negligible influence on the determined detector positions as also (*127*) confirms.

4.3.5   Area of detectors

So far we determined the detector positions of all four detectors. The simulations provide the opening cones of the detectors (corresponding to the solid angles), which provide detector distances when the detector area is known. We used the nominal value of 30 mm^2 for the detector areas and computed the solid angles using the obtained distances. According to (*117*) the real active detector area is probably smaller due to the collimator of the detector. For the Super-X system an active area of 26.4 mm^2 is suggested. This change in detector area does not influence the determined elevation angles but the detector distances.

Therefore, the so far determined detector distances were recalculated. This was done by first calculating the solid angle following (*118*) and then by changing the area of the detector and recalculating the detector distances. This new detector distances with the decrease detector area was used for a further simulation (results are depicted in Figure 60).
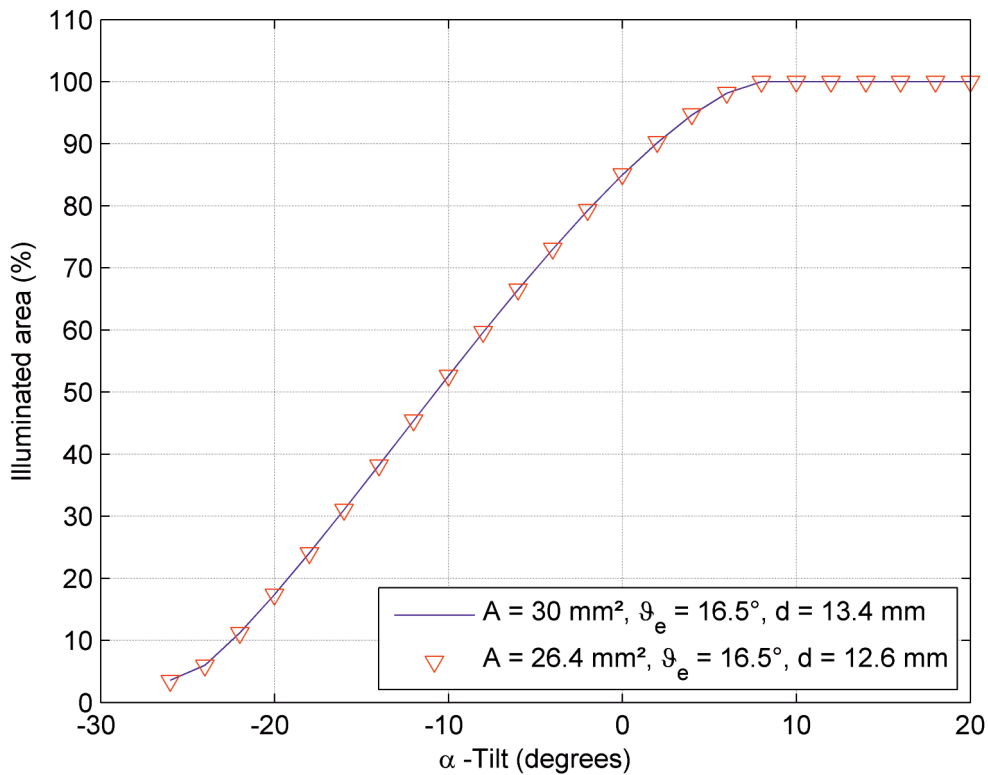
Figure 60: Simulations with Q1 at different positions and using different detector areas.

The calculated detector distances for a decreased detector area can be found in Table 16. The manufacturer indicates a detector position of 18° and 12.6 mm and a maximum total solid angle of 0.7 sr (for all four quadrants!). Assuming a detector area of 26.4 mm² (*117*) our results are close to the manufacturers values. The sum of all measured solid angles leads to an overall maximum solid angle of (0.64 ± 0.06) sr.

Table 16: Experimentally determined detector positions for all 4 detectors of the Super-X system and calculated solid angles according to (*118*).

	Elevation angle ϑ_e			Detector distance d (A_{det} = 26.4 mm^2)			Solid angle		
	(degrees)			(mm)			(sr)		
Q1	16.5	±	0.2	12.6	±	0.3	0.157	±	0.007
Q2	15.9	±	0.3	12.5	±	0.5	0.16	±	0.01
Q3	19.0	±	0.2	13.0	±	0.5	0.15	±	0.01
Q4	19.6	±	0.5	11.8	±	0.9	0.18	±	0.03

4.4 A second approach for detector-position determination

A second approach was also used to determine the detector positions. This was only done for detector Q1. Therefore, in the simulations the specimen holder was placed to a fixed specimen tilt position and the detector position was varied. Holder tilts for -10°, -16°, -20° and -24° were simulated at different detector positions (elevation angle 15°-25°, detector distance 7-17 mm); so for each detector position only one image was rendered. The normalization of the experimental measurements was done using the average of all values 10% smaller than the maximum illumination value (in counts); for Au L: 365 and for Si K: 780 (compare Table 10). The determined illuminated area for the corresponding specimen holder tilt can be found in Table 17.

The simulations in CINEMA 4D were done with and without the beryllium part of the holder. Similar to the previous approach, the simulations with the beryllium part were compared to the Si K measurements and the simulations without the beryllium part to the Au L measurements. The simulated images were converted to illumination percentages as done before. So, each holder position gave a set of illumination data. These data sets were compared with different thresholds. The idea was that the real detector position must be present in all the data sets.

Table 17: Measured illumination percentage of the Q1 at each *α*-tilt position of the holder for the Si K and the Au L signal.

| *α*-tilt (degrees)	Relative intensity (%)	
	Si K	Au L
-10	53.1	81.8
-16	33.1	62.4
-20	20.0	48.5
-24	8.8	33.7

In Figure 61 a graphical representation of the results can be found. The different symbols correspond to different holder tilts. The symbols are shown if the determined illumination percentage lies in the chosen range of ±1% or ±2%) of the experimentally determined illuminated area for the corresponding X-ray line. For example in case of Au L 25 values fulfil the condition that they do not differ more than 2% of the experimentally determined illumination. The detector positions which appear in all four holder tilts are marked by the red area in the graphs.

Au L, simulation without beryllium part:

a)
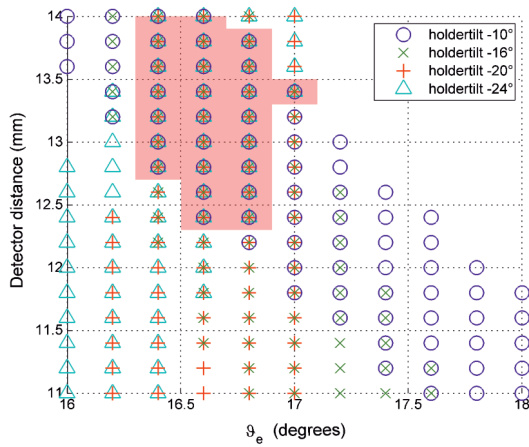
b)
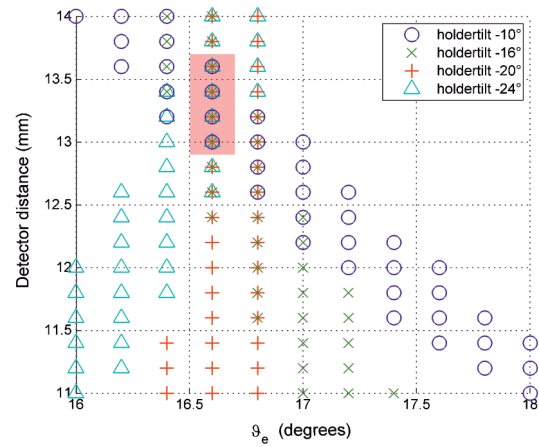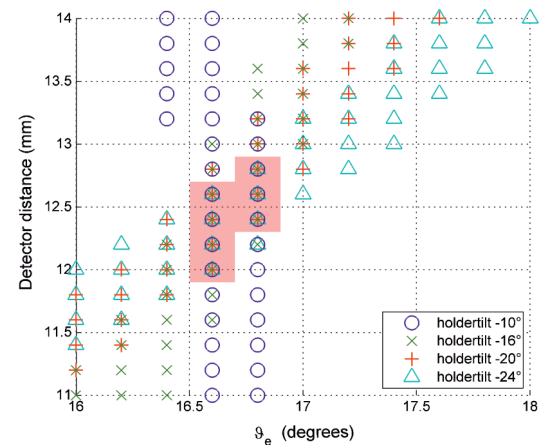
Si K, simulation with beryllium part:

c)
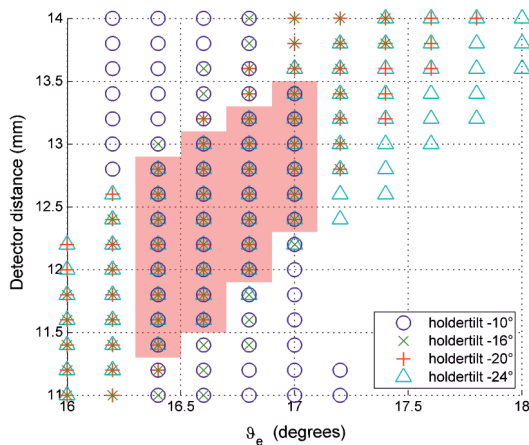
d)

Figure 61: All detector positions (for Q1, detector distance versus elevation angle) at fixed specimen holder tilt positions (-10°, -16°, -20°, -24°) are plotted if they did not differ more than ±2% (a,c) and ±1% (b,c) of the experimentally measured illumination. In a) and b) the comparison to the Au L measurements and in c) and d) to the Si K measurements, are shown.

The detector positions deviating less than 1% from the Au L measurement have an elevation angle of 16.6° and a detector distance ranging from 13.0 mm – 13.6 mm. Considering 1% deviation between the simulations with the beryllium part inserted and the Si K measurement gives a detector position range of 16.6° - 16.8° and 12.0 mm -12.8 mm.

This second approach is independent of the agreement of the whole shadowing curve. Also the normalization of the measured values is done differently. Nevertheless, the results are

similar to the other approach within assumed errors (compare Table 15 which shows the results for a detector area of 30 mm² which was also assumed for this experiment).

4.5   Effect of geometry on detected X-ray signal

The simulation setup can be used to estimate the influence of shadowing at any holder position and specimen tilt because we determined the positions of all four detectors of our Super-X system. Xu et al. (*128*) previously investigated the influence of the *α*- and *β*-specimen holder tilt and *x-y* position variation; using the Al:Ni ratio (Al K @1.49 keV and Ni K @7.47 keV) as an example. We present a more general statement. We assume a full X-ray absorption in the beryllium specimen carrier (X-ray energies below ~2 keV) and no absorption in the beryllium specimen carrier (X-ray energies above ~6 keV) to estimate the maximum systematic error of the quantitative results. Therefore, all simulations with the beryllium specimen carrier correspond to the shadow low energy X-rays would cast and simulations without the beryllium specimen carrier corresponds to shadows casted by higher energy X-rays. We performed simulations varying the *x*-y positions (chapter 4.5.1) and the *α*- and *β*-specimen holder tilt (chapter 4.5.2). Moreover, in both cases a shift in *z*-height is also discussed. This shift is rather important even when the eucentric height is properly adjusted. The microscope defines the point of the eucentric height. Therefore, the position of the X-ray generation is a fixed position in the microscope given by the intersection point of the electron beam with the sample (positioned at the eucentric height). Also the position of the EDX detector in respect to the point of X-ray generation is fixed. The only aspect that can change is the position of the specimen in the specimen holder. This can easily be the case due to the different nature or shape of the specimen (flatness, bending, ion milled samples, etc.). For instance a slight bending of a FIB support grid because of tweezer manipulation may change the specimens' position inside the sample holder by more than 100 µm. Also due to the usage of spacer rings, inserted prior to specimen insertion. These effects change the relative position of the point of X-ray generation with respect to the specimen holder. Adjusting the eucentric height will inevitably result in a different position of the specimen holder with respect to the EDX detectors. If the specimen is mounted deeper in the holder the specimen holder inside the microscope needs to be shifted upwards (with respect to the EDX detectors) to work at the eucentric height. Therefore, it strongly effects the shadowing of the detectors and the influence of the beryllium specimen carrier.

Therefore, in addition to movements of the specimen holder in the *x* and *y* directions and *α* and *β* tilt, movements in the *z* direction must also be considered.

4.5.1   *x-y-z* position of holder

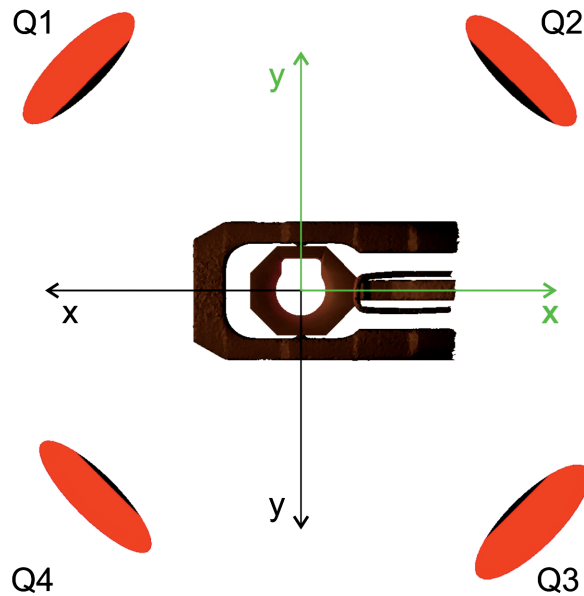In Figure 62 the holder at $x = y = z = 0$ is shown.

Figure 62: Top view of the holder model with the beryllium part inserted. The detector quadrants are positioned at the before determined positions. The point of X-ray generation, hence the simulated intersection of the electron beam with the sample is at $x = y = 0$. Green coordinate axis corresponds to the positions a TEM user sees. The black coordinate axis represents the actual holder movement.

One has to be aware of the fact that the movement of the holder is in the opposite direction as the coordinates of the specimen, which the TEM user sees on the screen. This is because the holder is moving and the beam stays stationary. In all the following figures always the user coordinates are given, corresponding to the green coordinates in Figure 62.

In a simulation the holder position was varied from $x = y = 950$ µm to $x = y = -950$ µm in 50 µm steps. At each position the illumination of each detector was calculated. In Figure 63 holder positions of ±750 µm are shown. The red cross marks the point of X-ray generation; hence the intersection point of the electron beam with the sample.

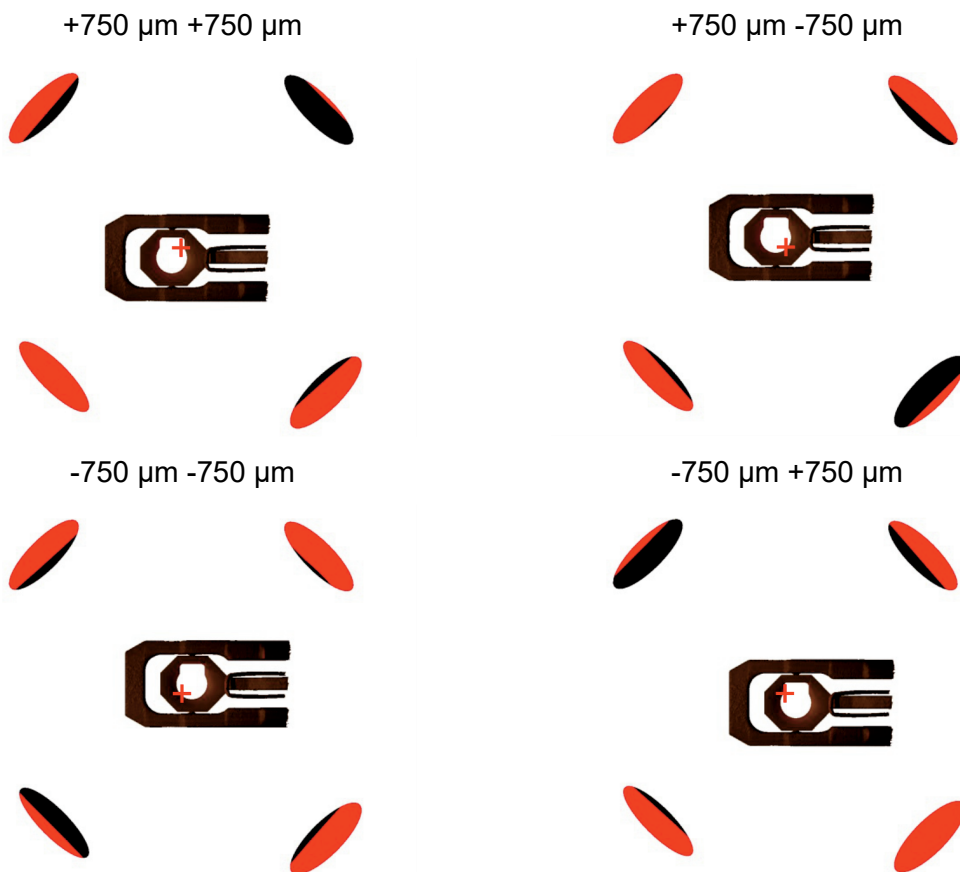+750 µm +750 µm   +750 µm -750 µm

-750 µm -750 µm   -750 µm +750 µm

Figure 63: Top left *x* = *y* = 750 µm, top right *x* = +750 µm *y* = -750 µm, bottom left
***x* = *y* = -750 µm, bottom right *x* = -750 µm *y* = +750 µm. The red cross marks**
position of X-ray generation.

As a result of these simulations the illumination of each detector at each holder position was obtained. For a better illustration the discrete values were linearly interpolated using a MATLAB function (scatteredInterpolant). In Figure 64 all four detectors are shown. As expected, the illumination decreases as the holder moves away from the corresponding detector and hence the beryllium part gets closer to the point of X-ray generation. The abrupt decrease of illumination at positions in the range of ±950 µm is due to the fact that the light source which represents the X-ray source was already underneath the beryllium part of the holder. Therefore, the illumination drops abruptly to zero. The window in the beryllium part has the effect that Q3 and Q4 have a larger range of higher illumination than Q1 and Q2.
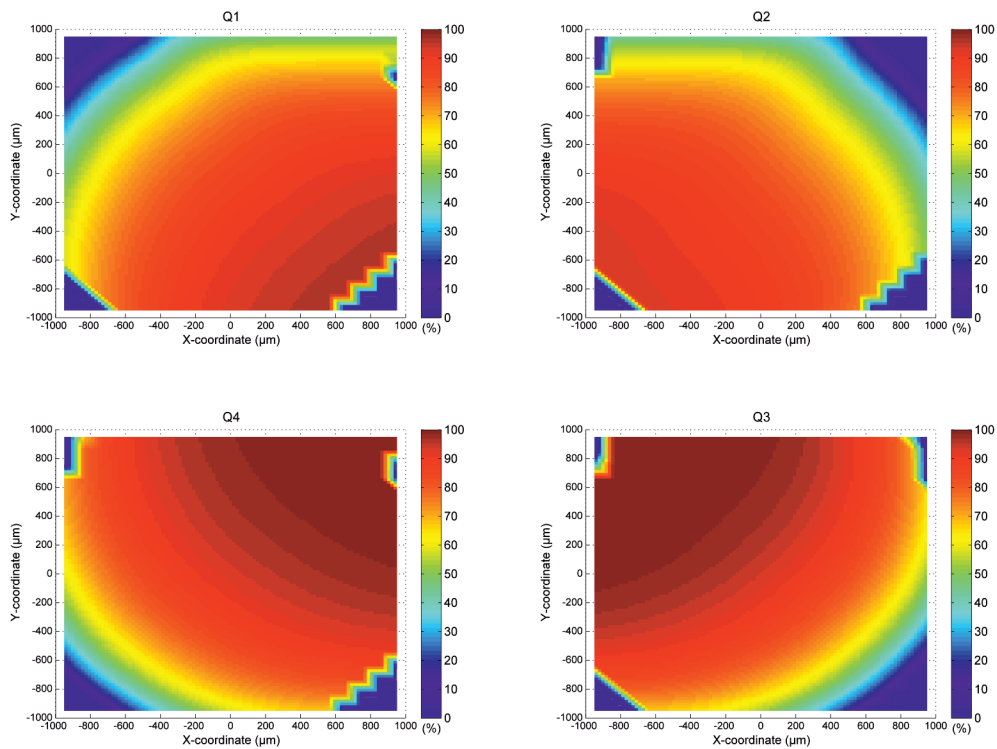
Figure 64: Illumination (%) at different *x/y* sample positions. Top left: Q1, top right: Q2, bottom left: Q4, bottom right: Q3.

In Figure 65 the total illumination of all four detectors is shown, for low and high energy X-rays as well as the systematic error, shown as a relative difference. The systematic error in this case is the relative difference of the two corresponding images (Figure 65a/ Figure 65b) shown in Figure 65c. It can clearly be seen that a full illumination of all four quadrants at zero degrees holder tilt is not possible neither for low nor for high energy X-rays. For low energy X-rays an illumination above 90% cannot be achieved. In Figure 65b the different positions of the detector can be seen without the beryllium part inserted. Figure 65c indicates that a offset of approximately 450 µm in *x-* or *y-* position at $\alpha = \beta = 0°$ leads to about 10% wrong X-ray intensity values due to absorption in the beryllium specimen carrier.
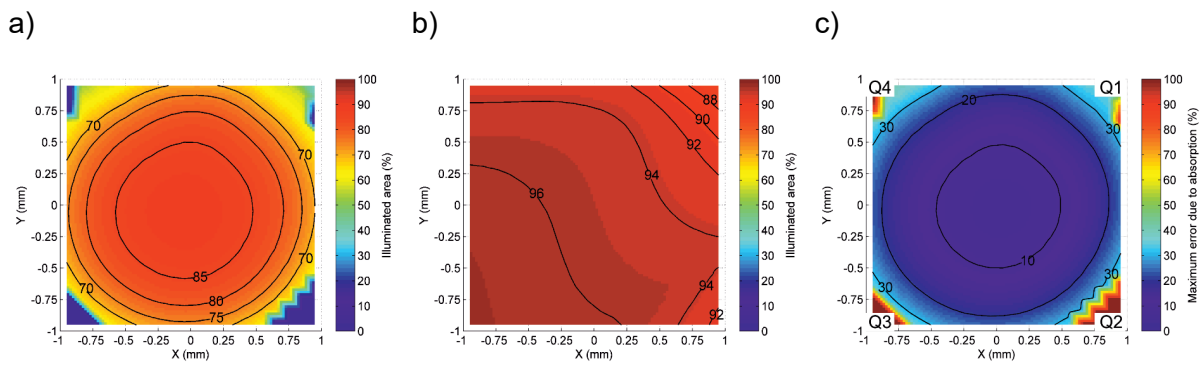
a)

b)

c)

Figure 65: Total illumination of all four quadrants (100% corresponds to all quadrants at 100%) at different sample positions. In (a) the illuminated area of all four detectors ($\alpha = \beta = 0°$) for different sample positions is shown. In (b) the same simulation results without the beryllium specimen carrier are shown. In (c) the maximum error which is possible due to absorption in the beryllium specimen carrier is shown for all four detectors.

For comparison, in Figure 66 the original data points without any interpolation are shown. The same shape, as in Figure 65a, can be observed. Each data point corresponds to the average illumination of all four detectors at each specimen holder position.
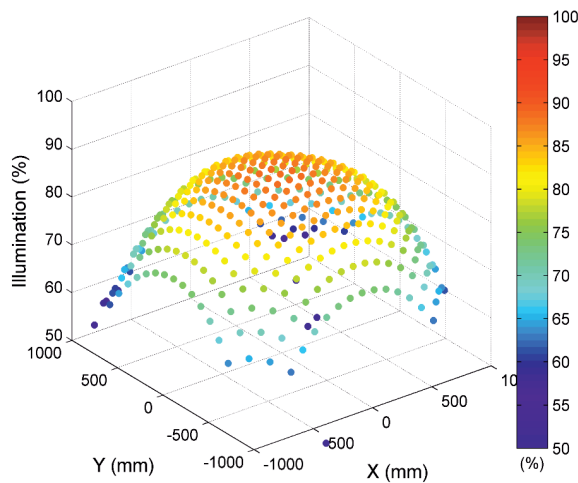

Figure 66: Total illumination of all four at different sample positions (50 µm steps).

As already mentioned in the introduction of this chapter, the *z*-height of the point of X-ray generation with respect to the specimen holder, is crucial for the shadow casted on the detectors. If the specimen holder is elevated by only 50 µm, the maximum achievable total illumination for all for quadrants at 0° holder tilt would be <83% (see Figure 67) because the

point of X-ray generation is lowered inside of the specimen holder. If each detector quadrant is considered separately, 100% illumination in case of Q1 and Q4 is no longer possible (see Figure 68).
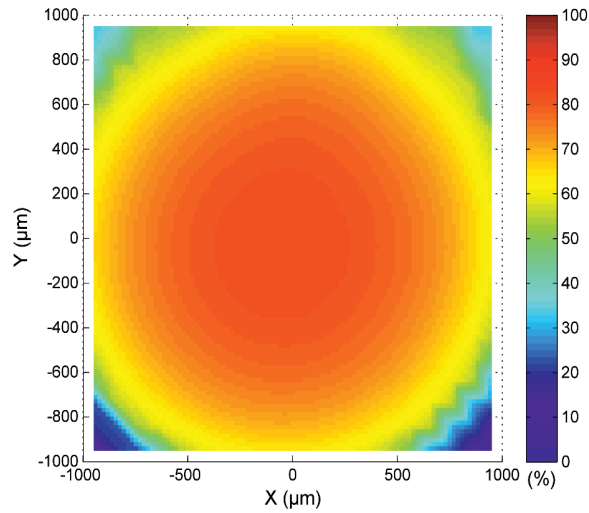

Figure 67: Total illumination of all four quadrants at different sample positions. The specimen holder is elevated by 50 µm.
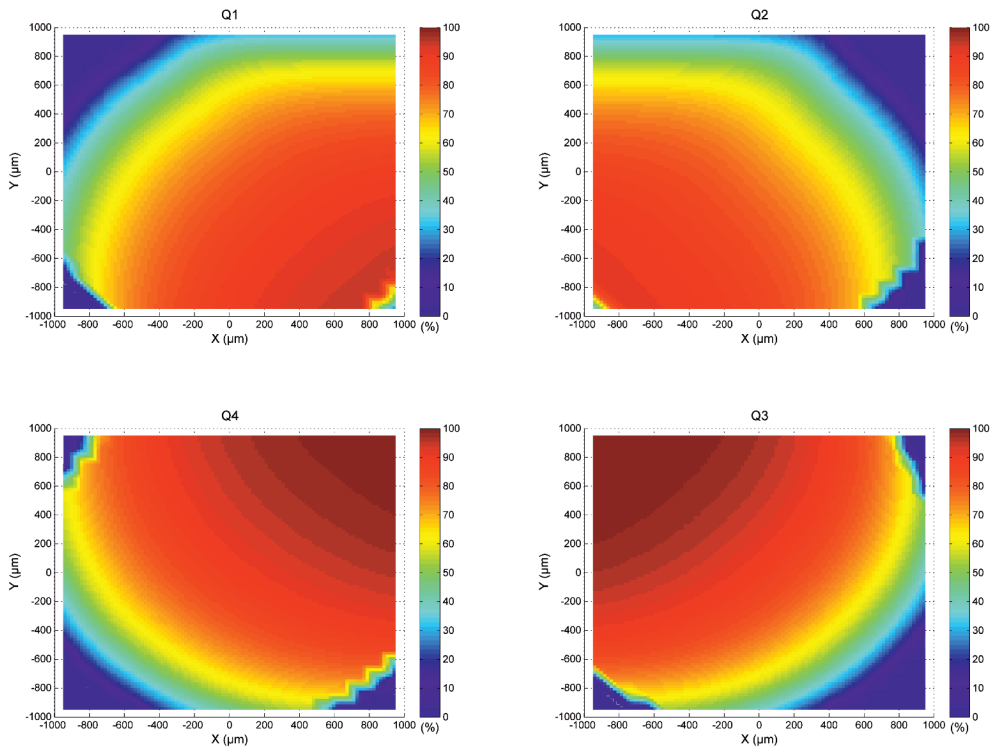
Figure 68: Illumination (%) at different *x-y-* sample positions. The specimen holder is elevated by 50 μm. Top left: Q1, top right: Q2, bottom left: Q4, bottom right: Q3.

If a spacer ring was used during measurements the point of X-ray generation would be shifted down even further into the specimen holder which would lead to an even higher elevated specimen holder with respect to the detectors. Here an example of an elevation of the specimen holder by 300 μm higher in respect to the optimum position (e.g. using a 0.3 mm aluminum spacer ring) is shown. In Figure 69 the effect of elevating the specimen holder by 300 μm is visible. If a measurement at $x = y = 0$ was performed each detector quadrant would only be ~50% illuminated. In this case the maximum achievable illumination is around 80% for Q1/Q2 and around 90% for Q3/Q4 without any holder tilt applied. If the total illumination of all four quadrants is considered, it can be seen that at least half of the total detector area is lost due to shadowing (compare Figure 70).
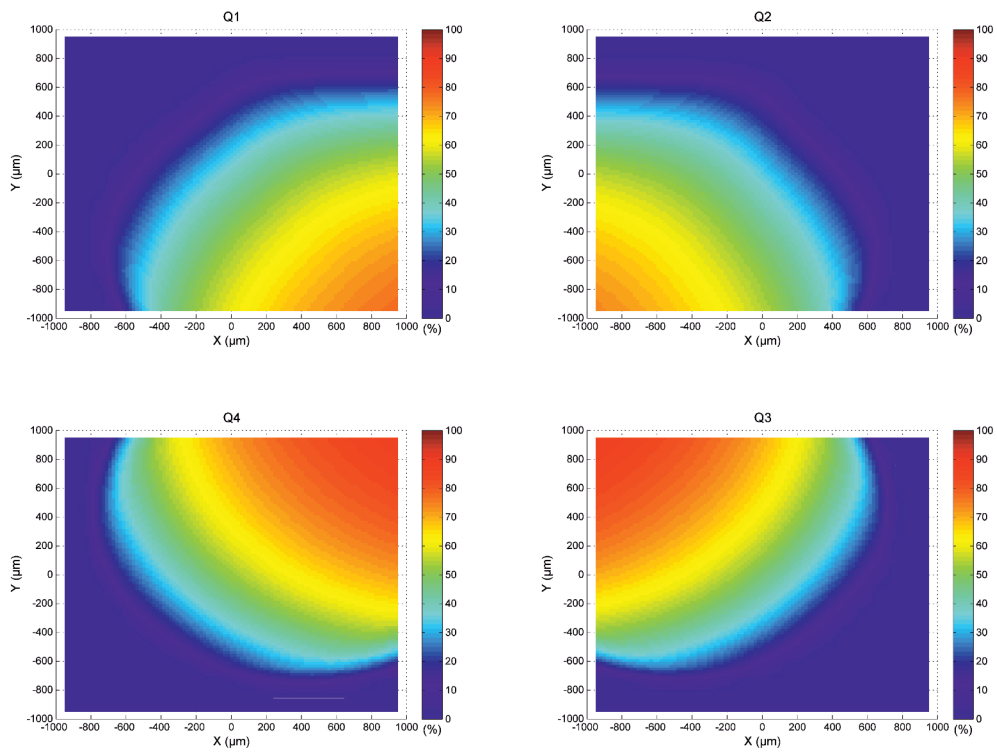
Figure 69: Illumination (%) at different *x-y-* sample positions. The specimen holder is elevated by300 µm. Top left: Q1, top right: Q2, bottom left: Q4, bottom right: Q3.
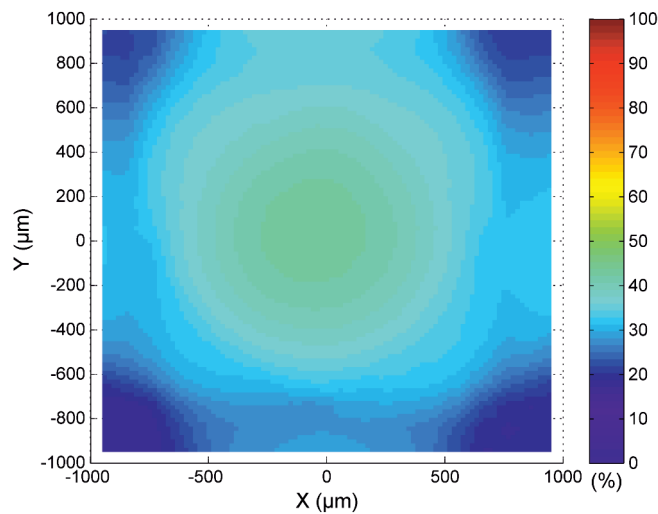
Figure 70: Total illumination of all four quadrants at different sample positions. The specimen holder is elevated by 300 µm.

In Figure 71 the detector illumination is plotted for different z-positions of the specimen holder, simulated for low energy X-rays. In the left plot $x = 0$ and y was varied from -950 µm to +950 µm in 50 µm steps and on the right hand side the y coordinate was kept constant at 0 and x was varied (also from -950 µm to 950 µm, 50 µm steps). The height of the specimen holder was shifted up by 50 µm for each line. The total maximum illumination (illumination for all four quadrants) is decreased by approximately 8% for each decrease in height of 50 µm. Both curves look rather alike due to the symmetric shape of the beryllium part. Only the beryllium window at the side of Q1 and Q4 leads to a slight increase of the total illumination in $+x$ direction.
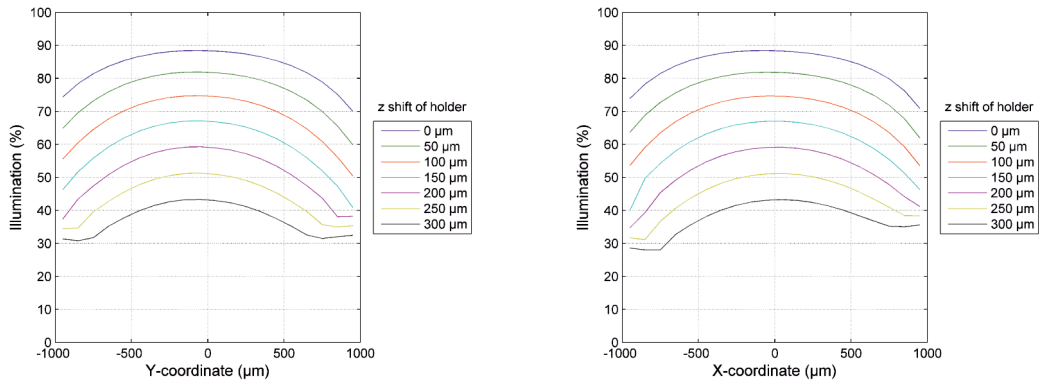
Figure 71: Total illumination (%) over *x*- (left) and *y*-positons (right) at different holder *z*-positions.

In Figure 72 and Figure 73 results for different holder positions are shown. In Figure 72 a *z*-height variation of up to 100 µm is depicted over the whole *x*- and *y*-space. The colour code only ranges from 50% to 100% illumination and a drastic decrease in illuminated can be seen. This holder position can easily be reached when not flat or bent samples are considered.
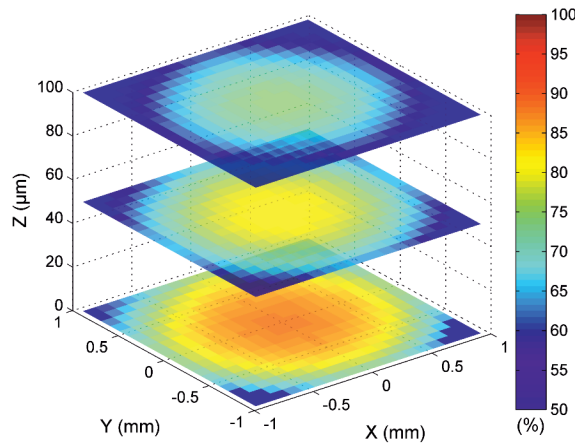
Figure 72: Total illumination of all four quadrants at different holder positions *z*=0 µm, 50 µm, 100 µm.

Using a spacer ring would set the holder up to 300 µm above the optimum position. The standard spacer ring heights are 0.1 mm, 0.2 mm and 0.3 mm. In Figure 73 the *z*-height variation is plotted up to 300 µm. The decrease in illuminated area for all four quadrants is dramatically, from ~80% to ~50% at maximum.

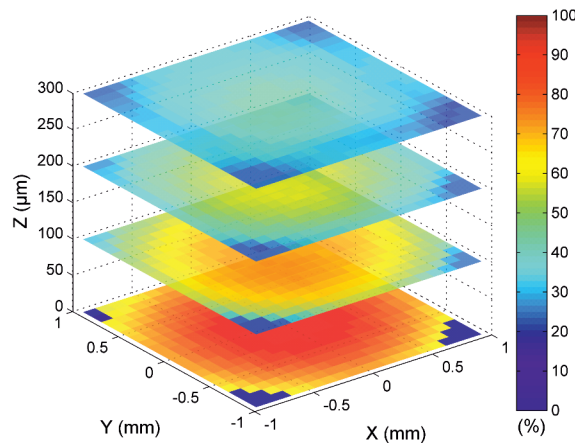**Figure 73: Total illumination of all four quadrants at different holder positions of**
_z_ = 0 μm, 100 μm, 200 μm, 300 μm.

4.5.2 _α-β_-tilt and _z_-height

To get a better understanding of the influence of the specimen holder tilt a simulation was performed varying the _α_- and _β_-tilt of the holder at _x_ = _y_ = 0. The _α_- and _β_-tilt were varied between ±30° in 2° steps. In Figure 74 the illumination over _α_- and _β_-tilt is plotted for each quadrant separately. The discrete data points were again linearly interpolated. A full illumination for low energy X-rays of the corresponding detector quadrant was achieved when the sample was tilted toward the detector. For example, a full illumination of Q1 was achieved when tilting in the positive _α_-direction and the negative _β_-direction. In Figure 75 the summed illuminations for all four quadrants are plotted over the simulated _α_- and _β_-tilt for low energy X-rays /with the beryllium specimen carrier) (Figure 75a), for higher energy X-rays (without the beryllium specimen carrier) (Figure 75b) and the maximum systematic error (Figure 75c). Unsurprisingly, the illumination of all four detectors is highest at 0° tilt in _α_- and _β_-direction (~90% illumination). In the simulations we neglected the clamp and the spacer ring (optional), which are inserted after the sample is mounted. Therefore, the Figure 75b only shows a change of illumination in _α_-tilt because the _β_-tilt only applies on the beryllium specimen carrier, which was taken out for this simulation, therefore a tilt in the _β_ direction has no effect on the shadow casted onto the detectors. In Figure 75c it is obvious that a change in _β_-tilt has a strong influence on the systematic error whereas a change in _α_-tilt has a moderate effect.
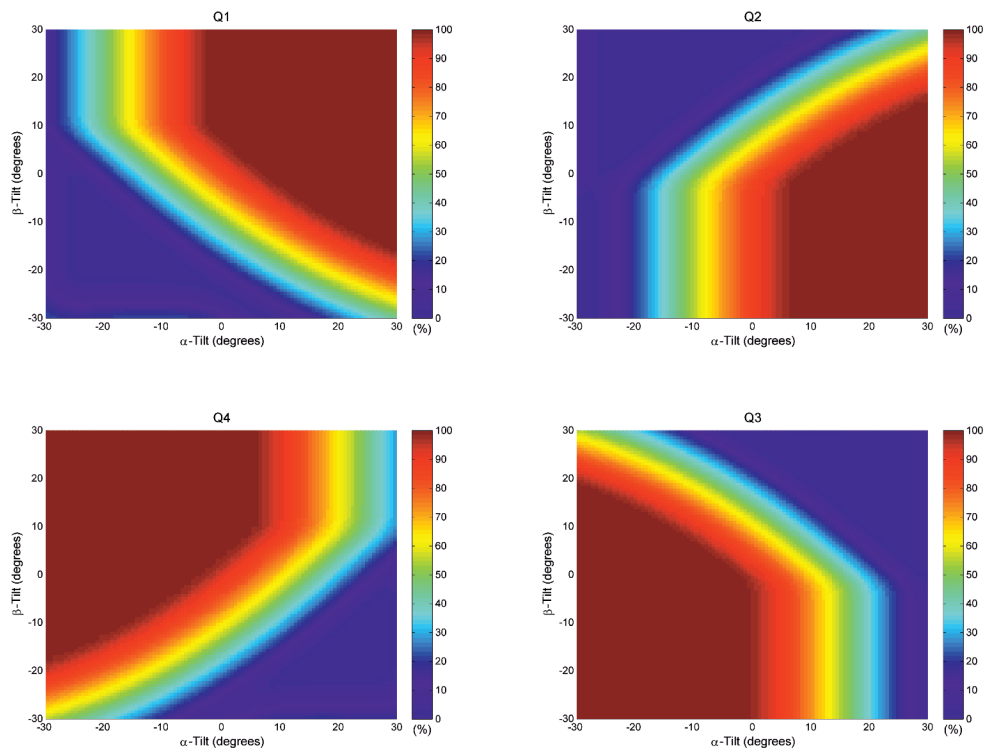
Figure 74: Illumination (%) at different *α-β*-tilts (at a holder position of *x= y = z* = 0).
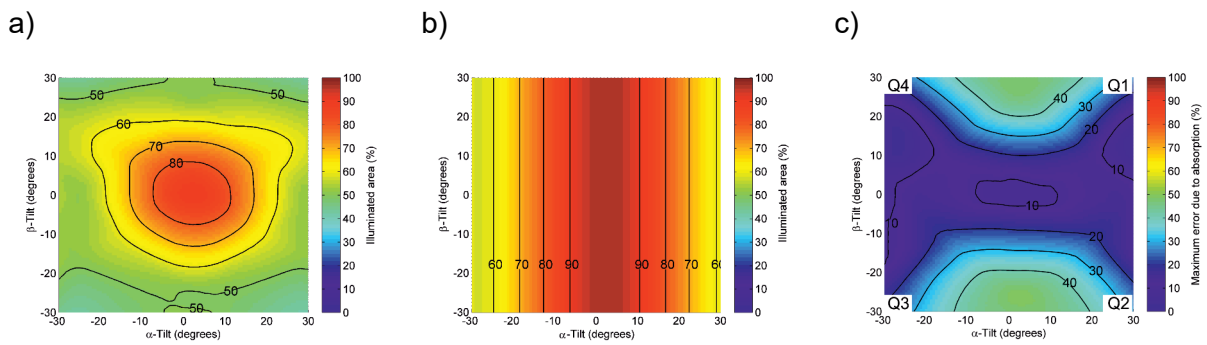**Top left: Q1, top right: Q2, bottom left: Q4, bottom right: Q3.**

a)

b)

c)

Figure 75: Total illumination of all four quadrants at different *α*- *β*- specimen holder tilts. In (a) the illuminated area of all four detectors (*x= y = z = 0*) for different sample tilts is shown. In (b) the same simulation results without the beryllium specimen carrier are shown. In (c) the maximum error which is possible due to absorption in the beryllium specimen carrier is shown for all four detectors.

Additionally, a simulation with an elevated specimen holder corresponding to a lowered point of X-ray generation, as done before considering the holder positions (see above Figure 67 - Figure 70). In Figure 76 the simulation results with a specimen holder elevated by 50 µm can be seen for each detector separately. In Figure 77 the summed illumination is shown. Compared to Figure 75 the area with an illumination of approximately 90% vanishes.

Figure 76: Illumination (%) at different *α-β*-tilts (at a holder position of *x= y* = 0). The specimen holder is elevated by 50 μm. Top left: Q1, top right: Q2, bottom left: Q4, bottom right: Q3.

Figure 77: Total illumination of all four quadrants at *α-β*-tilts. The specimen holder is elevated by 50 μm.

Simulations with a specimen holder elevated by 300 μm were also performed. Results can be seen in Figure 78 for each detector separately and the summed illumination in Figure 79. In these figures the illumination increased again at very high angles. This is due to the fact that light shines through underneath the beryllium and/or the holder part in the simulation. This might also be the case in real X-ray experiments but it has to be stated again that in the simulation no spacer ring was put on top of the sample and also no clamp was inserted. Therefore, we assume the results from these regions to be not very accurate.
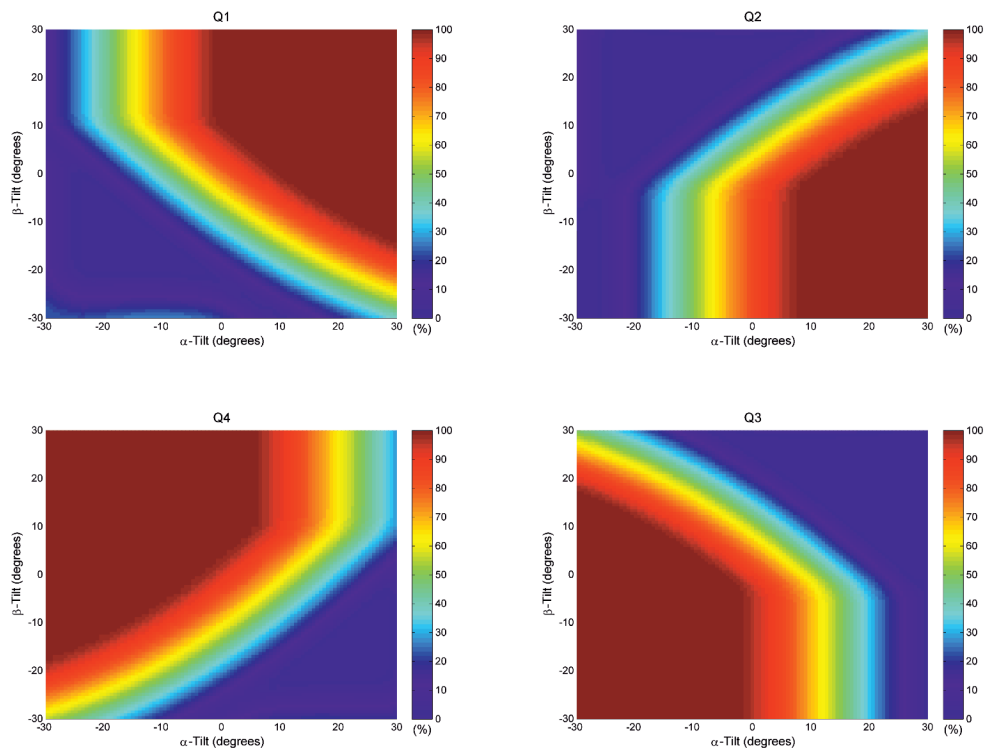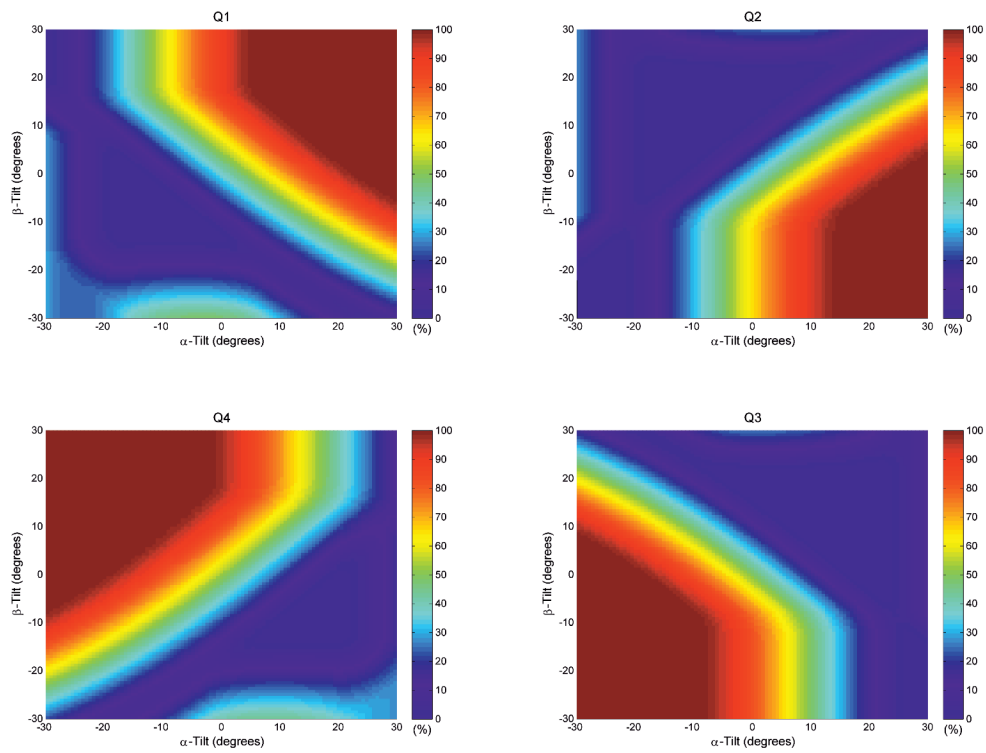
Figure 78: Illumination (%) at different *α-β*-tilts (at a holder position of *x*= *y* = 0). The specimen holder is elevated by 300 μm. Top left: Q1, top right: Q2, bottom left: Q4, bottom right: Q3.
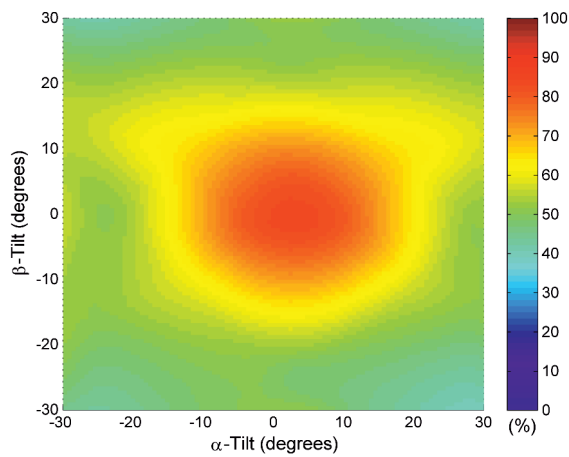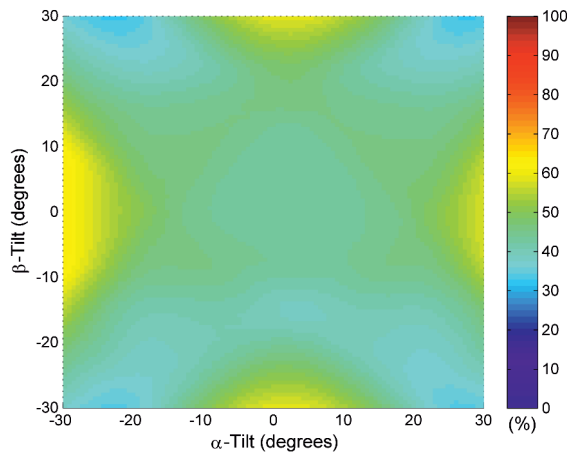
Figure 79: Total illumination of all four quadrants at *α-β*-tilts. The specimen holder is elevated by 300 µm.

To summarize the influence of a change in *z*-height on the whole space of *α*-and *β*- tilts in the range of ±30° the following plots were generated. In Figure 80 the holder position was increased by 0 µm, 50 µm, 100 µm and in Figure 81 *z*-heights of 0 µm, 100 µm, 200 µm and 300 µm. If e.g. the sample height was lowered by 100 µm a tilt of ~10° (in *α* or *β*) decreases the maximum achievable illumination to ~65%, so around one third of the X-ray signal is lost by the shadow of the brass part or altered by the shadow of the beryllium specimen carrier. The effect gets even more sever if the sample is tilted further.
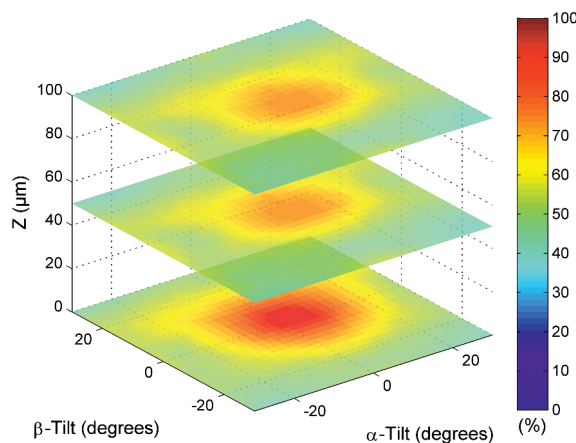
Figure 80: Total illumination of all four quadrants at different holder positions *z* = 0 µm, 50 µm, 100 µm.
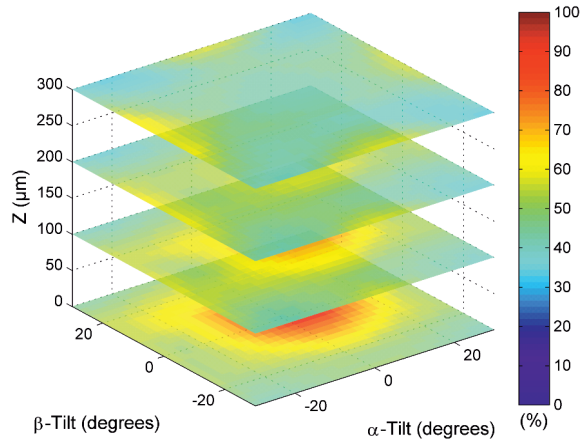
Figure 81: Total illumination of all four quadrants at different holder positions z = 0 μm, 100 μm, 200 μm and 300 μm.

4.5.3   Practical considerations

The findings above clearly show that if all four quadrants was used the energy dependent shadowing, arising from the beryllium specimen carrier of the holder, cannot be avoided. The easiest solution to this is to work only with one detector quadrant and tilt toward it. In Figure 82 a simulation was made were the holder position was varied between $x = y = \pm950$ μm in 50 μm steps and at an α-tilt of 0° till 10° in 1° steps for Q1 (first row) and Q2 (second row). The slices in the left column are plotted for an illumination of <99.8% for a better visibility of the red surface. The red surface indicates an illuminated area of 98%. It can be seen that Q1 already reaches >98% illumination at an α-tilt of 2° and a 100% at 3° α-tilt. In case of Q2 3° α-tilt is needed to reach illuminations >98% and 5° for 100% illumination of the detector. This is due to the brass part which is thicker in the direction of Q2. At an α-tilt of 10° around half of the possible x-y-positions achieve a 100% illumination of the detector area. This is true for both quadrants at different x-y-positions.

a)

b)

c)

d)
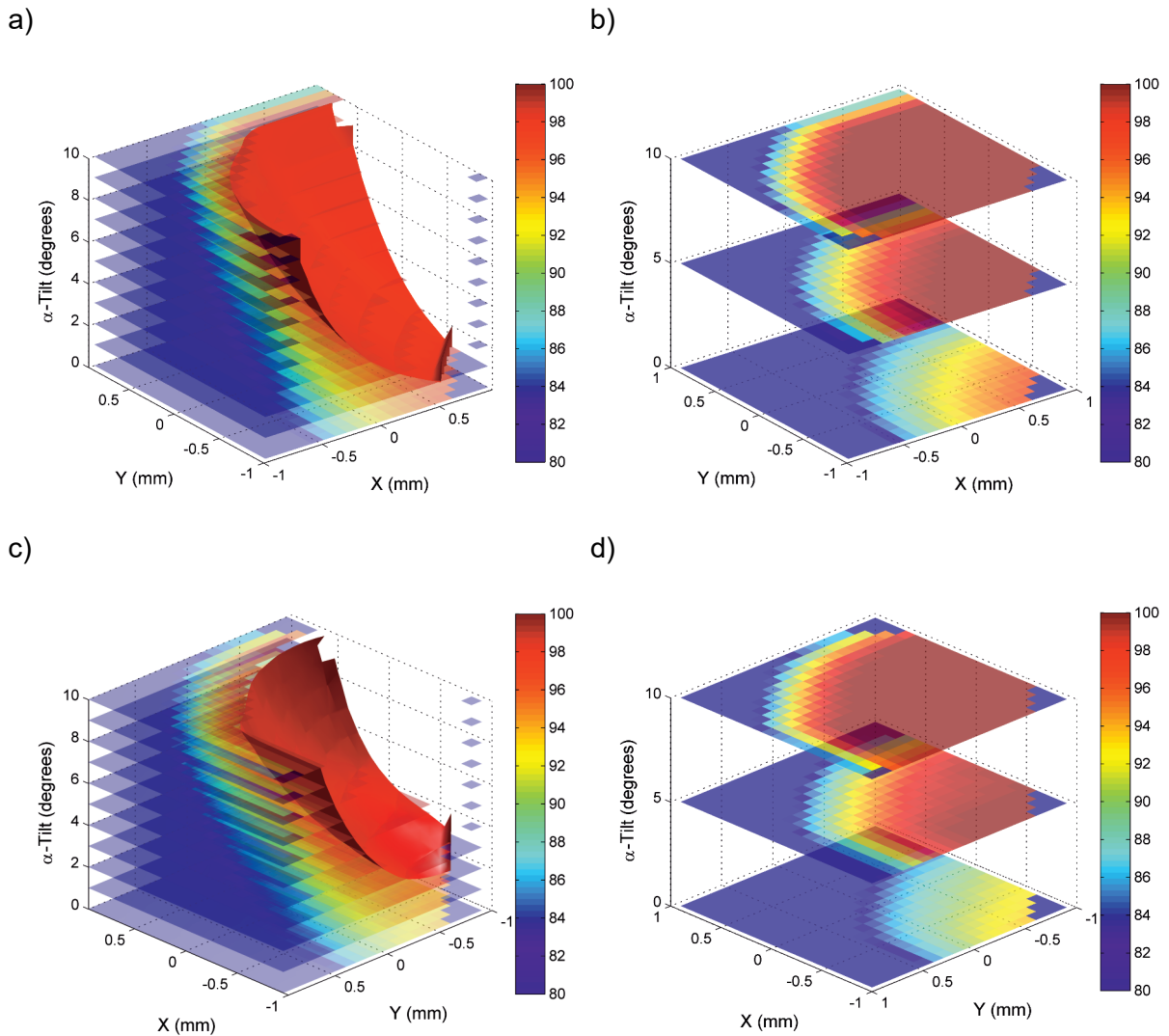
Figure 82: In the left column the illuminated area at different *x-y*-positions at an *α*-tilt from 0-10° in 1° steps are shown. The red surface indicates an illumination of 98%. The second column shows extracted slices for an *α*-tilt of 0°, 5° and 10°. In the first row results for Q1 (a) and (b) and in the second row results for Q2 (c) and (d) are shown.

Using only one detector quadrant would sacrifice one of the advantages of a Super-X system: its large active detector area. This may render elements of low concentrations invisible. So a possible trade-off is: using two detector quadrants and tilting toward one side (*α*-tilt). In Figure 83 the total signal for Q1 and Q2 is shown. The simulations were the same as in Figure 82, but this time the mean signal of both quadrants is shown (an illuminated area of 100% corresponds to a full illumination of both detectors). An illumination of 98% is reached at 4° *α*-tilt. A 100% illumination of both detector quadrants is reached at an *α*-tilt of 7°. At 0° *α*-tilt an illuminated area of 91% for Q1 and Q2 is achieved. Generally, the illuminated area increases

with a steeper angle (higher take-off angle) to the detector quadrants; hence the holder moves closer to the side of Q1 and Q2 (in minus *y* direction). In the direction along the holder, the x-direction, values close to 0 mm are preferred.

a)
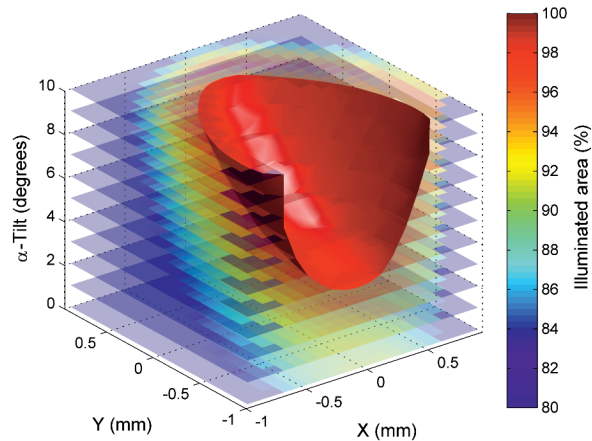
b)
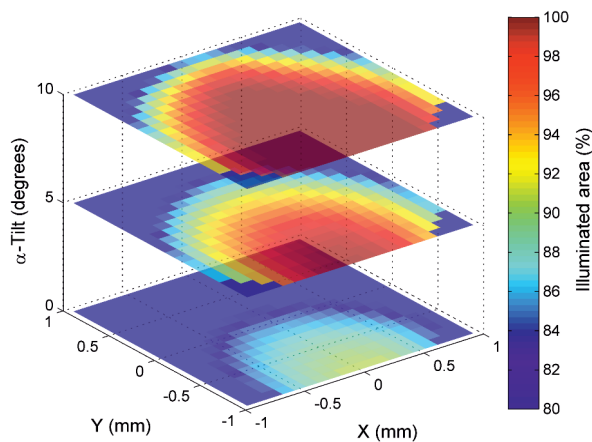
Figure 83: The signal for Q1 and Q2 is summed up (an illuminated area of 100% corresponds to both detectors fully illuminated). Different *x-y*-positions at an *α*-tilt from 0-10° in 1° steps are shown. The red surface indicates an illuminated area of 98%. (b) Slices for an *α*-tilt of 0°, 5° and 10° are shown.

To show the effect of the showing by the beryllium specimen carrier experimentally, a NiO_x standard specimen (Ted Pella, see also (*132*)) was analysed. At that time we had severe problems with the EDXS detectors which were switching off if the counts were too low.

Therefore, only ratios of the NiO_x were considered to be independent of that effect and also be independent of the measuring time and the beam current. For the measurements a position on the NiOx film, as close as possible to the center, was chosen. A measurement with each detector separately at each 2° α-tilt was made, between -24° to 28°. The spectra were evaluated using the window method (using the exact same energy range for each spectrum). The ratio of Ni L (0.58 keV) and O K (0.52 keV) should be marginally altered by the beryllium specimen carrier because both will experience a similar absorption. Whereas, the Ni K/ O K ratio should be altered by the beryllium specimen carrier because the difference in energy. Ni K at 7.48 keV will be far less absorbed in the beryllium part compared to O K. To correct for the absorption of the low energy X-rays a simulation at the same sample position was made. The Ni K/ O K ratio was corrected with the results of the simulation assuming that the O K X-rays are completely absorbed by the beryllium specimen carrier whereas the Ni K X-rays are not absorbed at all. Hence, the O K signal was multiplied with a correction factor for each tilt to compensate the percentage absorbed in the beryllium part.

Table 18: Mean value, standard deviation and relative standard deviations of the intensity ratios of Ni L/ O K, Ni K/ O K and Ni K/ O K corrected (left) and *α*-tilt versus intensity ratios of Ni L/ O K, Ni K/ O K and Ni K/ O K for Q1 to Q4 (right)

	Mean	σ	%σ
Ni L/ O K			
Q1	0.92	0.07	8%
Q2	0.87	0.07	8%
Q3	0.85	0.11	12%
Q4	0.73	0.09	13%
Ni K/ O K			
Q1	3.58	2.22	62%
Q2	2.25	0.33	15%
Q3	3.08	1.09	35%
Q4	3.06	1.47	48%
Ni K/ O K corrected			
Q1	2.30	0.26	11%
Q2	1.94	0.30	16%
Q3	2.75	0.58	21%
Q4	2.29	0.17	7%
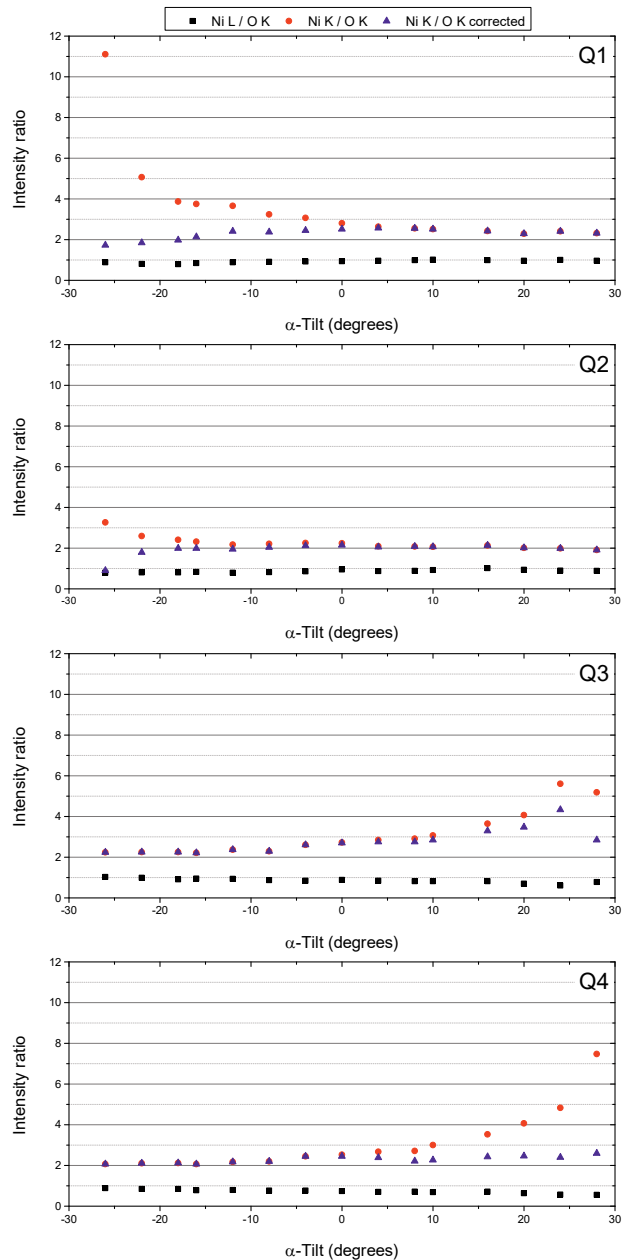
The results of the measurements can be seen in Table 18. In case of Q1 and Q4 the correction seems to work, the relative standard deviation significantly decreases. Considering the figures in Table 18 a slight overcorrection can be noticed. The relative deviations in case of Q2 and Q3 are generally lower, which can be attributed to the minor influence of the beryllium specimen carrier on the detectors in the back of the holder. It also has to be mentioned that the used NiO_x sample might not have been perfectly flat. Therefore, an absorption in sample

parts, layer or grid lines cannot be excluded. Finally, if one can assure that no shadowing from specimen parts (e.g. grid bars) have and influence we can correct for the absorption in the specimen holder by performing simulations with the geometrical setup at hand. Nevertheless, CINEMA 4D is only able to simulate a hard shadow therefore it is only an approximate correction.

4.5.4   Quantitative EDXS

In the last chapter, the influences of geometry on the quantification of a (virtual) Fayalite sample (Fe_2SiO_4, olivine group) are presented. Therefore, all relevant aspects are summarized and a further improvement of the simulation setup had to be done. These results are published in (*120*).

For a proper correction of the influence of the beryllium specimen carrier the exact path length through the beryllium has to be calculated. CINEMA 4D is not capable of doing so; therefore the model was transferred to MATLAB. The holder model was converted into voxels (10 µm x 10 µm). The detector discs were segmented with the same segment size (10 µm). The path length through the beryllium part was calculated using a cone-beam projection (ASTRA toolbox (*133*)) from a virtual point of X-ray generation to the detector segments. These gained beryllium thickness projection maps were transferred, for the corresponding X-ray energy, to absorption maps and finally absorption values, with which the X-ray intensity is applied.

The following observations must be considered for proper quantitative evaluation of EDX spectra.

Tilting of the specimen will inevitably create (partial) shadowing of the individual detectors. Equation (3.13) shows that shadowing will not change concentration values (the solid angle cancels out if all were measured at the same conditions). However, it will linearly distort the mass-thickness, and therefore the absorption correction will be incorrect. If no absorption correction is necessary, shadowing of one or more detectors will yield correct results.

X-rays may be absorbed differently when passing through parts of the specimen holder (beryllium specimen carrier). This behaviour results in energy-dependent shadowing, and the effective solid angle will depend on the X-ray energy. As a consequence, equation (3.13) indicates that the concentration values will be altered and systematically incorrect, even when no absorption correction is required.

The take-off angles will be different for each detector when a specimen tilt is applied (Table 7). Tilting toward one detector will increase its take-off angle and decrease the take-off angle for the other detectors. This will change the absorption path of the X-rays through the specimen.

The Fayalite sample contains two X-ray lines for which absorption in the sample can be neglected (Fe K and Si K), whereas the O K line is significantly absorbed in the sample (maximum specimen thickness for thin film criterion is approximately 1 nm). The energy of the Fe K_α line at 6.4 keV is high enough to penetrate the beryllium specimen carrier with no significant loss of intensity (2% are absorbed considering all four detectors at the given holder position). However, the Si K and O K lines will experience absorption in the beryllium carrier.

For the calculations, the specimen was tilted by α = -15° and β = +3° (i.e., toward Q4) and shifted by x = +300 µm and y = +200 µm. We assumed a homogenous specimen thickness of 100 nm (parallel slab) and computed the X-ray intensity reaching each detector, taking into account absorption in the sample and absorption and shadowing from the specimen holder. We took these calculated intensities and performed a quantitative evaluation using ζ-factors and absorption correction. The quantitative results are shown in Table 19.

Table 19: Quantification results for a 100 nm thick Fayalite sample. The percentage values represent the relative differences to the nominal values and correspond to the systematic quantification error when neglecting shadowing effects.

	atomic ratio Si/Fe		atomic ratio O/Fe		ρt [10^{-4} kg/m^2]	
nominal	0.5		2		4.39	
Q1	0.38	-24%	1.39	-31%	3.04	-31%
Q2	0.23	-54%	0.67	-66%	1.52	-65%
Q3	0.5		2		4.39	
Q4	0.5		2		4.39	
Q1-Q4	0.43	-14%	1.63	-18%	3.32	-25%

As expected, the concentrations and the mass thickness are correct for Q4 and Q3 (facing the sample surface). However, the quantification is incorrect for detectors Q1 and Q2. The signals and the deviations from all 4 detectors reach a mean value between 14% and 18%. This example suggests that neglecting the above-described effects leads to a significant systematic quantification error. This error exceeds typical measurement errors of EDXS quantification.

This deviation occurs because of shadowing and can be accounted for in the quantification process. If the signals of all 4 detectors are available separately, the simulated values for shadowing (including the beryllium specimen carrier) can be used as inputs and the results for all detectors will be correct. When only the summed signal of all 4 detectors is available on the Super-X system, a calculated value for shadowing will not completely correct the effects but lead to a significant improvement (less than 2% error for the above described example).

5   Conclusion

The leitmotif of this thesis was the quantification of light elements with EDXS. In the first part organic electronics devices are characterized. These devices mainly contain elements which are challenging to be analysed with EDXS mainly due to absorption effects. The ζ-factor method presents a method how EDXS can be used to quantify also samples containing these light elements. This is due to the possibility of applying an iterative absorption correction because the mass-thickness is provided. To use the ζ-factor technique the sensitivity factors need to be measured. The challenge of measuring ζ-factors is given by the lack of the knowledge of the absolute thickness of the used samples and having stable standard materials (no change of stoichiometry and density under the electron beam). We presented a convenient way to determine ζ-factors and present it on the example of Al, O and Si. The sample thickness is obtained by using a circular symmetric rod and the ζ-factor is measured on a plan parallel sample, to be able to apply absorption correction. Measuring ζ-factors on a four detector quadrant system presents more challenges. Not only that the ζ-factors have to be measured for each detector separately but also, that a full illumination of all detectors is not possible at the same time. One needs to know exactly how much each detector is illuminated at which sample position. Furthermore, not only the positioning of the sample is important, considering its tilt and positon, but also its configuration with respect to the exact detector positions. To this end, we present a method how the positions of the four detector quadrants can be determined. This was done using a combination of a tilting experiment with a well-known sample and simulations. These simulations were done using a 3D rendering program. By comparing the experiment and the simulations, the exact position of all four detector quadrants were determined. During this work, we also found out that the beryllium part of the sample holder has a severe effect on the gained X-ray counts. For a reliable quantification on a four quadrant detector system using all four quadrants at once the following aspects have to be considered: One would need to consider the absorption of X-rays in the sample, the absorption in the beryllium portion of the holder and finally the amount of each detector illuminated. We can simulate the exact illumination of each detector at each holder position. We also can calculate the path length of the X-rays through the beryllium portion. The X-ray signal is only available four all detectors at once. So far, we are not able to implement all of these aspects for each detector in the iterative quantification with the ζ-factor technique. Generally, it also has to be stated that all ζ-factors have to be measured at the exact same amount of illumination to produce reliable results. This problem is probably the reason why the determination of ζ-factors at the Super-X system was inconsistent.

6 References

1. Editorial, Embracing the organics world, *Nat Mater*. **12**, 591 (2013).

2. C. Auner *et al.,* Residue-free room temperature UV-nanoimprinting of submicron organic thin film transistors, *Organic Electronics*. **10**, 1466–1472 (2009).

3. C. Auner *et al.,* High-performing submicron organic thin-film transistors fabricated by residue-free embossing, *Organic Electronics*. **11**, 552–557 (2010).

4. K. Zojer *et al.,* Switching from weakly to strongly limited injection in self-aligned, nano-patterned organic transistors, *Sci Rep*. **6**, 31387 (2016).

5. T. Rothländer *et al.,* Channel length variation in self-aligned, nanoimprint lithography structured OTFTs, *Organic Electronics*. **15**, 3274–3281 (2014).

6. J. Kraxner, R. Schmied, H. Plank, W. Grogger, Analytical TEM in organic electronics, *Imaging & Microscopy*. **2014**, 36–38 (2014).

7. S. Fladischer, Phd thesis, University of Technology Graz (08.07.2013).

8. W. P. Reed, *Certificate of Analysis*, *Standard Reference Material 2063* (1993).

9. M. Watanabe, D. B. Williams, The quantitative analysis of thin specimens: a review of progress from the Cliff-Lorimer to the new zeta-factor methods, *J Microsc*. **221**, 89–109 (2006).

10. H. Klauk, Ed., *Organic Electronics* (Wiley-VCH Verlag GmbH & Co. KGaA, Weinheim, FRG, 2006).

11. H. Klauk, Organic thin-film transistors, *Chem. Soc. Rev.* **39**, 2643 (2010).

12. D. Gamota, *Printed Organic and Molecular Electronics // Printed organic and molecular electronics* (Springer US; Springer Science+Business Media, LLC, Boston, MA, 2004).

13. P. Stallinga, *Electrical characterization of organic electronic materials and devices* (John Wiley & Sons, Chichester, U.K., 2009).

14. H. Klauk, B. Gnade, in *Printed Organic and Molecular Electronics*, D. Gamota, P. Brazis, K. Kalyanasundaram, J. Zhang, Eds. (Springer US, Boston, MA, 2004), pp. 1–82.

15. D. J. Gundlach *et al.,* An experimental study of contact effects in organic thin film transistors, *J. Appl. Phys.* **100**, 24509 (2006).

16. U. Palfinger *et al.,* Fabrication of n- and p-Type Organic Thin Film Transistors with Minimized Gate Overlaps by Self-Aligned Nanoimprinting, *Adv. Mater.* **22**, 5115–5119 (2010).

17. T. Rothländer, Phd tehsis, University of Technology Graz (2014).

18. T. Rothländer *et al.,* Channel length variation in self-aligned, nanoimprint lithography structured OTFTs, *Organic Electronics*. **15**, 3274–3281 (2014).

19. A. Knobloch, A. Manuelli, A. Bernds, W. Clemens, Fully printed integrated circuits from solution processable polymers, *J. Appl. Phys.* **96**, 2286 (2004).

20. A. Orthacker *et al.,* Chemical degradation and morphological instabilities during focused ion beam prototyping of polymers, *Phys Chem Chem Phys*. **16**, 1658–1666 (2014).

21. R. Schmied, B. Chernev, G. Trimmel, H. Plank, New possibilities for soft matter applications: eliminating technically induced thermal stress during FIB processing, *RSC Adv.* **2**, 6932 (2012).

22. R. Schmied *et al.,* A combined approach to predict spatial temperature evolution and its consequences during FIB processing of soft matter, *Phys Chem Chem Phys*. **16**, 6153–6158 (2014).

23. D. C. Martin, J. Chen, J. Yang, L. F. Drummy, C. Kübel, High resolution electron microscopy of ordered polymers and organic molecular crystals: Recent developments and future possibilities, *J. Polym. Sci. B Polym. Phys.* **43**, 1749–1778 (2005).

24. D. C. Martin, E. L. Thomas, Experimental high-resolution electron microscopy of polymers, *Polymer*. **36**, 1743–1759 (1995).

25. C. J. Takacs *et al.,* Remarkable order of a high-performance polymer, *Nano Lett*. **13**, 2522–2527 (2013).

26. J. A. Love *et al.,* Film Morphology of High Efficiency Solution-Processed Small-Molecule Solar Cells, *Adv. Funct. Mater.* **23**, 5019–5026 (2013).

27. L. F. Drummy *et al.,* Molecular-Scale and Nanoscale Morphology of P3HT:PCBM Bulk Heterojunctions: Energy-Filtered TEM and Low-Dose HREM †, *Chem. Mater.* **23**, 907–912 (2011).

28. M. Pfaff *et al.,* Bulk heterojunction nanomorphology of fluorenyl hexa-peri-hexabenzocoronene-fullerene blend films, *ACS Appl Mater Interfaces*. **5**, 11554–11562 (2013).

29. X. Zhang *et al.,* In-Plane Liquid Crystalline Texture of High-Performance Thienothiophene Copolymer Thin Films, *Adv. Funct. Mater.* **20**, 4098–4106 (2010).

30. J. Petermann, H. Moritz, U. Rieck, B. A. Wood, E. L. Thomas, A novel TEM dark-field contrast method for semi-crystalline polymers, *J Mater Sci Lett*. **8**, 1023–1025 (1989).

31. D. B. Williams, C. B. Carter, *Transmission electron microscopy*, *A textbook for materials science* (Springer, New York, ed. 2, 2009).

32. K. Yamauchi *et al.,* Microdomain Morphology in an ABC 3-Miktoarm Star Terpolymer: A Study by Energy-Filtering TEM and 3D Electron Tomography, *Macromolecules*. **36**, 6962–6966 (2003).

33. K. Varlot, J. Martin, D. Gonbeau, C. Quet, Chemical bonding analysis of electron-sensitive polymers by EELS, *Polymer*. **40**, 5691–5697 (1999).

34. R. J. Spontak, P. Alexandridis, Advances in self-ordering macromolecules and nanostructure design, *Current Opinion in Colloid & Interface Science*. **4**, 140–146 (1999).

35. R. W. Smith, V. Bryg, Staining Polymers for Microscopical Examination, *Rubber Chemistry and Technology*. **79**, 520–540 (2006).

36. J. Loos, E. Sourty, K. Lu, G. de With, S. v. Bavel, Imaging Polymer Systems with High-Angle Annular Dark Field Scanning Transmission Electron Microscopy (HAADF−STEM), *Macromolecules*. **42**, 2581–2586 (2009).

37. T. Chou, P. Prayoonthong, A. Aitouchen, M. Libera, Nanoscale artifacts in RuO4-stained poly(styrene), *Polymer*. **43**, 2085–2088 (2002).

38. S. Yakovlev, M. Libera, Dose-limited spectroscopic imaging of soft materials by low-loss EELS in the scanning transmission electron microscope, *Micron*. **39**, 734–740 (2008).

39. M. R. Libera, R. F. Egerton, Advances in the Transmission Electron Microscopy of Polymers, *Polymer Reviews*. **50**, 321–339 (2010).

40. C. Guo *et al.,* Probing Local Electronic Transitions in Organic Semiconductors through Energy-Loss Spectrum Imaging in the Transmission Electron Microscope, *Adv. Funct. Mater.* **25**, 6071–6076 (2015).

41. K. Varlot, J. Martin, C. Quet, EELS analysis of PMMA at high spatial resolution, *Micron*. **32**, 371–378 (2000).

42. A. E. Ribbe, M. Hayashi, M. Weber, T. Hashimoto, Morphology Determination of Novel Polysulfone−Polyamide Block Copolymers Using Element Spectroscopic Imaging in the Transmission Electron Microscopy, *Macromolecules*. **33**, 2786–2789 (2000).

43. M. M. Rippel, C. A. Paula Leite, F. Galembeck, Elemental Mapping in Natural Rubber Latex Films by Electron Energy Loss Spectroscopy Associated with Transmission Electron Microscopy, *Anal. Chem.* **74**, 2541–2546 (2002).

44. C. Correa, B. Bonse, C. Chinaglia, E. Hage, L. Pessan, Characterization of unstained multiphase polymer systems by analytical electron microscopy, *Polymer Testing*. **23**, 775–778 (2004).

45. Y. Liao, A. Nakagawa, S. Horiuchi, T. Ougizawa, Interdiffusion at Homopolymer/Random Copolymer Interfaces Investigated by Energy-Filtering Transmission Electron Microscopy, *Macromolecules*. **40**, 7966–7972 (2007).

46. E. D. Gomez *et al.,* Interfacial Concentration Profiles of Rubbery Polyolefin Lamellae Determined by Quantitative Electron Microscopy, *Macromolecules*. **41**, 156–162 (2008).

47. T. Hayakawa *et al.,* Self-Assembled Lamellar Nanostructures of Wholly Aromatic Rod−Rod-Type Block Molecules, *Org. Lett.* **8**, 5453–5456 (2006).

48. E. D. Gomez *et al.,* Effect of Ion Distribution on Conductivity of Block Copolymer Electrolytes, *Nano Lett.* **9**, 1212–1216 (2009).

49. F. Allen, M. Watanabe, Z. Lee, N. Balsara, A. Minor, Chemical mapping of a block copolymer electrolyte by low-loss EFTEM spectrum-imaging and principal component analysis, *Ultramicroscopy*. **111**, 239–244 (2011).

50. R. F. Egerton, *Electron energy-loss spectroscopy in the electron microscope* (Plenum Press, New York, ed. 2, 1996).

51. G. Cliff, G. W. Lorimer, The quantitative analysis of thin specimens, *J Microsc*. **103**, 203–207 (1975).

52. M. Malac, R. F. Egerton, Calibration Specimens for Determining Energy-Dispersive X-ray k-Factors of Boron, Nitrogen, Oxygen, and Fluorine, *Microsc. Microanal.* **5**, 29–38 (1999).

53. M. Watanabe, D. B. Williams, Quantification of Elemental Segregation to Lath and Grain Boundaries in Low-Alloy Steel by STEM X-Ray Mapping Combined with the ζ-Factor Method, *MEKU*. **94**, 307–316 (2003).

54. V Banchet, J Michel, E Jallot, D Laurent-Maquin, G Balossier, Light elements quantitative x-ray microanalysis of thin samples in STEM. Absorption correction using EELS data, *Journal of Physics D: Applied Physics*. **36**, 1599 (2003).

55. M. Watanabe, Z. Horita, M. Nemoto, Absorption correction and thickness determination using the ζ factor in quantitative X-ray microanalysis, *Ultramicroscopy*. **65**, 187–198 (1996).

56. H. A. Kramers, XCIII. On the theory of X-ray absorption and of the continuous X-ray spectrum, *Philosophical Magazine Series 6*. **46**, 836–871 (1923).

57. M. N. Mazziotta, Electron–hole pair creation energy and Fano factor temperature dependence in silicon, *Nuclear Instruments and Methods in Physics Research Section A: Accelerators, Spectrometers, Detectors and Associated Equipment*. **584**, 436–439 (2008).

58. B. G. Lowe, R. A. Sareen, A measurement of the electron–hole pair creation energy and the Fano factor in silicon for 5.9keV X-rays and their temperature dependence in the range 80–270K, *Nuclear Instruments and Methods in Physics Research Section A: Accelerators, Spectrometers, Detectors and Associated Equipment*. **576**, 367–370 (2007).

59. N. J. Zaluzec, Processing and quantification of X-ray Energy-Dispersive Spectra in the Analytical Electron Microscope, *Ultramicroscopy*. **28**, 226–235 (1989).

60. N. Ritchie, J. M. Davis, D. E. Newbury, DTSA-II, *Microsc Microanal*. **14**, 1176–1177 (2008).

61. N. W. Ritchie, Spectrum simulation in DTSA-II, *Microsc Microanal*. **15**, 454–468 (2009).

62. J. Wood, D. B. Williams, J. I. Goldstein, Determination of Cliff-Lorimer k factors for Philips EM400T, *Quantitative Analysis with High Spatial Resolution, Metals Society, London* (1981).

63. J. E. Wood, D. B. Williams, J. I. Goldstein, Experimental and theoretical determination of kAFe factors for quantitative X-ray microanalysis in the analytical electron microscope, *Journal of microscopy*. **133**, 255–274 (1984).

64. R. J. Graham, J. W. Steeds, Determination of Cliff-Lorimer k factors by analysis of crystallized microdroplets, *Journal of microscopy*. **133**, 275–280 (1984).

65. P. J. Sheridan, Determination of experimental and theoretical kASi factors for a 200-kV analytical electron microscope, *J Electron Microsc Tech*. **11**, 41–61 (1989).

66. J. Lammer, Master thesis, University of Technology Graz (2016).

67. W. Bambynek, B. Crasemann, R. W. Fink, H. U. Freund, Hans Mark, C. D. Swift, R. E. Price, and P. Venugopala Rao, X-Ray Fluorescence Yields, Auger, and Coster-Kronig Transition Probabilities, *Rev. Mod. Phys.* **44**, 716–813 (1972).

68. M. O. Krause, *Atomic radiative and radiationless yields for K and L shells* (American Chemical Society and the American Institute of Physics for the National Bureau of Standards, [New York], 1979).

69. J. H. Hubbell *et al.,* A Review, Bibliography, and Tabulation of K, L, and Higher Atomic Shell X-Ray Fluorescence Yields, *Journal of Physical and Chemical Reference Data*. **23**, 339–364 (1994).

70. X. Llovet *et al.*, *NIST Database of Cross Sections for Inner-Shell Ionization by Electron or Positron Impact* (National Institute of Standards and Technology, Gaithersburg, Maryland, 2014).

71. D. Bote, F. Salvat, A. Jablonski, C. J. Powell, Cross sections for ionization of K, L and M shells of atoms by impact of electrons and positrons with energies up to 1GeV: Analytical formulas, *Atomic Data and Nuclear Data Tables*. **95**, 871–909 (2009).

72. D. Bote, F. Salvat, Calculations of inner-shell ionization by electron impact with the distorted-wave and plane-wave Born approximations, *Phys. Rev. A*. **77** (2008).

73. X. Llovet, C. J. Powell, F. Salvat, A. Jablonski, Cross Sections for Inner-Shell Ionization by Electron Impact, *J. Phys. Chem. Ref. Data*. **43**, 13102 (2014).

74. J. Philibert, in *Symposium on Advances in Techniques in Electron Metallography* (ASTM International, 100 Barr Harbor Drive, PO Box C700, West Consho hocken, PA 19428-2959, 1963), 3.

75. G. Kothleitner, W. Grogger, M. Dienstleder, F. Hofer, Linking TEM Analytical Spectroscopies for an Assumptionless Compositional Analysis, *Microsc Microanal*, 1–9 (2014).

References

76. S. J. B. Reed, *Electron microprobe analysis* (Cambridge Univ. Press, Cambridge u.a., ed. 2, 1997).

77. S. M. Zemyan, Phd thesis, Lehigh University (01.01.1996).

78. D. B. Williams, M. Watanabe, D. T. Carpenter, Thin film analysis and chemical mapping in the analytical electron microscope (vol 15, pg 49, 1998), *MIKROCHIMICA ACTA*. **131**, 246 (1999).

79. M. G. Burke, M. Watanabe, D. B. Williams, J. M. Hyde, Quantitative characterization of nanoprecipitates in irradiated low-alloy steels: advances in the application of FEG-STEM quantitative microanalysis to real materials, *J Mater Sci*. **41**, 4512–4522 (2006).

80. S. Fladischer, W. Grogger, Quantitative EDXS analysis of organic materials using the ζ-factor method, *Ultramicroscopy*. **136**, 26–30 (2014).

81. M. Rathi, S. P. Ahrenkiel, J. J. Carapella, M. W. Wanlass, A standards-based method for compositional analysis by energy dispersive X-ray spectrometry using multivariate statistical analysis: application to multicomponent alloys, *Microsc. Microanal.* **19**, 66–72 (2013).

82. M. Lopez-Haro *et al.,* Obtaining an accurate quantification of light elements by EDX: K-factors vs. Zeta-factors, *18th International Microscopy Congress; Czechoslovak Microscopy Society: Prague* (2014).

83. B. Goris *et al.,* Towards Quantitative EDX Results in 3 Dimensions, *Microsc Microanal*. **20**, 766–767 (2014).

84. D. Zanaga, T. Altantzis, J. Sanctorum, B. Freitag, S. Bals, An alternative approach for ζ-factor measurement using pure element nanoparticles, *Ultramicroscopy*. **164**, 11–16 (2016).

85. C.T. Chantler, K. Olsen, R.A. Dragoset, J. Chang, A.R. Kishore, S.A. Kotochigova, and D.S. Zucker, *X-Ray Form Factor, Attenuation,and Scattering Tables*, *Detailed Tabulation of Atomic Form Factors, Photoelectric Absorption and Scattering Cross Section, and Mass Attenuation Coefficients for Z = 1-92 from E = 1-10 eV to E = 0.4-1.0 MeV* (2001) (available at http://www.nist.gov/pml/data/ffast/).

86. Georg Thieme Verlag KG, *RÖMPP*.

87. M. Habermeyer, RÖMPP-Redaktion, H. Sitzmann, *Aluminium* (2016) (available at https://roempp.thieme.de/roempp4.0/do/data/RD-01-01786).

88. RÖMPP-Redaktion, H. Sitzmann, *Aluminiumoxide* (2016) (available at https://roempp.thieme.de/roempp4.0/do/data/RD-01-01815).

89. *Titan™ G2 with ChemiSTEM™ Technology*, *A revolution in atomic analytics*, Applicationnote (2011).

90. G. Kothleitner *et al.,* Quantitative Elemental Mapping at Atomic Resolution Using X-Ray Spectroscopy, *Phys. Rev. Lett.* **112** (2014).

91. N. R. Lugg, G. Kothleitner, N. Shibata, Y. Ikuhara, On the quantitativeness of EDS STEM, *Ultramicroscopy.* **151**, 150–159 (2015).

92. Z. Chen *et al.,* Energy dispersive X-ray analysis on an absolute scale in scanning transmission electron microscopy, *Ultramicroscopy.* **157**, 21–26 (2015).

93. J. Orloff, M. Utlaut, L. Swanson, *High Resolution Focused Ion Beams: FIB and its Applications*, *The Physics of Liquid Metal Ion Sources and Ion Optics and Their Application to Focused Ion Beam Technology* (Springer US; Imprint; Springer, Boston, MA, 2003).

94. L. A. Giannuzzi, F. A. Stevie, *Introduction to focused ion beams*, *Instrumentation, theory, techniques, and practice* (Springer, New York, 2005).

95. J. P. McCaffrey, M. W. Phaneuf, L. D. Madsen, Surface damage formation during ion-beam thinning of samples for transmission electron microscopy, *Ultramicroscopy.* **87**, 97–104 (2001).

96. A. Genç, D. Huber, D. Basile, H. L. Fraser, P. Fischione, Sample preparation for aberration corrected microscopy, *Microscopy and Microanalysis.* **14**, 998–999 (2008).

97. R.F. Egerton, Control of radiation damage in the TEM, *Ultramicroscopy*, 100–108 (2012).

98. R. Egerton, P. Li, M. Malac, Radiation damage in the TEM and SEM, *Micron.* **35**, 399–409 (2004).

99. R.F. Egerton, S. Lazar, M. Libera, Delocalized radiation damage in polymers, *Micron.* **43**, 2–7 (2012).

100. N. Jiang, Electron beam damage in oxides, *Rep. Prog. Phys.* **79**, 16501 (2016).

101. P. M. Kelly, A. Jostsons, R. G. Blake, J. G. Napier, The determination of foil thickness by scanning transmission electron microscopy, *phys. stat. sol. (a)*. **31**, 771–780 (1975).

102. S. M. Allen, Foil thickness measurements from convergent-beam diffraction patterns, *Philosophical Magazine A.* **43**, 325–335 (2006).

103. T. Malis, S. C. Cheng, R. F. Egerton, EELS log-ratio technique for specimen-thickness measurement in the TEM, *J Electron Microsc Tech*. **8**, 193–200 (1988).

104. K. Iakoubovskii, K. Mitsuishi, Y. Nakayama, K. Furuya, Thickness measurements with electron energy loss spectroscopy, *Microsc. Res. Tech.* **71**, 626–631 (2008).

105. D. R. G. MITCHELL, Determination of mean free path for energy loss and surface oxide film thickness using convergent beam electron diffraction and thickness mapping: a case study using Si and P91 steel, *J Microsc.* **224**, 187–196 (2006).

106. C.-W. Lee, Measurement of mean free paths for inelastic electron scattering of Si and SiO2, *Journal of Electron Microscopy.* **51**, 143–148 (2002).

107.   H. Meltzman *et al.,* An experimental method for calibration of the plasmon mean free path, *Journal of microscopy.* **236**, 165–173 (2009).

108.   P. L. Potapov, The experimental electron mean-free-path in Si under typical (S)TEM conditions, *Ultramicroscopy.* **147**, 21–24 (2014).

109.   Q. Jin, S. Wang, Investigation of Diffraction Condition and Convergent Probe Effects on Inelastic Mean Free Path Determination by Using a Cone-Shaped Silicon Crystal, *Microsc. Microanal.* **12**, 1184–1185 (2006).

110.   A. V. Aho, B. W. Kernighan, P. J. Weinberger, *The AWK programming language* (Addison-Wesley, Reading, Mass., 1988).

111.   F. Scholze, M. Procop, Modelling the response function of energy dispersive X-ray spectrometers with silicon detectors, *X-Ray Spectrom.* **38**, 312–321 (2009).

112.   P. Lechner *et al.,* Silicon drift detectors for high resolution room temperature X-ray spectroscopy, *Nuclear Instruments and Methods in Physics Research Section A: Accelerators, Spectrometers, Detectors and Associated Equipment.* **377**, 346–351 (1996).

113.   L. Strüder, P. Lechner, P. Leutenegger, Silicon drift detector - the key to new experiments, *Naturwissenschaften.* **85**, 539–543 (1998).

114.   H. v. Harrach *et al.,* An integrated Silicon Drift Detector System for FEI Schottky Field Emission Transmission Electron Microscopes, *Microsc Microanal.* **15**, 208–209 (2009).

115.   H. Soltau *et al.,* New Detector Architecture, for Electron Microscopes with SDDs, *Microsc Microanal.* **15**, 204–205 (2009).

116.   J. S. Iwanczyk *et al.,* Large Area Silicon Multi-Cathode Detector Developments for Microanalysis and High Speed Elemental Mapping, *Microsc Microanal.* **11**, 454–455 (2005).

117.   N. J. Zaluzec, Analytical formulae for calculation of X-ray detector solid angles in the scanning and scanning/transmission analytical electron microscope, *Microsc Microanal.* **20**, 1318–1326 (2014).

118.   J. T. Conway, Analytical solution for the solid angle subtended at any point by an ellipse via a point source radiation vector potential, *Nucl. Instr. Meth. Phys. Res.* **614**, 17–27 (2010).

119.   N. J. Zaluzec, On the geometry of the absorption correction for analytical electron microcopy, *Proceedings, Annual Conference - Microbeam Analysis Society* (1981).

120.   J. Kraxner *et al.,* Quantitative EDXS: Influence of geometry on a four detector system, *Ultramicroscopy.* **172**, 30–39 (2017).

121.   R. Pantel, Coherent Bremsstrahlung effect observed during STEM analysis of dopant distribution in silicon devices using large area silicon drift EDX detectors and high brightness electron source, *Ultramicroscopy*. **111**, 1607–1618 (2011).

122.   M. Watanabe, D. W. Ackland, D. B. Williams, The effect of large solid angles of collection on quantitative X-ray microanalysis in the AEM, *J Microsc*. **195**, 34–43 (1999).

123.   P. G. Kotula, L. N. Brewer, J. Michael, L. Giannuzzi, Computed Tomographic Spectral Imaging, *Microsc Microanal*. **13**, 1324–1325 (2007).

124.   K. Lepinay, F. Lorut, R. Pantel, T. Epicier, Chemical 3D tomography of 28nm high K metal gate transistor: STEM XEDS experimental method and results, *Micron*. **47**, 43–49 (2013).

125.   T. J. A. Slater, P. H. C. Camargo, M. G. Burke, N. J. Zaluzec, Haigh, Understanding the limitations of the Super-X energy dispersive x-ray spectrometer as a function of specimen tilt angle for tomographic data acquisition in the S/TEM, *J. Phys.: Conf. Ser.* **522**, 12025 (2014).

126.   T. J. A. Slater *et al.,* STEM-EDX tomography of bimetallic nanoparticles: A methodological investigation, *Ultramicroscopy*. **162**, 61–73 (2016).

127.   C. S. M. Yeoh *et al.,* The Dark Side of EDX Tomography: Modeling Detector Shadowing to Aid 3D Elemental Signal Analysis, *Microsc Microanal*. **21**, 759–764 (2015).

128.   W. Xu, J. H. Dycus, X. Sang, J. M. LeBeau, A numerical model for multiple detector energy dispersive X-ray spectroscopy in the transmission electron microscope, *Ultramicroscopy*. **164**, 51–61 (2016).

129.   N. J. Zaluzec, Calculating the Detector Solid Angle in X-ray Energy Dispersive Spectroscopy, *Microsc Microanal*. **15**, 520–521 (2009).

130.   N. J. Zaluzec, Detector solid angle formulas for use in X-ray energy dispersive spectrometry, *Microsc. Microanal.* **15**, 93–98 (2009).

131.   M. Schäfer, Diploma thesis, Technical University of Graz (17.07.2013).

132.   R. Egerton, S. C. Cheng, Characterization of an analytical electron microscope with a NiO test specimen, *Ultramicroscopy*. **55**, 43–54 (1994).

133.   W. van Aarle *et al.,* The ASTRA Toolbox: A platform for advanced algorithm development in electron tomography, *Ultramicroscopy*. **157**, 35–47 (2015).